Statistical analysis of classical and quantum measurements of free fall acceleration of antihydrogen for the GBAR experiment

Olivier Rousselle

▶ **To cite this version:**

Olivier Rousselle. Statistical analysis of classical and quantum measurements of free fall acceleration of antihydrogen for the GBAR experiment. Quantum Physics [quant-ph]. Sorbonne Université, 2022. English. NNT : 2022SORUS218 . tel-03725484v2

HAL Id: tel-03725484

https://theses.hal.science/tel-03725484v2

Submitted on 21 Nov 2022

HAL is a multi-disciplinary open access archive for the deposit and dissemination of scientific research documents, whether they are published or not. The documents may come from teaching and research institutions in France or abroad, or from public or private research centers.

L'archive ouverte pluridisciplinaire **HAL**, est destinée au dépôt et à la diffusion de documents scientifiques de niveau recherche, publiés ou non, émanant des établissements d'enseignement et de recherche français ou étrangers, des laboratoires publics ou privés.

École doctorale : "Physique en Ile-de-France"

THÈSE DE DOCTORAT SORBONNE UNIVERSITÉ

Réalisée au Laboratoire Kastler Brossel

Présentée par

Olivier ROUSSELLE

Pour obtenir le grade de docteur délivré par Sorbonne Université

Analyse statistique des mesures classiques et quantiques de l'accélération de chute libre de l'antihydrogène pour l'expérience GBAR

Statistical analysis of classical and quantum measurements of free fall acceleration of antihydrogen for the GBAR experiment

Soutenue le 13 juin 2022 devant le jury composé de :

Mme Marie-Christine Angonin	Examinatrice
M. Daniel Bloch	Rapporteur
M. Paolo Crivelli	Examinateur
Mme Martina Knoop	Examinatrice
M. Giovanni Manfredi	Rapporteur
M. Serge Reynaud	Directeur de thèse

Contents

Introduction

In 1924, De Broglie conjectured that every microscopic particle is associated with a wave of wavelength

$$\lambda_{dB} = \frac{h}{p} \ , \tag{1}$$

with p its momentum and h the Planck constant [1]. This hypothesis was confirmed in 1928 by Davisson and Germer [2] with the experiment of electron diffraction. The evolution of a matter wave function ψ in a potential V is governed by the Schrödinger equation discovered in 1926 [3]:

$$i\hbar\frac{\partial\psi}{\partial t} = \left(-\frac{\hbar^2}{2m}\Delta + V\right)\psi \tag{2}$$

with $\hbar = h/2\pi$ the reduced Planck constant, m the mass of the particle and Δ the Laplacian. The inherent quantum uncertainty on position and momentum was described in 1927 by the Heisenberg principle [4]:

$$\Delta x \ \Delta p \geqslant \frac{\hbar}{2} \tag{3}$$

with Δx the position dispersion, Δp the momentum dispersion.

Nowadays, the wave-like behavior of quantum matter still captivates physicists. A quantum wave function can penetrate classically forbidden regions, leading to the famous tunneling effect. Moreover, a quantum wave packet can reverse its direction of propagation in the absence of a classical turning point. This last phenomenon is commonly known as quantum reflection. In fact, quantum reflection is a general feature of wave propagation in inhomogeneous media [5, 6], like atmospheric and oceanic waves for example, and it occurs in regions where the wavelength varies rapidly. Quantum reflection has been studied for the attractive Casimir potential since the early days of quantum mechanics [7, 8], and it was first observed experimentally for ultracold atoms on solid surfaces [9, 10, 11, 12]. The scattering of the atomic matter wave on the Casimir-Polder potential of a surface is very different from that of a classical particle. The Casimir-Polder force is attractive, so that one would expect an incoming atom to be accelerated towards the surface and eventually hit it. On the contrary, the atom has a significant probability to be reflected away from the surface [13, 14].

Some experiments have observed the bounces of particles on different surfaces. These quantum bouncers are trapped by the combined action of reflection and gravity. The

quantum bound states have been described theoretically [15, 16, 17, 18], but since the gravitational force is very weak at atomic scales, extremely cold particles are needed to resolve them experimentally. These Gravitational Quantum States (GQS) have first been observed with ultracold neutrons [19, 20, 21, 22]. They have not been observed on atoms, but their existence is predicted also in this case as a consequence of quantum reflection from the attractive Casimir-Polder (CP) interaction on a mirror placed below the atoms [23, 24].

In this thesis, we will study the evolution of the atom during a free fall. One must keep in mind that the falling atom is not a classical point particle but a quantum matter wave. The fact that the falling wave function is extended and that it expands, means that the time at which the particle reaches the detector is randomly distributed. This is a consequence of the quantum uncertainty on the initial position and momentum of the particle. More generally, the absence of notions such as point particle or classical trajectory complicates the formulation of the weak equivalence principle in quantum mechanics [25, 26, 27, 28]. The gravitational interaction not only appears in the trajectories of motion but also in the phase of the wave function, when the neutron is in a spatial superposition of different gravitational potentials. The effect of gravity on quantum systems was first observed in the Colella-Overhauser-Werner (COW) experiment [29]. A phase shift was measured between the arms of a neutron interferometer when the device was tilted in the Earth's gravity field. Later on, atomic interferometers were able to measure the local gravitational acceleration with great precision [30].

GBAR: testing the equivalence principle for antimatter

The recognition that the motion of objects in a gravitational field is independent of their mass and composition was central to the birth of modern science in the 17^{th} century. In the last decades, the Equivalence Principle has been tested at high precision on macroscopic test masses and atoms [31, 32, 33, 34, 35, 36, 37, 38]. The space mission MICROSCOPE confirmed the weak equivalence principle with a relative precision of about 10^{-14} by comparing the free fall of macroscopic platinum and titanium masses [39].

Since Dirac's remarkable prediction in 1928 [40] and Anderson's observation of the positron in 1932 [41], antimatter has remained a topic of great interest for physicists. The antiparticle is defined as the symmetric of a particle after charge (C), parity (P) and time reversal (T) – the so called CPT symmetry -, and the CPT tests on antimatter are quite precise [42, 43, 44]. However, modern physics still fails to understand the apparent asymmetry between the numbers of particles and antiparticles in the visible universe. A natural way to progress in this domain is to explore the gravity for antimatter, that doesn't fit in the framework of Standard Model [45]. The possibility of an asymmetry in the gravitational behavior of matter and antimatter has been raised [46, 47, 48, 49, 50], with the possibility of negative gravitational mass for antimatter [51, 52, 53, 54, 55]. However, objections to this possibility are discussed in many papers [56, 57, 58].

In this context, it's important to test the effect of gravity on antimatter in experiments. A direct measurement of the acceleration of an antimatter particle in the Earth's

gravity field is a longtime objective of physicists. Experimental knowledge on this issue is much less precise than for gravitational properties of ordinary matter. Early experiments with charged antiparticles like antiprotons were thwarted by the preponderance of electromagnetic forces over gravity [59, 60, 61]. Current experimental endeavors are thus concentrating on neutral particles, especially the antihydrogen atom. The antihydrogen atom $\bar{H}$ is the bound state of an antiproton $\bar{p}$ and a positron e^+; it was first produced at high energies in CERN in 1995 [62]. Since then, much progress has been made towards lower temperatures and longer lifetimes [59, 63] in several experiments based at CERN's Antiproton Decelerator [64, 65, 66]. The aim of measuring the free fall acceleration $\bar{g}$ of anti-hydrogen $\bar{H}$ in Earth's gravitational field has been approached in the last decades [67] and indirect indications of the sign of $\bar{g}$ obtained very recently [68]. Improving the accuracy of the measurement of $\bar{g}$ will remain a crucial objective for advanced tests of the Equivalence Principle involving antimatter besides matter test masses [33, 36, 37, 38, 39].

The GBAR project (*Gravitational Behavior of Antihydrogen at Rest*) is one of the ongoing endeavors to determine the gravitational pull of the Earth on the simplest of antimatter atoms, antihydrogen. This ambitious experiment will produce, trap and cool antihydrogen atoms before dropping them in the Earth's gravity field, in a modern day reenactment of Galileo's tower experiment. The specificity of GBAR is that it will produce the antihydrogen ion $\bar{H}^+$, two positrons orbiting an antiproton, in order to take advantage of ion trapping and cooling techniques [69]. Once the ion is cold, a laser pulse is applied to detach the excess positron forming a neutral antiatom $\bar{H}$. The laser pulse marks the start of the free fall towards a detection plate. The aim is to measure $\bar{g}$ with an accuracy of the order of 1% by timing the classical free fall of antiatoms [70, 71].

An important goal of this thesis will be to study precisely the expected accuracy of the GBAR experiment, accounting for the recoil transferred in the photodetachment process. We will highlight what are the optimal parameters in the design of the free fall chamber to get the best precision.

The presence of the attractive Casimir-Polder potential on surfaces of the free fall chamber induces quantum reflection phenomenon: antihydrogen atoms have a probability to bounce above the detection surface, preventing their annihilation. The reflected atoms will not be detected at the expected time, leading to a loss in statistics. Moreover, higher energy atoms are less affected by quantum reflection and are thus more likely to be detected. Accurately modeling quantum reflection is therefore necessary to correct this mechanism which could otherwise bias the measurement.

Quantum interference measurement of the GBAR experiment

The interest of studying quantum reflection for antimatter has been highlighted by physicists, for example with antihydrogen atoms [13, 23, 72]. This phenomenon is in particular crucial for spectroscopic studies of the quantum levitation states of antihydrogen atoms trapped by quantum reflection and gravity [19]. We use this quantum phenomenon to study an original experimental setup, consisting of adding a reflecting surface to gen-

erate interferences between quantum states, before the free fall of the antihydrogen on the detector, thus producing interference pattern containing much more information on $\bar{g}$ that the classical distribution of free fall time. This study was already proposed in the thesis of P.P. Crépin [73], but without taking into account the photodetachment process of the excess positron. The main goal of this quantum design is to increase considerably the precision of the GBAR experiment.

Outline of the thesis

Chapter I deals with the free fall of quantum wave packet of antihydrogen as part of the GBAR experiment. We solve the Schrödinger equation for a particle in the Earth gravitational field. The Wigner function formalism is introduced to discuss the links between quantum and classical descriptions of motion. The photodetachment of the positron and associated momentum recoil is taken into account in our study, as well as quantum reflection on the detection surfaces. Based on these results, we can compute the annihilation current J at the detection. The uncertainty of this classical free fall experiment is evaluated by using the Monte-Carlo simulation and Cramer-Rao statistical analysis (optimal lower bound). Our simulations aim at finding the optimal parameters for the design of the free fall chamber to get the best accuracy possible in the classical free fall timing experiment.

In chapter II, we study a new measurement technique of the antihydrogen free fall acceleration producing interferences of quantum levitation states. We describe the experimental setup, that could be implemented in the GBAR experiment, and derive the evolution of the atomic wave packet from the photodetachment to the detection. We also present statistical methods to extract an estimation of $\bar{g}$ and give the standard deviation that is much smaller than the one achieved with the free fall timing experiment.

The numerical calculations are performed using the programming language `Python` and its high performance compiler `Numba`. Original statistical analysis methods will be highlighted: analysis from non-gaussian likelihoods, mean-likelihood estimator, statistics from interference pattern,...

A few technical discussions are presented in the Appendices. The appendix A details the equations governing the evolution of a gaussian wave paquet in a gravitational field. Appendix B details theoretical considerations concerning quantum reflection on Casimir-Polder potential. Appendix C presents the important algorithms, codes and numerical computations used in this thesis.

A bibliography, list of publications and an index of notations are given at the end of the manuscript.

Chapter I

Timing the free fall of antihydrogen wave packet in GBAR experiment

In this chapter, we determine the accuracy to be expected for the measurement of free fall acceleration of antihydrogen in the GBAR experiment, and we evaluate if we can reach a relative uncertainty below 1%. A goal is to determine whether the photodetachment recoil is a limiting factor to the precision. Our analysis will ease the constraints on the choice of the parameters of the trap and photodetachment laser, as well as the design parameters of the GBAR free fall chamber.

I.1 Presentation and goal of the GBAR experiment

One of the most important questions of fundamental physics is the asymmetry between matter and antimatter observed in the Universe [74, 75, 76, 77]. In this context, it is extremely important to compare the gravitational properties of antimatter with those of matter [46, 54, 56, 57, 58, 78]. Experimental knowledge on this question is much less precise than for gravitational properties of ordinary matter [58, 60, 79]. The aim of measuring the free fall acceleration $\bar{g}$ of anti-hydrogen $\bar{H}$ in Earth's gravitational field has been approached in the last decades [67] and indirect indications of the sign of $\bar{g}$ obtained very recently [68].

Ambitious projects are currently developed at new CERN facilities to produce low energy anti-hydrogen atoms [80] and to improve the accuracy of $\bar{g}$-measurement [71, 81, 82, 83]. Among these projects, the GBAR experiment (*Gravitational Behaviour of Anti-hydrogen at Rest*) aims at timing the free fall of ultra-cold $\bar{H}$ atoms, with a precision goal of 1% [70, 84].

The principle of GBAR experiment is based upon an original idea of Walz and Hänsch [69]. GBAR is an international collaboration with several institutions led by CEA (France). Parts of the work presented below have been done in collaboration with the teams in Kastler–Brossel Laboratory (France), ETH Zurich (Switzerland), Laue-Langevin Institute (France) and University of Mainz (Germany).

Using a neutral particle for GBAR experiment is necessary in order to avoid electromagnetic interference (at this microscopic scale, electromagnetism is dominant over gravity). In theory, the electrically neutral antineutrons would be the smallest chunks for this experiment, but they can't be used due to their quick decay time. The next simplest particle is therefore antihydrogen, the simplest antimatter atom.

I.1.1 Production of antihydrogen

Producing antihydrogen requires antiproton and positron, and the different steps needed for the final measurement are illustrated in figure I.1.

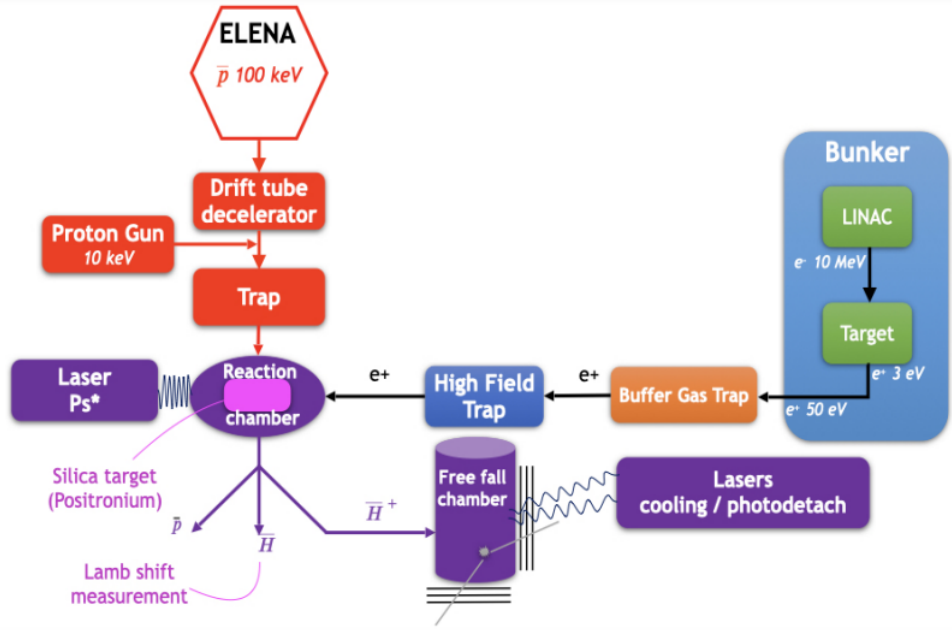

Figure I.1: Scheme of the different steps of the GBAR experiment.

Antiprotons are produced by collisions of $\sim$ 26 GeV protons at the LHC at CERN. *Extra Low ENergy Antiproton ring* (ELENA) is a 30 m hexagonal electrostatic ring that decelerates those antiproton beams from an energy of 5.3 MeV to 100 keV for precise measurements; it is situated inside the Antiproton Decelerator (AD) complex [80, 85, 86]. Antiprotons are then slowed down to approximately 1 keV using an electrostatic decelerator and a drift tube [87, 88]. Along with antiprotons from AD, the GBAR experiment also needs a intense flux of positrons, which are generated by the collision of 9 MeV electrons from a linear accelerator (LINAC) with a tungsten target [89]. Positrons from the intense LINAC-based source are first trapped in a buffer gas accumulator and collected in a high-field Penning trap [90]. The accumulated e^+ are then ejected onto a nanoporous silica film inside a cavity, forming a positronium (Ps, bound state e^+e^-) cloud in vacuum [91, 92, 93, 94]. Then the antiproton beam strikes the target made of this positronium cloud, producing $\bar{H}^+$ ions by two successive charge-exchange reactions

[95, 96]:

$$\bar{p} + Ps \rightarrow \bar{H} + e^- \tag{I.1}$$
$$\bar{H} + Ps \rightarrow \bar{H}^+ + e^-. \tag{I.2}$$

At the output of the reaction chamber, the $\bar{H}^+$ ions are separated from $\bar{H}$ and $\bar{p}$. Although more difficult to produce than the simpler antiatoms $\bar{H}$, the antimatter ions $\bar{H}^+$ can be more easily manipulated. They are trapped and sympathetically cooled to microkelvin temperatures in a Paul trap filled with laser-cooled Be^+/HD^+ ion cloud [97, 98, 99, 100].

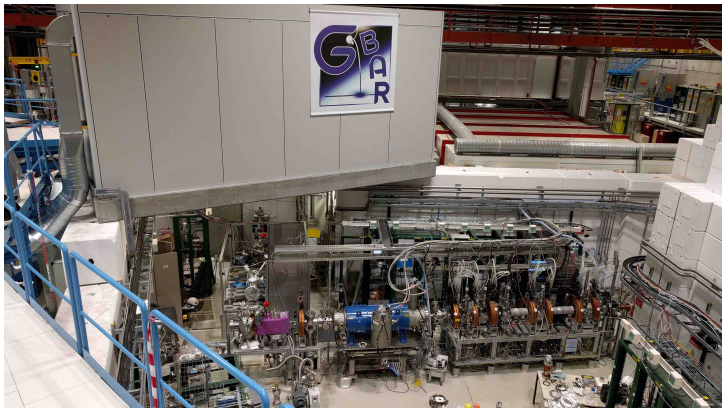

Figure I.2: Photo of the experimental hall at Antimatter Factory (2018) [101].

I.1.2 Free fall chamber

The excess positron of $\bar{H}^+$ is photodetached with a laser pulse, forming a neutral anti-hydrogen atom $\bar{H}$ [102, 103, 104]. This pulse marks the start of the free fall of the $\bar{H}$ neutral atom (as illustrated in figure I.3). The free fall on a given height is timed with a stop signal associated with the annihilation of anti-hydrogen reaching the surface of the detector [84].

The source of $\bar{H}$ atoms is placed at the centre of the cylindrical vacuum chamber (radius R_c and free fall height H_f) in which the free fall measurement is performed. The $\bar{H}$ atom will come in contact with the vacuum vessel and annihilate, producing on average three charged pions $\pi^{\pm}$ (see figure I.4). Micromegas detectors (Micro-Mesh Gaseous Structure) track the trajectory of the pions, allowing for the reconstruction of the $\bar{H}$ annihilation position. The Micromegas detectors of size 50 cm x 50 cm are arranged in groups of three, with 5 cm spacing between each other [105]. Additionally, Time of Flight (ToF) scintillator bars are forming the outer layer of the detection setup, and are used to measure the precise free fall time and help reject cosmic ray signals. Antihydrogen atoms easily traverse the vacuum chamber vessel and leave straight tracks

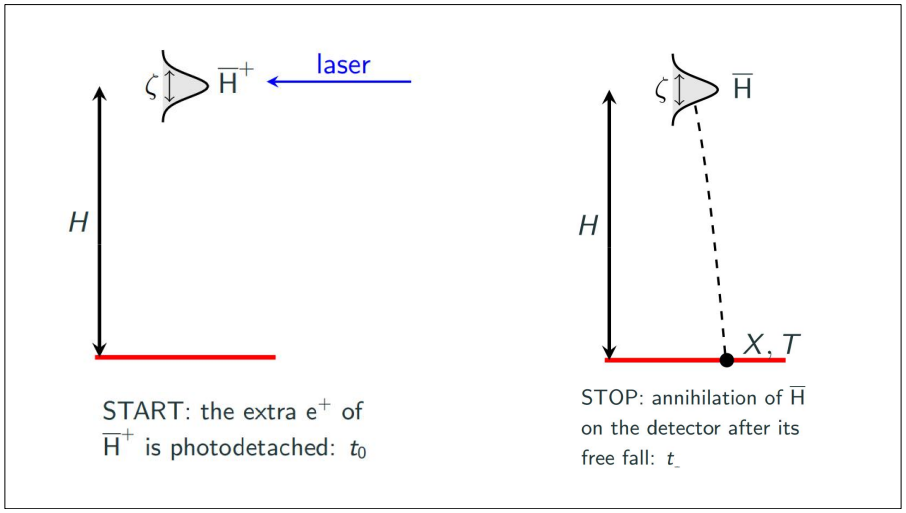

Figure I.3: Illustration of the photodetachment process in the free fall experiment.

by ionising the gas of the detectors. A cryogenic vacuum environment will lower the pressure such that residual gas annihilation is negligible.

The annihilation events are localized in space and time, and the free fall acceleration $\bar{g}$ is deduced from a statistical analysis of annihilation events. Our analysis is focused on the optimization of uncertainty, expected to reach a value of the order of 1% after analysis of the free fall of approximately $N = 1000$ atoms [70, 84].

In fact, we will see that the precision of the experiment is mainly limited by the initial velocity dispersion before the photodetachment process. For an accurate determination of $\bar{g}$, it is crucial to understand how the photodetachment process modifies the distribution of velocities and then affects the statistics of annihilation events. In the simulations, we assume that free fall acceleration of antihydrogen has its standard value $g_0 = 9.81\,\mathrm{m/s^2}$. We fix the initial number N of atoms but our analysis of dispersion accounts for the fact that the number of events N_c detected on the surfaces of the chamber may be smaller than N. At the end of calculations, we will obtain the mean μ_g and the standard deviation σ_g of the estimator defined for $\bar{g}$, simply denoted g from now on.

In this part, we will study the free fall of antihydrogen atoms for different configurations of the chamber. We start with the simple design with horizontal plane to test the effect of trap and photodetachment parameter. We then study the realistic full free fall chamber of the GBAR experiment with cylindrical shape. In this chamber, we will implement two disks positioned above and below the trap, which goal is to hide the complexity of the trap and to improve the accuracy of the experiment. We will finally make the analysis more complete by evaluating the effect of quantum reflection on the detection surfaces and on the disks.

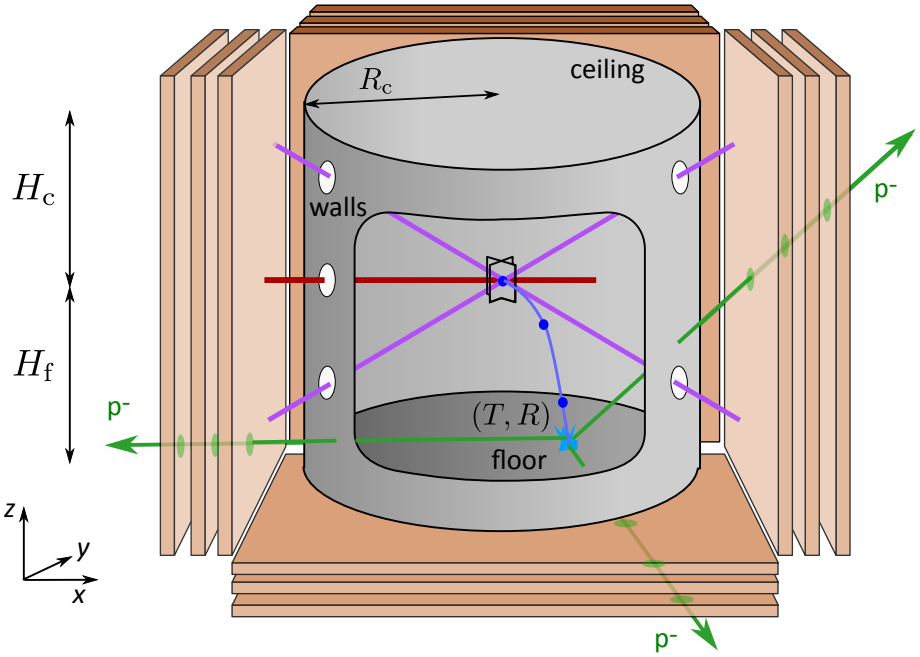

Figure I.4: Principle of the free fall measurement of antihydrogen in the GBAR experiment. $\bar{H}^+$ ions are laser cooled in an ion trap. The excess positron is photodetached by a horizontal laser (red line) to form a neutral $\bar{H}$ atom that falls under gravity. Micromegas and scintillation detectors are used to reconstruct the positions in space and time of the annihilation events on the surfaces of the chamber [106, 107, 108].

I.2 Simplest geometry: horizontal plane detection

The first design studied is the simple geometry where annihilation of antihydrogen takes place only on a horizontal plane placed at an altitude $H_f = 30$ cm below the trap. The main goal of this design is to study the effect of initial parameters like velocity dispersion Δv and energy recoil δE on the precision of the experiment.

In the following, we first discuss the initial distribution of velocities before the free fall and the distribution of annihilation events after the free fall. We then present a Monte-Carlo simulation of the measurement of the free fall acceleration g using first this simple geometry where atoms fall down to a horizontal detection plane.

I.2.1 Initial state before free fall

The initial velocity is composed of different components:

- The distribution in the Paul trap with width Δv ;
- The recoil induced by the absorption of the photon is constant, along the direction of propagation of the laser, with magnitude v_γ ;

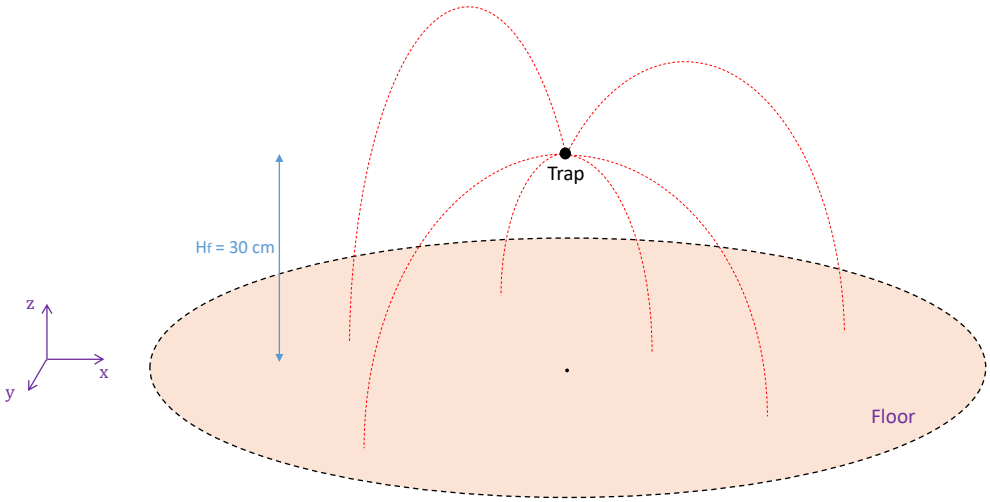

Figure I.5: Simple geometry of the GBAR experiment: free fall on a horizontal plane placed below the trap at a distance $H_f = 30$ cm. The trajectories from the trap to the horizontal plane are represented in red lines.

- The recoil velocity associated to the excess positron $\boldsymbol{v}_e$.

Then the initial velocity is:

$$\boldsymbol{v}_0 = \boldsymbol{v}_{\text{trap}} + \boldsymbol{v}_\gamma - \boldsymbol{v}_e. \tag{I.3}$$

Unless stated explicitly, the initial parameters of trap and laser used in the simulation are indicated in table I.1.

Parameter	**Value**
Trap frequency	$f = 1$ MHz
Initial velocity dispersion	$\Delta v = 0.44$ m/s
Photodetachment energy	$\delta E = 30$ μeV
Photodetachment velocity	$v_e = 1.76$ m/s

Table I.1: Values of the parameters of the trap and photodetachment process.

We detail below the different components of the initial velocity.

Distribution in the Paul trap Before the photodetachment process, the initial wave packet corresponds to the ground state of an harmonic and isotropic trap, with Heisenberg minimal dispersions identical along the 3 directions of space:

$$\zeta = \sqrt{\frac{\hbar}{2m\omega}}\ , \quad \omega = 2\pi f \tag{I.4}$$

with ζ position dispersion, f trap frequency, m mass of antihydrogen atom and $\hbar$ reduced Planck constant. From the Heisenberg relation, we get the velocity dispersion:

$$\Delta v = \frac{\hbar}{2m\Delta x} = \sqrt{\frac{\hbar\omega}{2m}} = \sqrt{\frac{hf}{2m}}. \tag{I.5}$$

Values of Δv and ζ are given in the table I.2 for different trap frequencies.

$\boldsymbol{\Delta v}$ **[m/s]**	$\boldsymbol{\zeta}$ **[nm]**	$\boldsymbol{f}$ **[MHz]**
0.77	41	3
0.44	71	1
0.24	130	0.3
0.14	220	0.1
0.077	410	0.03

Table I.2: Initial dispersions in velocity and position for different trap frequencies.

The ground state is represented by a wave-packet centered at the origin of space coordinates with a Gaussian shape in position:

$$\begin{aligned} \Psi_{\text{trap}}(\boldsymbol{r}_{\text{trap}}) &= \phi_{\text{trap}}(x_{\text{trap}}, y_{\text{trap}})\ \psi_{\text{trap}}(z_{\text{trap}}) \\ &= \left(\frac{1}{2\pi\zeta^2}\right)^{3/4} \exp\left(-\frac{\boldsymbol{r}_{\text{trap}}^2}{4\zeta^2}\right). \end{aligned} \tag{I.6}$$

with $\boldsymbol{r}_{\text{trap}} = (x_{\text{trap}}, y_{\text{trap}}, z_{\text{trap}})$ the position with respect to the trap center. This wave function is normalized:

$$\int_{\mathbb{R}^3} |\Psi_{\text{trap}}(\boldsymbol{r}_{\text{trap}})|^2 d^3\boldsymbol{r}_{\text{trap}} = 1. \tag{I.7}$$

The wave function has also a gaussian shape in the momentum representation:

$$\begin{aligned} \widetilde{\Psi}_{\text{trap}}(\boldsymbol{p}_{\text{trap}}) &= \frac{1}{(2\pi\hbar)^{3/2}} \int_{\mathbb{R}^3} \exp\left(-\frac{i}{\hbar}\boldsymbol{p}_{\text{trap}} \cdot \boldsymbol{r}_{\text{trap}}\right) \Psi_{\text{trap}}(\boldsymbol{r}_{\text{trap}}) d^3\boldsymbol{r}_{\text{trap}} \\ &= \left(\frac{1}{2\pi\Delta p^2}\right)^{3/4} \exp\left(-\frac{\boldsymbol{p}_{\text{trap}}^2}{4\Delta p^2}\right). \end{aligned} \tag{I.8}$$

The density matrix is defined in momentum representation as:

$$\rho_{\text{trap}}(\boldsymbol{r}_{\text{trap}}, \boldsymbol{r}'_{\text{trap}}) = \Psi_{\text{trap}}(\boldsymbol{r}_{\text{trap}}) \Psi^*_{\text{trap}}(\boldsymbol{r}'_{\text{trap}}). \tag{I.9}$$

We now introduce the Wigner formalism, i.e. the phase space formulation of quantum mechanics introduced by Wigner in 1932 [109]. The Wigner function W is a convenient representation of the density matrix [72], which fully describes quantum properties of the initial state. It is a quasi-probability distribution defined as a mixed position-momentum representation. Its proximity to the classical phase space distribution makes the Wigner

function an ideal tool to study the classical limit [110]. The Wigner distribution $W(\boldsymbol{r},\boldsymbol{p})$ of a state with density matrix ρ is defined as:

$$\begin{aligned} W(\boldsymbol{r},\boldsymbol{p}) &\equiv \frac{1}{(2\pi\hbar)^3}\int_{\mathbb{R}^3}\exp\left(-\frac{i}{\hbar}\boldsymbol{p}\cdot\boldsymbol{s}\right)\rho\left(\boldsymbol{r}+\frac{\boldsymbol{s}}{2},\boldsymbol{r}-\frac{\boldsymbol{s}}{2}\right)d^3\boldsymbol{s} \\ &= \frac{1}{(2\pi\hbar)^3}\int_{\mathbb{R}^3}\exp\left(-\frac{i}{\hbar}\boldsymbol{p}\cdot\boldsymbol{s}\right)\Psi\left(\boldsymbol{r}+\frac{\boldsymbol{s}}{2}\right)\Psi^*\left(\boldsymbol{r}-\frac{\boldsymbol{s}}{2}\right)d^3\boldsymbol{s}. \end{aligned} \tag{I.10}$$

For the gaussian state Ψ, the density matrix is a gaussian distribution of mean positions and differences and the Wigner function is a gaussian distribution of positions and momenta. In our case, the Wigner function in the trap becomes:

$$\begin{aligned} W_{\text{trap}}(\boldsymbol{r}_{\text{trap}},\boldsymbol{p}_{\text{trap}}) &= \frac{1}{(2\pi\hbar)^3}\int_{\mathbb{R}^3}e^{-\frac{i}{\hbar}\boldsymbol{p}_{\text{trap}}\cdot\boldsymbol{s}}\rho_{\text{trap}}\left(\boldsymbol{r}_{\text{trap}}+\frac{\boldsymbol{s}}{2},\boldsymbol{r}_{\text{trap}}-\frac{\boldsymbol{s}}{2}\right)d^3\boldsymbol{s} \\ &= \frac{1}{(2\pi\hbar)^3}\int_{\mathbb{R}^3}e^{-\frac{i}{\hbar}\boldsymbol{p}_{\text{trap}}\cdot\boldsymbol{s}}\left(\frac{1}{2\pi\zeta^2}\right)^{3/2}e^{-\frac{\boldsymbol{r}_{\text{trap}}^2+(\boldsymbol{s}/2)^2}{2\zeta^2}}d^3\boldsymbol{s} \\ &= \frac{1}{(\pi\hbar)^3}\exp\left(-\frac{\boldsymbol{r}_{\text{trap}}^2}{2\zeta^2}\right)\exp\left(-\frac{\boldsymbol{p}_{\text{trap}}^2}{2\Delta p^2}\right). \end{aligned} \tag{I.11}$$

where at the last step we used the gaussian integral

$$\int_{\mathbb{R}^3}\exp\left(-\alpha||\boldsymbol{x}||^2+\beta||\boldsymbol{x}||\right)d^3x = \left(\frac{\pi}{\alpha}\right)^{3/2}\exp\left(\frac{\beta^2}{4\alpha}\right). \tag{I.12}$$

We then calculate the probability in momentum space:

$$\begin{aligned} \Pi_{\text{trap}}(\boldsymbol{p}_{\text{trap}}) &= \int_{\mathbb{R}^3}W_{\text{trap}}(\boldsymbol{r}_{\text{trap}},\boldsymbol{p}_{\text{trap}})d^3\boldsymbol{r}_{\text{trap}} \\ &= \left(\frac{1}{2\pi\Delta p^2}\right)^{3/2}\exp\left(-\frac{\boldsymbol{p}_{\text{trap}}^2}{2\Delta p^2}\right). \end{aligned} \tag{I.13}$$

This momentum distribution can also be obtained directly from equation (I.8):

$$\Pi_{\text{trap}}(\boldsymbol{p}_{\text{trap}}) = \left|\widetilde{\Psi}_{\text{trap}}(\boldsymbol{p}_{\text{trap}})\right|^2 = \left(\frac{1}{2\pi\Delta p^2}\right)^{3/2}\exp\left(-\frac{\boldsymbol{p}_{\text{trap}}^2}{2\Delta p^2}\right). \tag{I.14}$$

The gaussian shape of the initial momentum distribution is represented in the figure I.6.

Recoil induced by the photon For antihydrogen, the threshold energy (electron affinity) is around 0.754 eV corresponding to a photon wavelength of 1.64 μm. The magnitude of the photon recoil is then

$$v_\gamma = \frac{\hbar k_\gamma}{m} \approx 0.24 \text{ m/s}. \tag{I.15}$$

with k_γ the wave vector of the photon and m the mass of antihydrogen. This value is fixed and doesn't show fluctuations. Moreover, the direction of the photon recoil is given by the laser propagation.

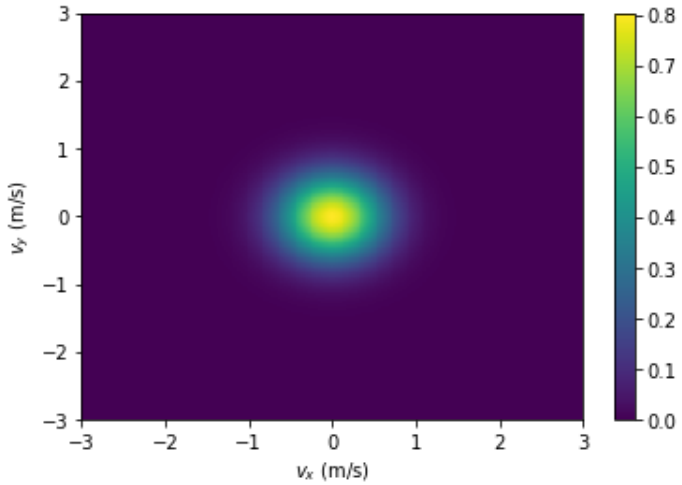

Figure I.6: Initial momentum distribution in the trap Π_{trap} in terms of velocities v_x and v_y. Parameters: $f = 1$ MHz / $\Delta v = 0.44$ m/s.

Photodetachment process The photodetachment of the excess positron relies on the absorption by the ion of a photon whose energy is high enough to detach the bound positron. The photodetachment efficiency depends on the energy δE above the threshold and scales as $\delta E^{3/2}$, which implies that large values of δE have to be favored to get a good photodetachment efficiency [102, 103, 104]. However this excess energy is transformed into kinetic energy which can be considered as a bad thing for the uncertainty in a naive linear variation analysis . The recoil of the atom is calculated by accounting for energy and momentum conservation.

The recoil $\boldsymbol{q}_e$ associated to excess positron has a fixed modulus q_e which in the limit $m_e \ll m$ is given by:

$$q_e = \sqrt{2m\delta E}. \tag{I.16}$$

The recoil velocity for the atom is fixed by excess energy δE above the photodetachment threshold, with typical values given in table I.3.

$\boldsymbol{v_e}$ **[m/s]**	$\boldsymbol{\delta E}$ **[μeV]**
1.25	15
1.77	30
2.17	45

Table I.3: Recoil velocity v_e for the atom for different excess energies δE

With these values of the excess energy, needed to reach a good photodetachment efficiency, v_e is larger than the velocity dispersion Δv before photodetachment, which would be a worrying problem in a naive precision analysis. $\boldsymbol{q}_e$ is expressed in spherical

coordinates as (see figure I.7):

$$\boldsymbol{q}_e = q_e \hat{q_e} = q_e \ (\sin\theta_e \cos\varphi_e, \sin\theta_e \sin\varphi_e, \cos\theta_e). \tag{I.17}$$

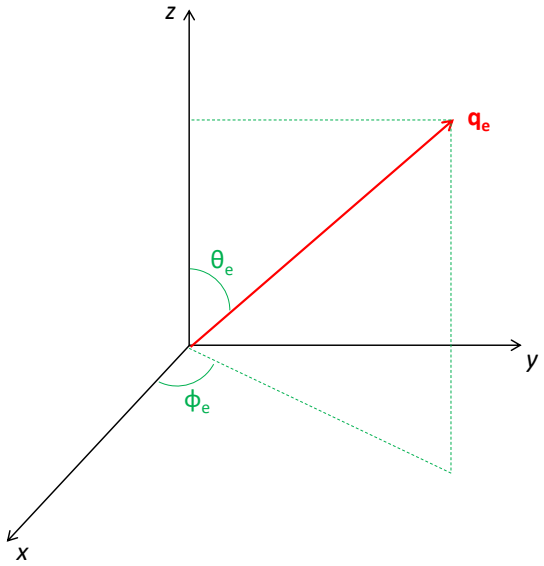

Figure I.7: Spherical coordinates of momentum transfer vector $\boldsymbol{q}_e$.

The recoil of the atom is calculated from energy and momentum conservation. We use here the approximation where it is described as an instantaneous elastic process, not affecting the position. The momentum transfer $\boldsymbol{q}$ is the sum of the photon momentum $\boldsymbol{q}_\gamma$ and the opposite $\boldsymbol{q}_e$ of the momentum of detached excess positron:

$$\boldsymbol{q} = \boldsymbol{q}_\gamma - \boldsymbol{q}_e = \hbar\boldsymbol{k}_\gamma - \boldsymbol{q}_e. \tag{I.18}$$

The recoil momentum associated to detached positron lies on a sphere with a center $\hbar\boldsymbol{k}_\gamma$ and a radius q_e.

After the photodetachment, the momentum of the atom is given by the sum of the momentum inside the trap and the recoil momentum transfered in the photodetachment:

$$\boldsymbol{p}_0 = \boldsymbol{p}_{\text{trap}} + \boldsymbol{q} = \boldsymbol{p}_{\text{trap}} + \hbar\boldsymbol{k}_\gamma - \boldsymbol{q}_e. \tag{I.19}$$

We first consider a pure state corresponding to the momentum transfer q. The wave function or equivalently the Wigner function are expressed as:

$$\begin{aligned} \Psi_q(\boldsymbol{r}_0) &= \exp\left(\frac{i}{\hbar}\boldsymbol{q}\cdot\boldsymbol{r}_0\right)\Psi_{\text{trap}}(\boldsymbol{r}_0) \\ &= \left(\frac{1}{2\pi\zeta^2}\right)^{3/4} \exp\left(-\frac{\boldsymbol{r}_0^2}{4\zeta^2} + \frac{i}{\hbar}\boldsymbol{q}.\boldsymbol{r}_0\right). \end{aligned} \tag{I.20}$$

$$\begin{aligned}\rho_q(\boldsymbol{r}_0,\boldsymbol{r}_0') &= \Psi_q(\boldsymbol{r}_0)\Psi_q^*(\boldsymbol{r}_0') \\ &= \exp\left(\frac{i}{\hbar}\boldsymbol{q}\cdot\boldsymbol{r}_0\right)\exp\left(-\frac{i}{\hbar}\boldsymbol{q}\cdot\boldsymbol{r}_0'\right)\Psi_{\text{trap}}(\boldsymbol{r})\Psi_{\text{trap}}^*(\boldsymbol{r}_0') \\ &= \exp\left(\frac{i}{\hbar}\boldsymbol{q}\cdot(\boldsymbol{r}_0-\boldsymbol{r}_0')\right)\rho_{\text{trap}}(\boldsymbol{r}_0,\boldsymbol{r}_0')\ . \end{aligned} \tag{I.21}$$

$$\begin{aligned}W_q(\boldsymbol{r}_0,\boldsymbol{p}_0) &= \frac{1}{(2\pi\hbar)^3}\int_{\mathbb{R}^3}\exp\left(-\frac{i}{\hbar}\boldsymbol{p}_0\cdot\boldsymbol{s}\right)\rho_q\left(\boldsymbol{r}_0+\frac{\boldsymbol{s}}{2},\boldsymbol{r}_0-\frac{\boldsymbol{s}}{2}\right)d^3\boldsymbol{s} \\ &= \frac{1}{(2\pi\hbar)^3}\int_{\mathbb{R}^3}\exp\left(-\frac{i}{\hbar}(\boldsymbol{p}_0-\boldsymbol{q})\cdot\boldsymbol{s}\right)\rho_{\text{trap}}\left(\boldsymbol{r}_0+\frac{\boldsymbol{s}}{2},\boldsymbol{r}_0-\frac{\boldsymbol{s}}{2}\right)d^3\boldsymbol{s} \\ &= W_{\text{trap}}(\boldsymbol{r}_0,\boldsymbol{p}_0-\boldsymbol{q}). \end{aligned} \tag{I.22}$$

The angular distribution on the sphere depends on the polarization of the laser. In spherical coordinate, with poles given by the direction of polarization of the photodetachment laser, the angular distribution probability is given by:

$$\varpi(\hat{q_e}) \equiv \frac{\mathrm{d}\mathcal{P}}{\mathrm{d}\Omega} = \frac{3}{4\pi}(\hat{q_e}\cdot\hat{n})^2 \tag{I.23}$$

with Ω the solid angle and $\hat{n}$ the laser polarization vector (unit vector orthogonal to the laser propagation direction):

$$\hat{n} = (0, \sin\theta_n, \cos\theta_n). \tag{I.24}$$

The normalization factor in (I.23) is such that

$$\int\varpi(\hat{q_e})d\Omega = \int_0^{\pi}\int_0^{2\pi}\frac{3}{4\pi}(\hat{q_e}\cdot\hat{n})^2\sin\theta_e d\theta_e d\varphi_e = 1. \tag{I.25}$$

For a vertical polarization, $\theta_n = 0$, $\hat{n} = (0,0,1)$, one obtains:

$$\varpi(\hat{q_e}) = \frac{3}{4\pi}\cos^2\theta_e. \tag{I.26}$$

For a horizontal polarization, $\theta_n = \pi/2$, $\hat{n} = (0,1,0)$, we get:

$$\varpi(\hat{q_e}) = \frac{3}{4\pi}\sin^2\theta_e\sin^2\varphi_e. \tag{I.27}$$

The Wigner function is then a statistical mixture over recoil directions:

$$W_0(\boldsymbol{r}_0,\boldsymbol{p}_0) = \int W_q(\boldsymbol{r}_0,\boldsymbol{p}_0)\varpi(\hat{q_e})d\Omega = \int W_{\text{trap}}(\boldsymbol{r}_0,\boldsymbol{p}_0-\boldsymbol{q})\varpi(\hat{q_e})d\Omega. \tag{I.28}$$

The momentum distribution, defined as the marginal of the modified Wigner function integrated over position, is:

$$\begin{aligned}\Pi_0(\boldsymbol{p}_0) &= \int_{\mathbb{R}^3}W_0(\boldsymbol{r}_0,\boldsymbol{p}_0)d^3\boldsymbol{r}_0 \\ &= \int W_{\text{trap}}(\boldsymbol{r}_0,\boldsymbol{p}_0-\boldsymbol{q})d^3\boldsymbol{r}_0\varpi(\hat{q_e})d\Omega \\ &= \int\Pi_{\text{trap}}(\boldsymbol{p}_0-\boldsymbol{q})\varpi(\hat{q_e})d\Omega. \end{aligned} \tag{I.29}$$

The momentum distribution is the convolution of the gaussian distribution of initial momentum and of the recoil distribution associated with positron.

The calculation of $\bar{\Pi}_0(\boldsymbol{p}_0)$ can be performed analytically. We first give the result for a vertical polarization:

$$\begin{aligned}\bar{\Pi}_0(\boldsymbol{p}_0) &\equiv \Pi_0(\boldsymbol{p}_0+\hbar\boldsymbol{k}_\gamma)=\int \Pi_{\rm trap}(\boldsymbol{p}_0+\boldsymbol{q}_e)\varpi(\hat{q}_e)d\Omega \\ &= \int_0^\pi\int_0^{2\pi}\left(\frac{1}{2\pi\Delta p^2}\right)^{3/2} e^{-\frac{(\boldsymbol{p}_0+\boldsymbol{q}_e)^2}{2\Delta p^2}}\varpi(\hat{q}_e)\sin\theta_e d\theta_e d\varphi_e \\ &= \left(\frac{1}{2\pi\Delta p^2}\right)^{3/2} e^{-\frac{\boldsymbol{p}_0^2+\boldsymbol{q}_e^2}{2\Delta p^2}}\int_0^\pi\int_0^{2\pi} e^{-\frac{\boldsymbol{p}_0\cdot\boldsymbol{q}_e}{\Delta p^2}}\frac{3}{4\pi}\cos^2\theta_e\sin\theta_e d\theta_e d\varphi_e.\end{aligned} \tag{I.30}$$

The expression of $\boldsymbol{q}_e$ and $\boldsymbol{p}_0$ in spherical coordinates are (by noting θ_v angle between the vertical axis $\hat{z}$ and velocity vector v):

$$\begin{aligned}\boldsymbol{q}_e &= q_e\ (\sin\theta_e\cos\varphi_e,\sin\theta_e\sin\varphi_e,\cos\theta_e)\ , \\ \boldsymbol{p}_0 &= p_0\ (\sin\theta_v\cos\varphi_v,\sin\theta_v\sin\varphi_v,\cos\theta_v).\end{aligned} \tag{I.31}$$

One then gets

$$\begin{aligned}\bar{\Pi}_0(\boldsymbol{p}_0) &= \left(\frac{1}{2\pi\Delta p^2}\right)^{3/2}\exp\left(-\frac{p_0^2+q_e^2}{2\Delta p^2}\right)\frac{3}{4\pi} \\ &\quad\times\int_0^\pi\int_0^{2\pi}\exp\left(-\frac{\sin\theta_v\sin\theta_e\cos\varphi_e+\cos\theta_v\cos\theta_e}{\sigma^2}\right)\cos^2\theta_e\sin\theta_e d\theta_e d\varphi_e\end{aligned} \tag{I.32}$$

with

$$\sigma^2=\frac{\Delta p^2}{p_0 q_e}. \tag{I.33}$$

By using isotropic integrals and modified Bessel function [111, 112], we deduce after some intermediate steps:

$$\bar{\Pi}_0(\boldsymbol{p}_0)=\frac{1}{\sqrt{2\pi}\Delta p}\left(e^{-\frac{(p_0-q_e)^2}{2\Delta p^2}}-e^{-\frac{(p_0+q_e)^2}{2\Delta p^2}}\right)\frac{3q_e}{4\pi P}((1-2I_*\cos^2\theta_v+I_*\sin^2\theta_v) \tag{I.34}$$

with

$$I_*=\frac{\sigma^2}{\tanh(1/\sigma^2)}-\sigma^4. \tag{I.35}$$

This distribution is normalized:

$$\int\bar{\Pi}_0(\boldsymbol{p}_0)d\boldsymbol{p}_0=1. \tag{I.36}$$

The distribution for a general polarization angle is finally obtained by a rotation of the system of coordinates, replacing in the expression the angle θ_v between directions $\hat{z}$ and $\boldsymbol{v}$ by the angle θ_{vn} between directions $\boldsymbol{v}$ and $\hat{n}$:

$$\bar{\Pi}_0(\boldsymbol{p}_0)=\frac{1}{\sqrt{2\pi}\Delta p}\left(e^{-\frac{(p_0-q_e)^2}{2\Delta p^2}}-e^{-\frac{(p_0+q_e)^2}{2\Delta p^2}}\right)\frac{3}{4\pi p_0 q_e}\left((1-2I_*\cos^2(\theta_{vn})+I_*\sin^2(\theta_{vn})\right). \tag{I.37}$$

The distributions $\bar{\Pi}_0$ drawn as functions of velocities $\boldsymbol{v}_0 = \boldsymbol{p}_0/m$ are shown in figure I.8 for different values of the parameters δE and f, for the case of a vertical polarization. The distributions, invariant under a rotation around the z-axis, are shown as a density plot in the v_y, v_z plane. Other polarizations are obtained by a 3D rotation of the distribution. Velocities after photodetachment lie on a spherical shell obtained as the convolution product of the sphere of photodetachment recoil velocities and the gaussian distribution of velocities in the ion trap. In the simulations, we will use a velocity dispersion of $\Delta v = 0.44$ m/s and photodetachment recoil velocity $v_e = 1.76$ m/s.

In most cases of experimental interest, the gaussian velocity Δv is smaller than the velocity recoil v_e, and the distribution is close to the initial one restricted on the sphere of radius v_e, with an angular density proportional to $\cos^2\theta_v$. The full distribution, for arbitrary values of Δv^2, describes a gaussian smearing along radial variations and a gaussian smearing of the initial angular distribution.

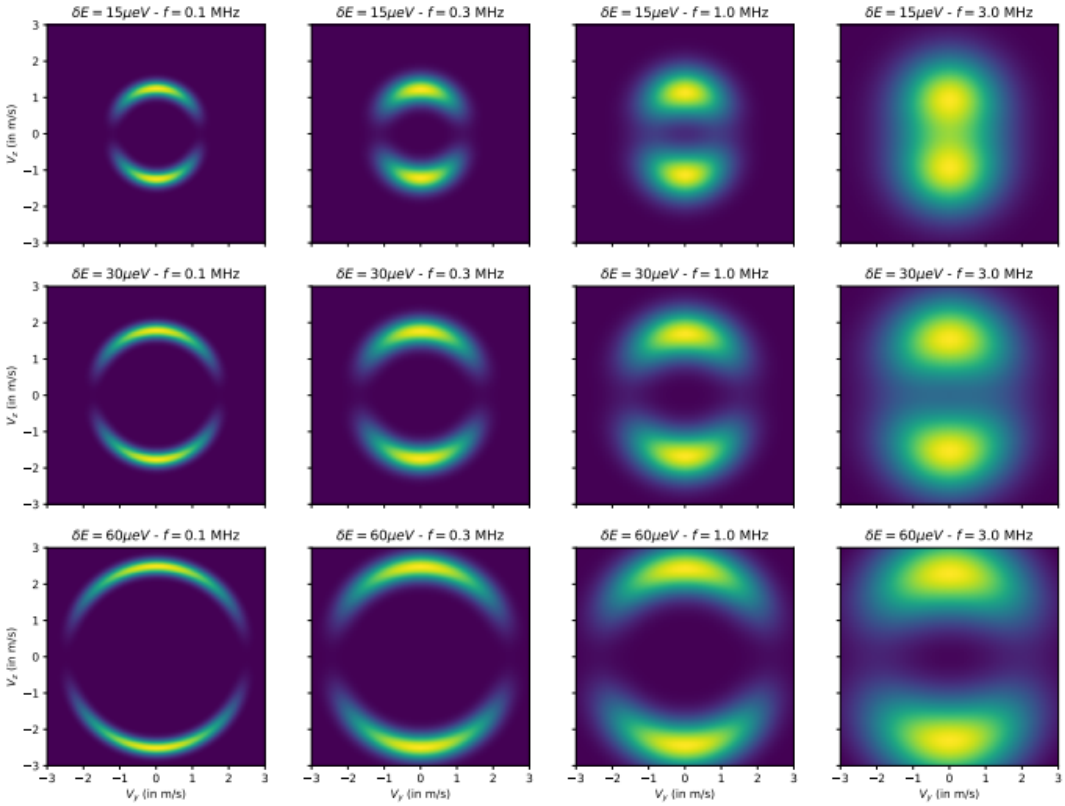

Figure I.8: Density plots of the velocity distributions in the v_y, v_z plane for $\delta E = 15$, 30, 60 μeV on the first, second and third lines respectively (corresponding to $v_e = 1.25$ m/s, 1.76 m/s and 2.50 m/s) and for $f = 0.1$, 0.3, 1, 3 MHz on the first, second, third and fourth columns respectively (corresponding to $\Delta v = 0.14$ m/s, 0.24 m/s, 0.44 m/s and 0.77 m/s) [108].

We assume that all atoms originate from the same point $(x_0, y_0, z_0) = (0, 0, 0)$, which corresponds to the position of the trap, at time $t_0 = 0$. After photodetachment, atoms freely fall in the gravity field and the free fall can be considered as classical if one uses the Wigner representation.

I.2.2 Free fall and annihilation probability current

After the free fall, each detection point is characterized by its position (x, y, z), time of flight t and speed (v_x, v_y, v_z). There is a one to one matching between the impact parameters ($\boldsymbol{r}$ and t) and the initial velocity v_0:

$$\begin{cases} x = v_{x_0} t \\ y = v_{y_0} t \\ z = v_{z_0} t - \frac{gt^2}{2} \end{cases} \quad \text{and} \quad \begin{cases} v_x = v_{x_0} = \frac{x}{t} \\ v_y = v_{y_0} = \frac{y}{t} \\ v_z = v_{z_0} - gt = \frac{z}{t} - \frac{gt}{2}. \end{cases}$$

with g the gravity field at Earth surface (reference value is $g_0 = 9.81$ m/s^2).

The Wigner function will be used to calculate the annihilation current; it has the remarkable property that for at most quadratic potentials, it connects classically those two positions in phase space [109]:

$$W_t(\boldsymbol{r}, \boldsymbol{p}) = W_0(\boldsymbol{r_0}, \boldsymbol{p_0}) \ , \tag{I.38}$$

with

$$\begin{aligned} &\boldsymbol{r}_0 = (x_0, y_0, z_0) \quad , \quad \boldsymbol{r} = (x, y, z) \ , \\ &\boldsymbol{p}_0 = m\left(\frac{\boldsymbol{r} - \boldsymbol{r}_0}{t} - \frac{\boldsymbol{g}t}{2}\right) \quad , \quad \boldsymbol{p} = m\left(\frac{\boldsymbol{r} - \boldsymbol{r}_0}{t} + \frac{\boldsymbol{g}t}{2}\right) \quad , \quad \boldsymbol{g} = (0, 0, -g). \end{aligned} \tag{I.39}$$

The observable is the particle current j, which is counted as a number of detected atom N per unit of time dt and per unit of surface dS:

$$\boldsymbol{j} = \frac{d^3N}{dS\ dt}\boldsymbol{n} = \frac{d^3N}{dV}\boldsymbol{v} = \rho \boldsymbol{v} \tag{I.40}$$

with dS unit of surface, dt unit of time, dV unit of volume, v speed and ρ density. By noting $|v_\perp|$ the speed orthogonal to the surface of detection, we get the current J normal to the detection surface:

$$\begin{aligned} J(\boldsymbol{r}, t) &= |v_\perp| \rho_t(\boldsymbol{r}, \boldsymbol{r}) \\ &= |v_\perp| \int_{\mathbb{R}^3} W_t(\boldsymbol{r}, \boldsymbol{p}) d^3\boldsymbol{p} \\ &= |v_\perp| \left(\frac{m}{t}\right)^3 \int_{\mathbb{R}^3} W_0(\boldsymbol{r}_0, \boldsymbol{p}_0) d^3\boldsymbol{r}_0 \quad , \quad \boldsymbol{p}_0 = m\left(\frac{\boldsymbol{r} - \boldsymbol{r}_0}{t} - \frac{\boldsymbol{g}t}{2}\right). \end{aligned} \tag{I.41}$$

We thus write J from the marginal of Wigner function that is also the initial momentum distribution Π_0:

$$J(\boldsymbol{r}, t) = \frac{m^3 |v_\perp|}{t^3} \Pi_0(\boldsymbol{p}_0). \tag{I.42}$$

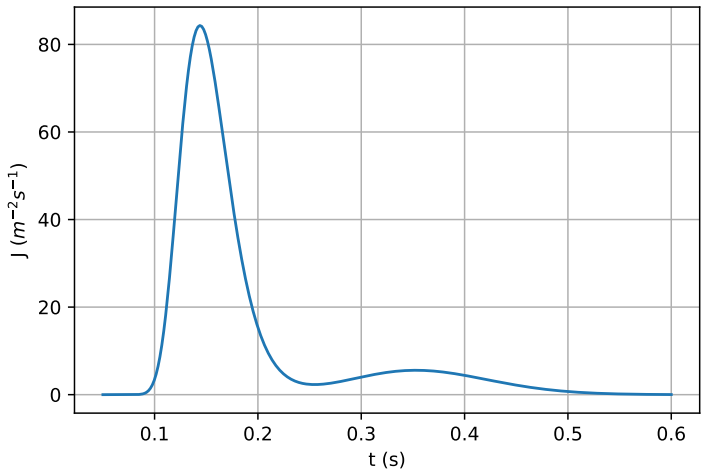

Figure I.9: Distribution of annihilation times, at the center of the floor ($r = 0$). Parameters: $f = 1$ MHz, $\delta E = 15$ μeV and vertical polarization of the laser.

For a detection on the horizontal plane, the orthogonal velocity is:

$$v_\perp = v_z = v_{z_0} - gt = \frac{z}{t} - \frac{gt}{2}. \tag{I.43}$$

Moreover, we check that the annihilation current over the detection surface is normalized so that

$$\int_{\mathbb{R}^3} J(\boldsymbol{r}, t) d^2\boldsymbol{r} dt = 1. \tag{I.44}$$

An example of such normalized distribution of annihilation events is shown in figure I.9 for a detection at the center of the floor. The distribution presents two peaks corresponding to atoms with different initial velocities which are annihilated at the same point but different time of flight. The heights and shapes of these two peaks depend on the precise values of the parameters entering the expression of $J(\boldsymbol{r}, t)$.

The distribution of annihilation current is also represented in figure I.10 by using false colour picture allowing to see both time and spatial coordinates. Due to the correlation between the vertical and horizontal velocity induced by the photodetachment, the maxima depends on the distance $R_\perp$ to the center (they do not form vertical lines) showing the importance to take into account the position in the analysis.

In the following parts, we will present analysis methods to determine the accuracy of the experiment. The first one is the linear variation analysis based on the relative uncertainty on the time arrival. Then we detail the analytical Cramer-Rao method based on the calculation of the Fisher information. Another way closer to the final data analysis to be designed for the experiment is the numerical Monte-Carlo method. We

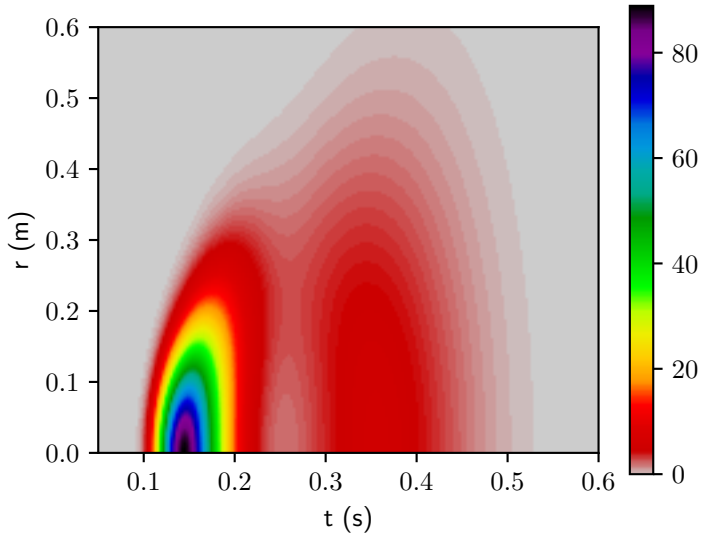

Figure I.10: Distribution of annihilation events ($J(\boldsymbol{r}, t)$ in $\mathrm{m}^{-2}\mathrm{s}^{-1}$) on the floor as a function of t and r (distance from the vertical axis) [108]. Same parameters as figure I.9.

compare the results of those methods, and use their good agreement as a cross validation of the results.

I.2.3 Linear variation analysis

We present here the statistical variation analysis to determine the accuracy of the experiment, as it was done in the initial proposal of GBAR [113]. In the simple design, the atom is prepared in a trap and then dropped on a detection plate, which results in a spread of the arrival time distribution (see figure 3 in appendix A). We note H the height between the trap and the detection plate. The quantum phase space quasi-distribution $W_t(z, p_z)$ obeys classical equations of motion in a uniform gravity field. It follows that we can do all calculations based on classical trajectories, by treating classical and quantum uncertainties on the same footing [14, 72]. The expression of g as function of our variables is

$$g = \frac{2v_{z_0}}{t - t_0} - \frac{2(z - z_0)}{(t - t_0)^2}. \tag{I.45}$$

The standard deviation on g can be expressed in terms of Δv_{z_0}, Δz_0, Δz, Δt_0 and Δt, the standard deviations of v_{z_0}, z_0, z, t_0 and t respectively considered as independent.

$$\begin{aligned} \Delta g &= \sqrt{\left|\frac{\partial g}{\partial v_{z_0}}\right|^2 \Delta v_{z_0}^2 + \left|\frac{\partial g}{\partial z_0}\right|^2 \Delta z_0^2 + \left|\frac{\partial g}{\partial z}\right|^2 \Delta z^2 + \left|\frac{\partial g}{\partial t_0}\right|^2 \Delta t_0^2 + \left|\frac{\partial g}{\partial t}\right|^2 \Delta t^2} \\ \longrightarrow \frac{\Delta g}{g} &= 2\sqrt{\left(\frac{\Delta v_{z_0}}{gt}\right)^2 + \left(\frac{\Delta z_0}{gt^2}\right)^2 + \left(\frac{\Delta z}{gt^2}\right)^2 + \left(\frac{\Delta t_0}{t}\right)^2 + \left(\frac{\Delta t}{t}\right)^2}. \end{aligned} \tag{I.46}$$

Can we simplify this expression ? The $\bar{H}^+$ ions in the Paul trap are very well localized to a few μm, and the annihilation position z of the $\bar{H}$ atom can be measured and stabilized to better than 100 μm [72, 113]. Moreover, the start time t_0 can be known with a precision better than 500 μs, and the annihilation time t can easily be measured to a better precision. Those arguments justify so we can neglect the dispersions Δz_0, Δz, Δt_0 and Δt respectively for a measurement of g at the % level. The relative uncertainty then becomes:

$$\frac{\Delta g}{g} \approx 2\frac{\Delta v_{z_0}}{gt} \approx 2\frac{\Delta v_{z_0}}{gt_H} \quad , \quad t_H = \sqrt{\frac{2H}{g}}. \tag{I.47}$$

This equation is correct only for 1 event. With N measurements, one gets an uncertainty on g of about:

$$\frac{\Delta g}{g} \approx \frac{1}{\sqrt{N}} 2\frac{\Delta v_{z_0}}{gt_H}. \tag{I.48}$$

In the GBAR proposal [113], it was estimated that about N=1500 fully detected annihilation events are needed to reach a 1% precision on g.

The term Δv_{z_0} has 2 sources: the initial velocity of the atom on the trap (with dispersion noted Δv previously) and the recoil of the photodetached positron. In this naive estimation of the sensitivity of the experiment, we see that the dispersion of the estimator of g is proportional to the dispersion of the vertical velocity distribution Δv_{z_0} just before the free fall, that is also just after the photodetachment process, and inversely proportional to the average free fall time t_H. An efficient way to decrease the relative uncertainty would consist then in decreasing the vertical velocity dispersion Δv_{z_0}. As a large part of the velocity dispersion is due to the excess energy delivered by the photodetachment process, this naive analysis could lead to restrict the excess energy and consequently limit the photodetachment efficiency. The photodetachment recoil is then a limiting factor.

In the following parts, we will use more robust statistical methods (Monte-Carlo / likelihood numerical method and Cramer-Rao analytical method). We will show that, contrary to the results of the linear analysis, the photodetachment recoil isn't a limiting factor and the precision is mainly limited by the initial velocity dispersion before the photodetachment process.

I.2.4 Monte-Carlo simulation

Considering a draw of N atoms that escape from the trap after the photodetachment process, we calculate the trajectory that depends on the random initial velocity $\boldsymbol{v}_0$ and deduce the annihilation position in space $\boldsymbol{r}_i$ and time t_i. We sum up here the different steps in this simulation.

Generation of events The Monte-Carlo simulation is performed by sampling random variables corresponding to the different sources of uncertainty in the initial velocity. The distribution in the trap is generated using a normal distribution function with a width

Δv given by (I.5). In `Python`, this normal distribution is generated by using the module `numpy.random.normal()`.

In spherical coordinates, the probability of the velocity direction (θ, φ) due to the photodetachment process is obtained using equation (I.23). This probability distribution is generated using two independent random variables X_1 and X_2 with uniform distributions in [0,1[producing random angles:

$$\theta_e = \arccos \sqrt[3]{1 - 2X_1} \quad , \quad \varphi_e = 2\pi X_2. \tag{I.49}$$

In `Python`, the variables X_1 and X_2 are generated using the module `numpy.random.rand()` (see appendix C for details of the code used). If the polarization forms an angle θ_n with the vertical, a rotation along the x-axis is performed to obtain the velocity components:

$$\boldsymbol{v}_e = v_e \begin{pmatrix} \sin\theta_e \cos\varphi_e \\ \cos\theta_n \sin\theta_e \sin\varphi_e + \sin\theta_n \cos\theta_e \\ -\sin\theta_n \sin\theta_e \sin\varphi_e + \cos\theta_n \cos\theta_e \end{pmatrix}. \tag{I.50}$$

Using the standard value $g_0 = 9.81$ m/s^2, we generate $N = 1000$ atoms with random initial velocity $\boldsymbol{v}_0$. Each atom undergoes a classical free fall, and each detection event is characterized by its impact position (x, y, z) on one of the surfaces of the chamber and its time of flight t.

We represent in figure I.11 a sample of 50 Monte-Carlo trajectories drawn in 2D plane (all azimuthal angles set to the same value, only for this representation). The point $(0, 0)$ is here the position of the trap. Trajectories have a shape of parabola with random initial velocity and reach the detection plate (horizontal line) situated 30 cm below the trap. The maximum radius reached is about 1 m.

Computation of likelihoods For each detection point generated from MC simulation, we evaluate the annihilation probability current $J(x, y, z, t)$. For a random draw of N detected events, we calculate the likelihood function [114, 115] as the product of current for the annihilation events:

$$\mathcal{L}(g) = \prod_{i=1}^{N} J_g(x_i, y_i, z_i, t_i). \tag{I.51}$$

Samples of 10 likelihood functions $\mathcal{L}$ are plotted in figure I.12 as function of $(g - g_0)/g_0$, each one calculated for a random draw of $N = 1000$ atoms. The number of 10 draws has been chosen to illustrate the variance while simultaneously avoiding confusion on the figure. The likelihood functions have gaussian shapes with similar values for their variance, but they are shifted with respect to one another, hence giving different values of the estimator. Each likelihood function leads to an estimation of the variance close to the variance deduced from the histogram of values on a large number of independent random draws. Their colors are chosen to make the figure more easily read.

The usual method is to estimate the value of g maximizing the likelihood:

$$\left(\frac{\partial \mathcal{L}(g)}{\partial g} \right)_{\hat{g}} = 0. \tag{I.52}$$

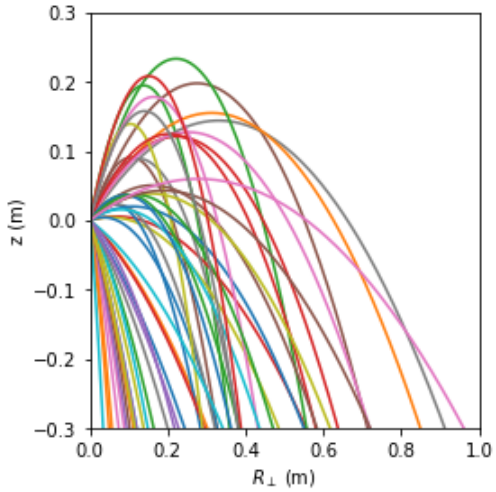

Figure I.11: Sample of 50 Monte-Carlo trajectories with vertical polarization of the laser and detection on horizontal plane. The point with coordinates (0,0) is the position of the trap.

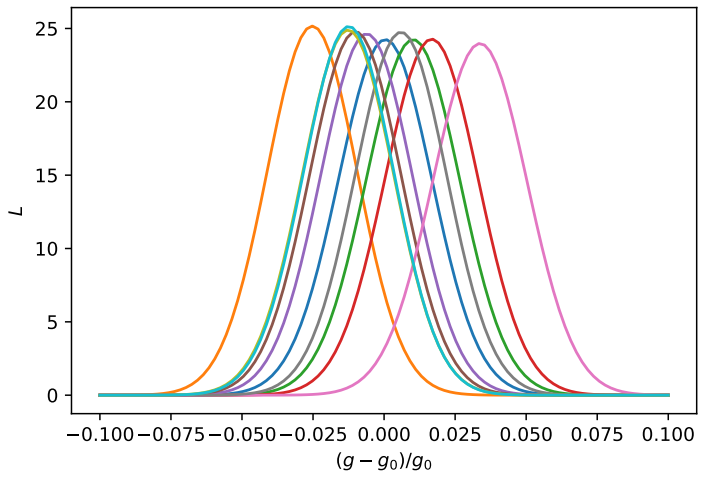

Figure I.12: Sample of 10 normalized likelihoods calculated for independent random draws of 1000 atoms for the simple design.

In `Python`, the estimation of g is obtained by minimizing the function $-\log \mathcal{L}(g)$, by using the module `scipy.optimize.fmin`. The value of this estimator will be denoted $\widehat{g}_{\max}$ in the following parts.

Calculation of the uncertainty We repeat this simulation process (generation of events and Max Likelihood estimation) a large number M of times. Each simulation provides an estimator $\widehat{g}_{\max}$, the distribution of which is plotted in figure I.13.

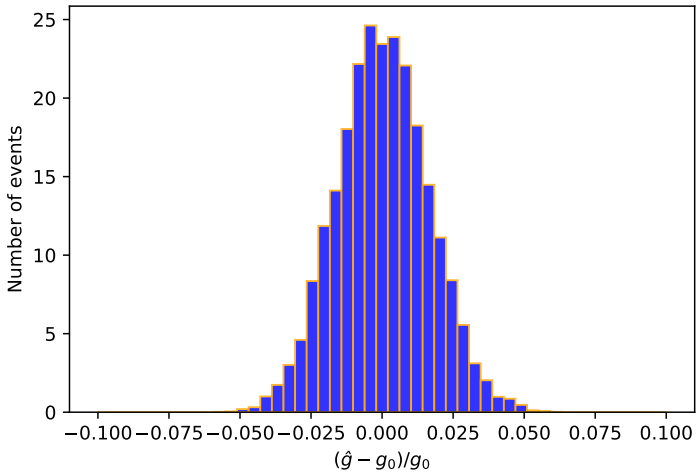

Figure I.13: Normalized histogram of the estimators $\widehat{g}$ for $M = 10000$ random draws for the simple design.

This distribution has nearly a gaussian shape and is symmetrical. From this histogram, we can extract the following information:

- The mean value of the distribution of $\widehat{g}_{\max}$ is denoted μ_g ;
- The standard deviation σ_g of the estimators $\widehat{g}_{\max}$ will often be given as the relative uncertainty σ_g/g_0 in the following.

The estimator isn't biased if $|\mu_g - g_0| < \sigma_g$ that is also when $|\text{bias}| < \sigma_g/g_0$. In our case, the mean value of the histogram is close to the value $g_0 = 9.81$ m/s^2, which means that the estimator has a negligible bias.

We also notice that there is an inherent statistical error in σ_g, because we generate an initial velocity with random norm and random direction. However, when we increase the number M of random draws, the statistical error decreases. We chose $M = 10000$ in order to reduce drastically this statistical error, and to get nearly the same value for σ_g if we repeat several times the Monte-Carlo simulation.

We may wonder if there exist another way to extract more information from the probability current density that leads to a lower uncertainty σ_g. In fact, the information contained on the probability distribution can be quantified by the Fisher information.

I.2.5 Cramer-Rao statistical method

The Cramer-Rao lower bound corresponds to an optimal estimation of the relative uncertainty. Whatever the estimation method we use, we can never reach a better uncertainty for the considered parameter.

Cramer-Rao lower bound This lower bound is deduced from the Fisher information $\mathcal{I}_g$ describing the g-dependence of the event distribution [114, 115, 116]:

$$\begin{aligned} \mathcal{I}_g &= \mathbb{E}\left[-\frac{\partial^2}{\partial g^2}\log J(g)\right] = \mathbb{E}\left[\left(\frac{\partial}{\partial g}\log J(g)\right)^2\right] \\ &= \int dSdT\frac{(\partial_g J_g)^2}{J_g}. \end{aligned} \tag{I.53}$$

Here $\mathbb{E}$ denotes the expectation value and J_g the probability current calculated for the value g. The last integral is calculated on the surface of the chamber and on the annihilation time.

We consider $\hat{g}$ an unbiaised estimator:

$$\mathbb{E}[\hat{g} - g] = 0. \tag{I.54}$$

After several steps and by using the Cauchy-Schwarz inegality, we have for 1 event [115]:

$$\mathbb{V}[\hat{g}]\ \mathcal{I} \geqslant 1. \tag{I.55}$$

For N events, the previous relation becomes:

$$\begin{aligned} \mathcal{I}_N(g) = N\ \mathcal{I} \quad &, \quad \mathbb{V}[\hat{g}]\ \mathcal{I}_N \geqslant 1 \\ \longrightarrow \quad &\mathbb{V}[\hat{g}] \geqslant \tfrac{1}{N\ \mathcal{I}}. \end{aligned} \tag{I.56}$$

Then the Cramer-Rao bound σ_g^{CR} is given by the number of events N and the Fisher information $\mathcal{I}$ [115]:

$$\sigma_g^{CR} = \frac{1}{\sqrt{N\ \mathcal{I}_g}}\ . \tag{I.57}$$

In our case of study, the calculation of the Fisher information is precisely:

$$\begin{aligned} \mathcal{I} &= \int_0^{+\infty}\int_{-\pi}^{\pi}\int_0^{+\infty} dr d\phi dt\ \mathbb{I}(r\cos\phi, r\sin\phi, t)\ , \\ \mathbb{I}(x,y,t) &= \frac{(\partial_g J_g(x,y,t))^2}{J_g(x,y,t)}. \end{aligned} \tag{I.58}$$

This triple integral is performed numerically, by using the module `scipy.integrate.nquad`:

```
I = nquad(integrand, [[0,np.inf],[-np.pi,np.pi],[0,np.inf]])[0]
```

An advantage of this method is its computation speed. Indeed, we evaluated that the simulation with the CR method is about 20 times faster than the MC - likelihood simulation with $M = 10000$.

Statistical efficiency

The Monte-Carlo dispersions σ_g^{MC} are expected to be slightly larger than the Cramer-Rao dispersions σ_g^{CR}, the difference being small for a good statistical efficiency, with the statistical efficiency e defined as [115]:

$$e = \left(\frac{\sigma_g^{CR}}{\sigma_g}\right)^2 \quad , \quad 0 \leqslant e \leqslant 1. \tag{I.59}$$

An estimator is called efficient if $e \approx 1$, meaning that the Cramer-Rao lower bound is nearly reached. From an experimental point of view, a good efficiency means that the unique random draw to be obtained in one experiment is representative of the variety of results for different random draws in the numerical simulations.

The relative uncertainty obtained with both methods for $f = 1$ MHz and $\delta E = 30$ μeV is around 1%:

$$\sigma_g^{MC}/g \approx 1.04\% \ , \tag{I.60}$$
$$\sigma_g^{CR}/g \approx 1.03\% \ , \tag{I.61}$$
$$e = \left(\frac{\sigma_g^{CR}}{\sigma_g^{MC}}\right)^2 \approx 0.98. \tag{I.62}$$

The statistical efficiency is then nearly satisfied for our design of horizontal plane considered in this part ($\sigma_g^{MC} \approx \sigma_g^{CR}$). This is directly related to the fact that the likelihoods are gaussian (see figure I.12).

We now study the effect of trap and laser parameters on the accuracy of the experiment.

I.2.6 Variation versus design parameters

We discuss here variations of the results versus trap and laser parameters, still with horizontal plane design, using Monte-Carlo or Cramer-Rao dispersions equivalently as they lead to the same conclusions, in all cases discussed below in this part.

Polarization of the laser We can study the effect of the polarization of the laser, by plotting the relative uncertainty σ_g/g as function of the polarization angle θ_n for $f = 1$ MHz and $\delta E = 30$ μeV. In particular, the relative uncertainty obtained for vertical and horizontal polarization of the laser is:

$$\sigma_g/g \ (\theta_n = 0^o) \approx 1.04\% \ , \tag{I.63}$$
$$\sigma_g/g \ (\theta_n = 90^o) \approx 1.62\% \ . \tag{I.64}$$

Those results stand in contrast with the expectation of the naive linear variation analysis sketched at the beginning of this part. The variance of vertical recoil is indeed smaller for a horizontal polarization than for a vertical one, so that naive expectations would

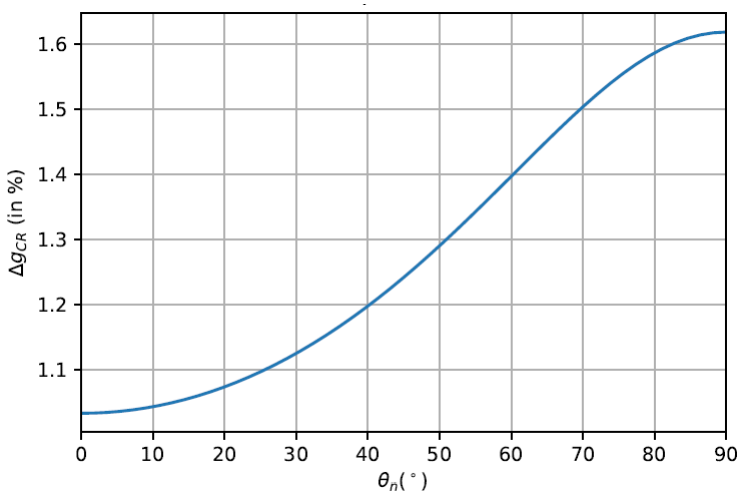

Figure I.14: Variations of relative dispersion as a function of θ_n (polarization angle).

lead to a larger dispersion in the former case than in the latter one. With the results of the full analysis performed in this part, the accuracy is better for vertical polarization. This can be traced to the fact that atoms with an initial upwards velocity have a longer time of flight, which is beneficial for the determination of g.

Variation of velocity dispersion Figure I.15 shows that the accuracy is improved (the relative dispersion is decreased) for lower values of $f/\Delta v$, the two curves corresponding to different polarization angles but the same excess energy. The accuracy is then highly determined by the Gaussian velocity distribution in the ion trap. We see also that the vertical polarization provides better accuracy than horizontal polarization, whatever the value of the velocity dispersion.

Variation of photodetachment recoil The effect of the photodetachment recoil is shown in figure I.16 with full lines representing Cramer-Rao predictions and dots showing the results of Monte-Carlo simulations. One clearly sees on the plot that the results of the two methods are close, which confirms the good statistical efficiency. One also notices a conclusion standing in contrast with the prediction of a dispersion proportional to the initial velocity dispersion, since the accuracy is improved for larger values of the excess energy.

The too naive linear variation analysis sketched previously leads to the prediction of a dispersion proportional to the dispersion of initial vertical velocity. It gives in most cases an accuracy poorer than the correct results produced by the analysis in this part. It also favours the choice of a horizontal polarization whereas the correct results lead to prefer a vertical polarization. The results obtained here thus reduce the constraints on the choice of photodetachment parameters, as they allow an increase of δE which is

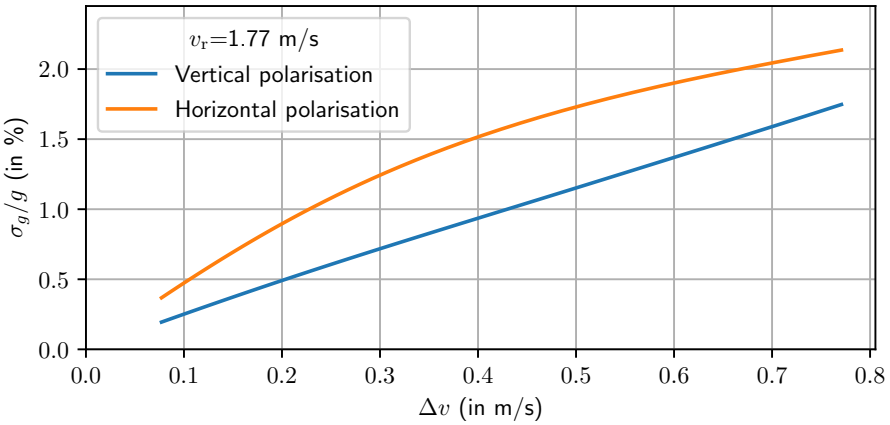

Figure I.15: Variations of relative dispersion, as a function of Δv, vertical and horizontal polarization of the laser, with recoil velocity v_e = 1.77 m/s [108].

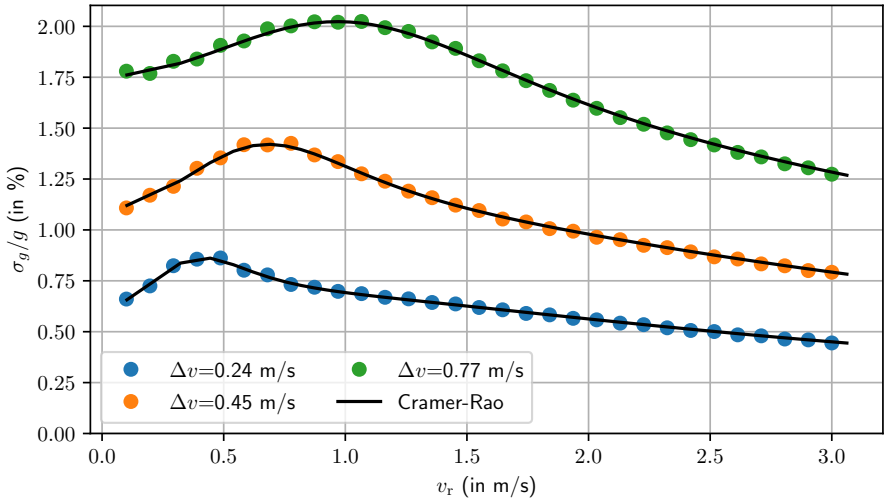

Figure I.16: Variations of predicted relative dispersions, as a function of recoil velocity v_e, for different velocity dispersions Δv and a vertical polarization. Full lines represent Cramer-Rao predictions while dots show the results of Monte-Carlo simulations [108].

certainly good for discussion of the photodetachment efficiency.

Up to now, we have considered only free fall on the horizontal floor. However, the experiment will take place in a chamber with finite dimensions for radius and height, and it is necessary to take into account the presence of the walls on which atoms having large initial velocities will annihilate.

I.3 Cylindrical free fall chamber

For a first realistic treatment of the GBAR free fall chamber, we consider a cylindrical chamber having finite dimensions for the free fall height $H_f = 30$ cm, with ceiling at height $H_c = 30$ cm above the trap and with radius $R_c = 25$ cm. It was the design of the free fall chamber considered by the collaboration when the thesis work began [70].

Atoms fall from the trap at the center of the chamber until they reach a material boundary on the floor, walls or ceiling of the chamber (see figure I.17). The free fall height $H_f = 30$ cm corresponds to a free fall time $t \approx 247$ ms for atoms with null initial vertical velocity. With $R_c = 25$ cm, antihydrogen atoms with an initial horizontal velocity larger than ~ 1 m/s hit the vertical walls before they can reach the floor. When this is the case, free fall times are shortened with respect to the situation where atoms are only detected on the floor, which should degrade the sensitivity to the measurement of g. This effect is relevant for a significant fraction of antiatoms, which should lead to poorer accuracy. The analysis of this degradation is discussed below.

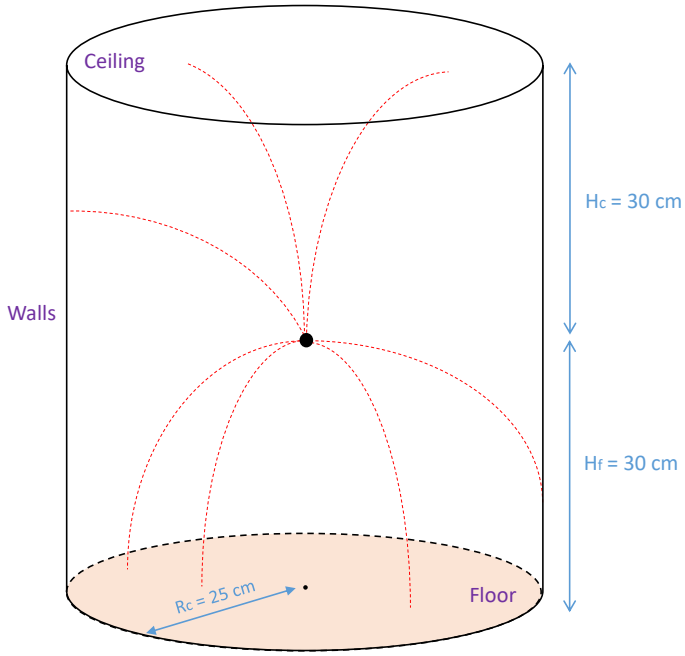

Figure I.17: Free fall inside cylindrical chamber of radius $R_c = 25$ cm and height 60 cm. The trajectories to the surfaces of the chamber are represented in red dotted lines.

We will apply the same procedures as before to compute the annihilation current, perform Monte-Carlo simulations and deduce maximum likelihood estimators $\widehat{g}$.

I.3.1 Current with discontinuities

The analytical formulas for the current are the same as in the last part with a horizontal plane. The only difference is that the orthogonal velocity at detection has different definitions for detections on different surfaces of the chamber:

$$v_\perp = v_{z_0} - gt = \frac{z}{t} - \frac{gt}{2}\ , \quad \text{detection on the floor or ceiling ;} \tag{I.65}$$

$$v_\perp = \sqrt{{v_x}^2 + {v_y}^2} = \frac{\sqrt{x^2+y^2}}{t}\ , \quad \text{detection on the walls.} \tag{I.66}$$

Antihydrogen atoms can touch the ceiling, when they have large enough upwards velocity in the initial distribution

$$v_{z_0} > v_s = \sqrt{2gH_c}. \tag{I.67}$$

The value of v_s (≈ 2.43 m/s with the standard value of $g_0 = 9.81$ m/s^2 and $H_c = 30$ cm) is independent of other parameters. It leads to a step in the annihilation current as a function of time of flight (see figure I.18), which has important consequences in the following analysis.

For a given position, we can calculate analytically the critical time t_c corresponding to this step. A "limit" trajectory can be described as the succession of two parabolic legs: an upward one from the trap to the ceiling and a downward one from the ceiling to the annihilation position.

$$\begin{aligned} t_c &= t_1\ (\text{trap} \rightarrow \text{ceiling}) + t_2\ (\text{ceiling} \rightarrow \text{annihilation}) \\ &= \frac{v_{z_0}}{g} + \frac{\sqrt{v_{z_0}^2 - 2gz}}{g} = \frac{\sqrt{2gH_c}}{g} + \frac{\sqrt{2gH_c - 2gz}}{g} \\ &= \sqrt{\frac{2H_c}{g}} + \sqrt{\frac{2(H_c - z)}{g}}. \end{aligned} \tag{I.68}$$

For example, for $H_c = 30$ cm and $z = -H_f$ (floor), we obtain $t_c \approx 597$ ms, which corresponds to the position of the cut emphasized by the zoom in figure I.18.

I.3.2 Analysis and relative uncertainty

The parameters used are the same as the ones used for the design with horizontal plane, they are indicated in table I.1.

Results of typical Monte-Carlo simulations are depicted in figure I.19. We have plotted a scatter of $N = 5000$ annihilation events for the different surfaces of the chamber. The color of the detection points indicates the time of flight, which is always smaller than $1s$. Very few atoms hit the ceiling.

The likelihood functions calculated for random draws of $N = 1000$ atoms are no longer perfectly Gaussian (figure I.20) while the histogram of estimated $\hat{g}$ for a number of different simulations has an asymmetric shape with a significant bias (figure I.21). This behaviour appears when we include the ceiling in the geometry, which induces a cut in the current J. This point will be discussed more thoroughly below.

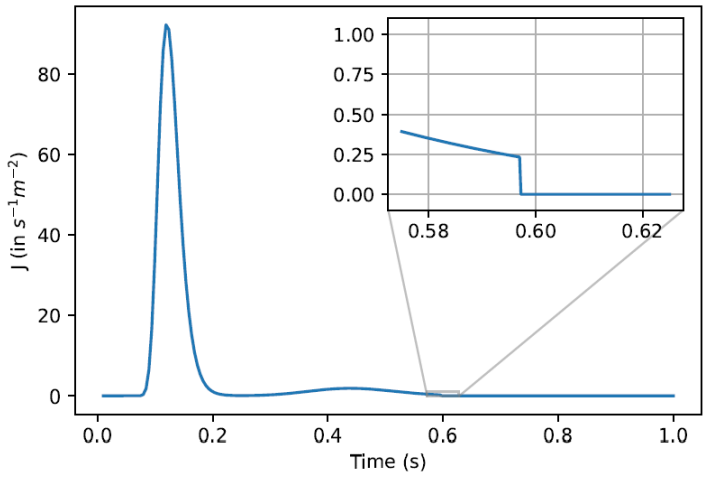

Figure I.18: Distribution of annihilation times on the floor, at $z = -H_f$. Parameters: $f = 1$ MHz, $\delta E = 30$ μeV and vertical polarization of the laser.

The relative uncertainties obtained with the Monte-Carlo method for the vertical and horizontal polarizations of the laser are:

$$\sigma_g^{MC}/g \ (\theta_n = 0^o) \approx 1.26\% \ , \tag{I.69}$$

$$\sigma_g^{MC}/g \ (\theta_n = 90^o) \approx 2.93\%. \tag{I.70}$$

As expected, the accuracy is a bit degraded compared to the situation with horizontal plane. Indeed, a significant fraction of atoms reach the wall before the floor, and their time of flight is reduced as well as the effective free fall height, leading to a detrimental effect on the accuracy.

The Fisher information is calculated by decomposing it on each detection surface of the free fall chamber:

$$\mathcal{I} = \mathcal{I}_{\text{floor}} + \mathcal{I}_{\text{walls}} + \mathcal{I}_{\text{ceiling}}. \tag{I.71}$$

However, the current J of annihilation times on the floor and on the walls contains a cut, as illustrated in figure I.18. The evaluation of the Fisher information in those surfaces leads to an error, as it involves the calculation of the derivative of J which isn't defined at the cut. This problem will be solved later in this chapter, by smoothing this step.

In the next part, we will add small disks inside the cylindrical chamber, positioned symmetrically above and below the trap.

I.4 Cylindrical chamber with disks

When we analyzed the role of annihilation on the surfaces of the free fall chamber, we discovered a new effect associated with the presence of "obstacles" and noticed at some point that "obstacles" could be used to improve the accuracy of the experiment. Indeed,

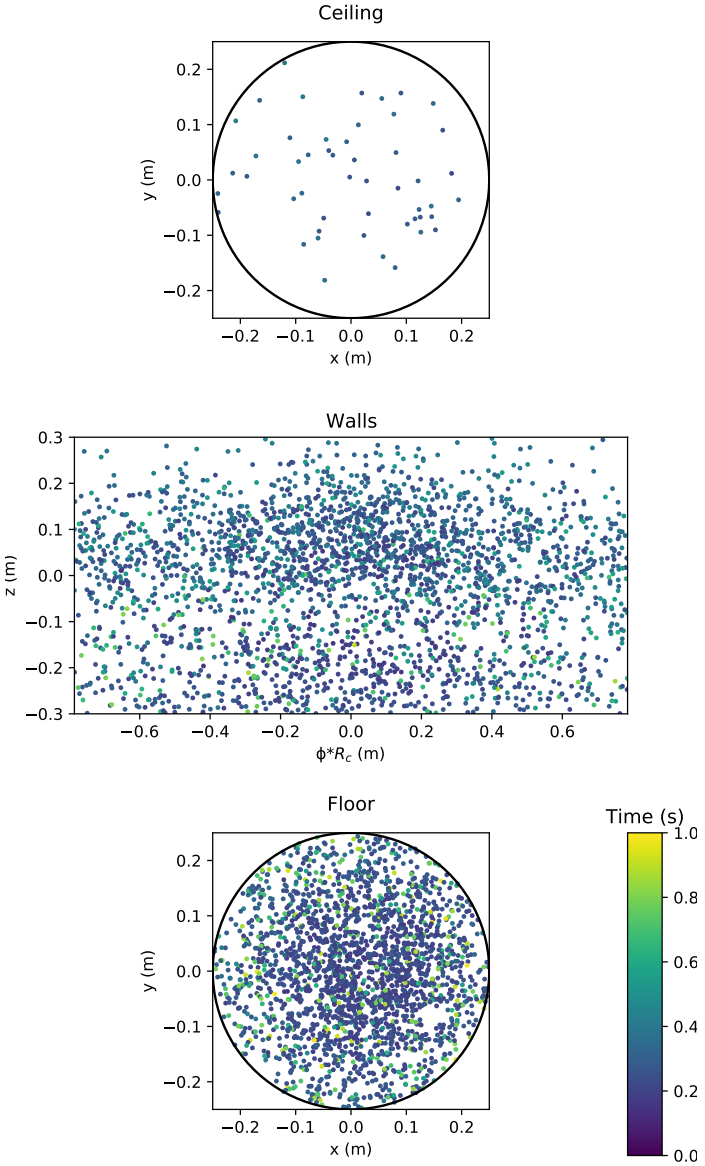

Figure I.19: Monte-Carlo generation of $N = 5000$ events, where the color indicates the time of flight t. Distribution of events: 45% on the floor, 54% on the walls, 1% on the ceiling. Vertical polarization of the laser.

near-edge events correspond to large information about the value of the free fall acceleration. This led us to design a new experimental configuration with two disks symmetrical placed in the vicinity of the source of antiatoms in order to maximize the advantage gained from near-edge events. The purpose of this part is to study this configuration.

The new design is represented in figure I.22-**a**, where we add two disks of radius

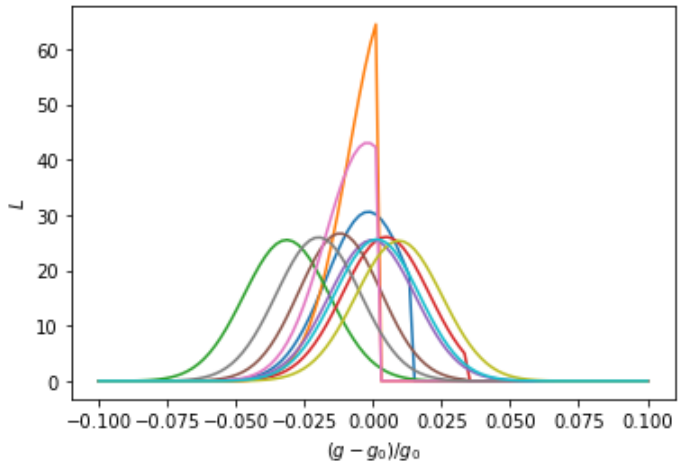

Figure I.20: Sample of 10 normalized likelihoods calculated in the case of the cylindrical chamber for independent random draws of 1000 atoms.

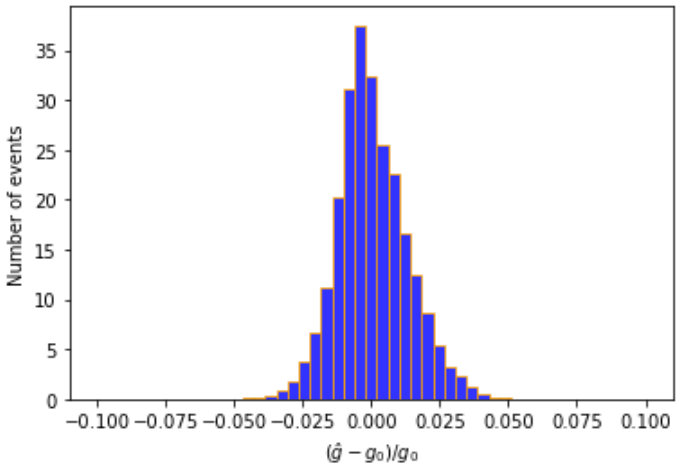

Figure I.21: Histogram of estimators $\hat{g}$ for 10000 random draws in the case of the cylindrical chamber.

$R_d = 2$ cm symmetrically positioned above and below the trap at distance $H_d = 1$ cm. In figure I.22-**b**, we show schematically the trap (which is the source of anti-atoms) and the obstacles surrounding it (such as the electrodes of the ion trap and the lenses of the laser cooling). The symmetrical configuration produces a simple geometry which will be more easily studied in Monte-Carlo simulations of the experiment. We will work with a horizontal polarization of the photodetachment laser ($\theta_n = \pi/2$) in order to launch the atoms preferably in the free interval between the two disks.

The disks are absolutely needed for the experiment [99, 100] as they hide the complexity of the trap. However, they intercept some trajectories of free falling anti-atoms

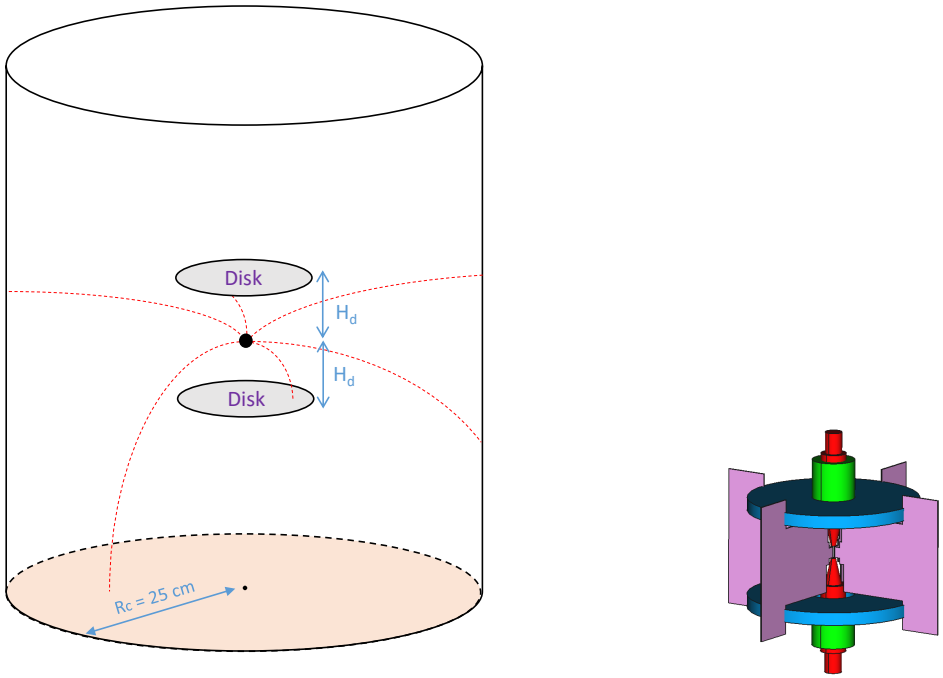

Figure I.22: **a** - Cylindrical chamber with two disks symmetrically positioned above and below the trap at distance H_d. **b** - Schematic representation of the ion trap. Electrodes are in red, the lenses are in purple and the two disks are in blue. The structure that supports the trap is not represented.

and they reduce the number of annihilated events. In the following, we fix the initial number N of atoms but our analysis of dispersion accounts for the fact that the number of events N_c detected on the surfaces of the chamber is smaller than N.

One might simply think that these obstacles are detrimental as they reduce the number of annihilated events, leading to a loss of accuracy. We will show however that the opposite happens, with a significantly improved accuracy on the measurement of $\bar{g}$, thanks to the information gained from the boundaries of intercepted trajectories which depend on $\bar{g}$.

I.4.1 Distribution of annihilation events with disks

The conditions to reach the upper disk from the trap are:

$$v_{z_0} > 0 \quad , \quad v_{z_0} t_{\text{apo}} - \frac{g}{2} t_{\text{apo}}^2 > H_d \quad , \quad t_{\text{reach-disk}} < t_{\text{disk}}. \tag{I.72}$$

with

$$t_{\text{apo}} = \frac{v_{z0}}{g} \quad , \quad t_{\text{reach-disk}} = \frac{v_{z0} - \sqrt{v_{z0}^2 - 2gH_d}}{g} \quad , \quad t_{\text{disk}} = \frac{R_{\text{d}} - \sqrt{x_0^2 + y_0^2}}{\sqrt{v_{x_0}^2 + v_{y_0}^2}}. \tag{I.73}$$

The condition to reach the lower disk from the trap is:

$$v_{z_0} t_{\text{disk}} - \frac{g}{2} t_{\text{disk}}^2 < H_d. \tag{I.74}$$

On the figure I.23 of the 2D current on the walls as function of z and t, one clearly sees the sharp boundaries of the shadow induced on the walls by the presence of the disks. The position in space and time of this shadow depends on the value of g and its detection allows to gain information on the value of g.

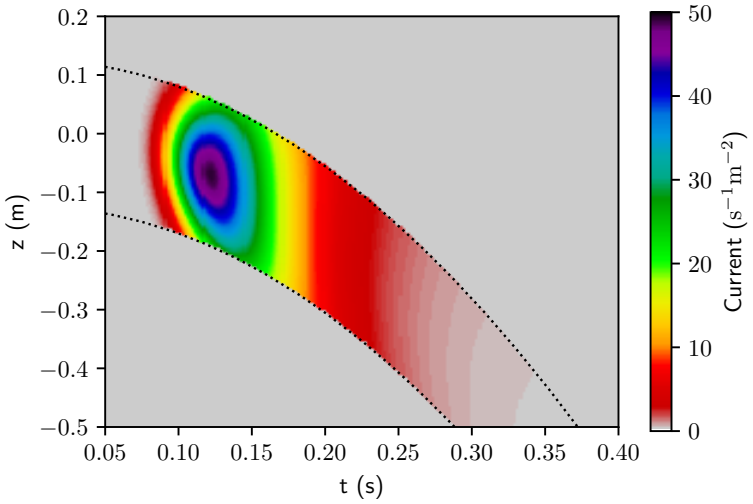

Figure I.23: Distribution of annihilation events J on the walls of the altitude z and time of flight t. The shadow zone is represented in grey. Parameters: $f = 1$ MHz, $\delta E = 30$ μeV and horizontal polarization of the laser.

The figure I.24 illustrates that modifying the value of g changes the shadow area, here for $g = 0.8\ g_0$, $g = 0.8\ g_0$ and $g = 1.2\ g_0$.

The critical time t_c of the steps induced by the disks depends on the detection point (x, y, z) considered. Note that the critical time induced by the disk is necessarily lower than the one induced by the ceiling. For example if we consider a detection point on the walls at $z = -17$ cm, then the value of the critical times induced by the upper and lower disks are:

$$\text{Upper disk :} \quad t_c = \sqrt{\frac{2}{g} \frac{z - R_c/R_d|H_d|}{R_d/R_c - 1}} \approx 0.256\ s; \tag{I.75}$$

$$\text{Lower disk :} \quad t_c = \sqrt{\frac{2}{g} \frac{z + R_c/R_d|H_d|}{R_d/R_c - 1}} \approx 0.1\ s. \tag{I.76}$$

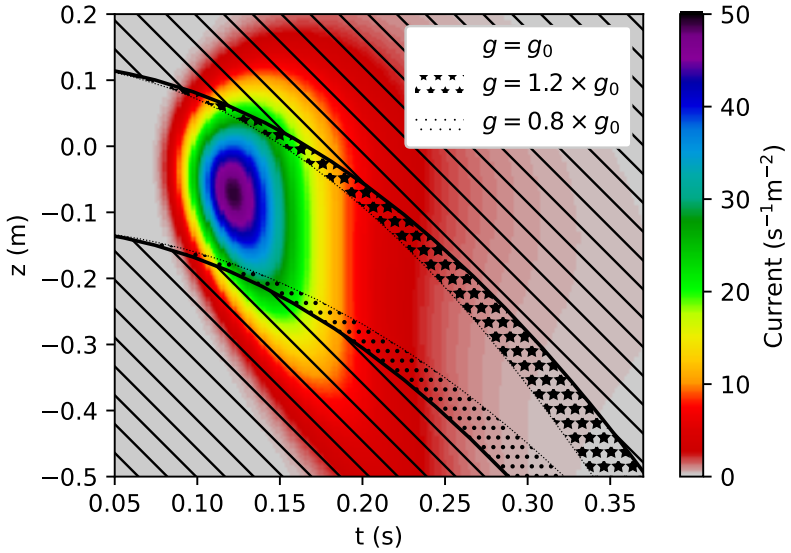

Figure I.24: Current J as a function of z and t. The area with diagonal hatching represents the shadow from the two disks for g_0. The two dotted areas represent zones that are not in the shadow for $g = g_0$ but are in the shadow for $g = 1.2\ g_0$ and $g = 0.8\ g_0$.

Those critical times are clearly apparent in the figure I.25 of annihilation times, drawn at the fixed altitude $z = -17$ cm.

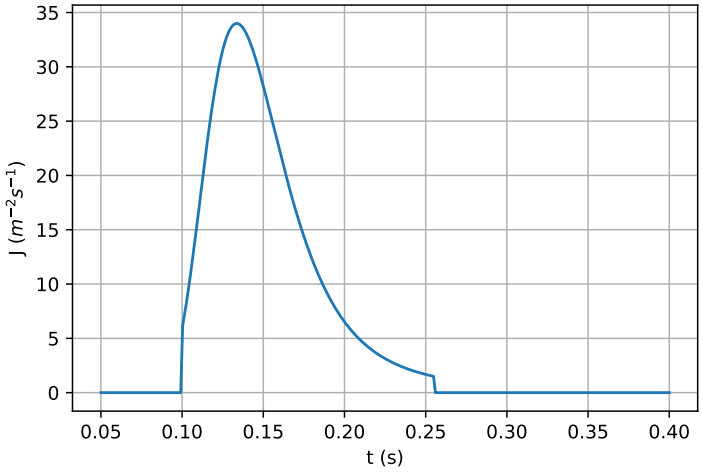

Figure I.25: Distribution of annihilation times, at $z = -17$ cm. Same parameters as figure I.23.

A random draw of Monte-Carlo detection events is represented in figure I.26 on the

floor and on the walls. Trajectories hitting the disk lead to annihilation there, and are discarded from the forthcoming analysis as they contain no useful information on the value of g. About 60% of the initial atoms are detected, while the other 40% are annihilated on the disks. On the walls, we observe two main groups of detection for $\phi = \pm 90^o$ (azimuth angle), due to the horizontal polarization of the laser. There is no detection events on the ceiling due to the presence of the upper disk which intercepts upward trajectories.

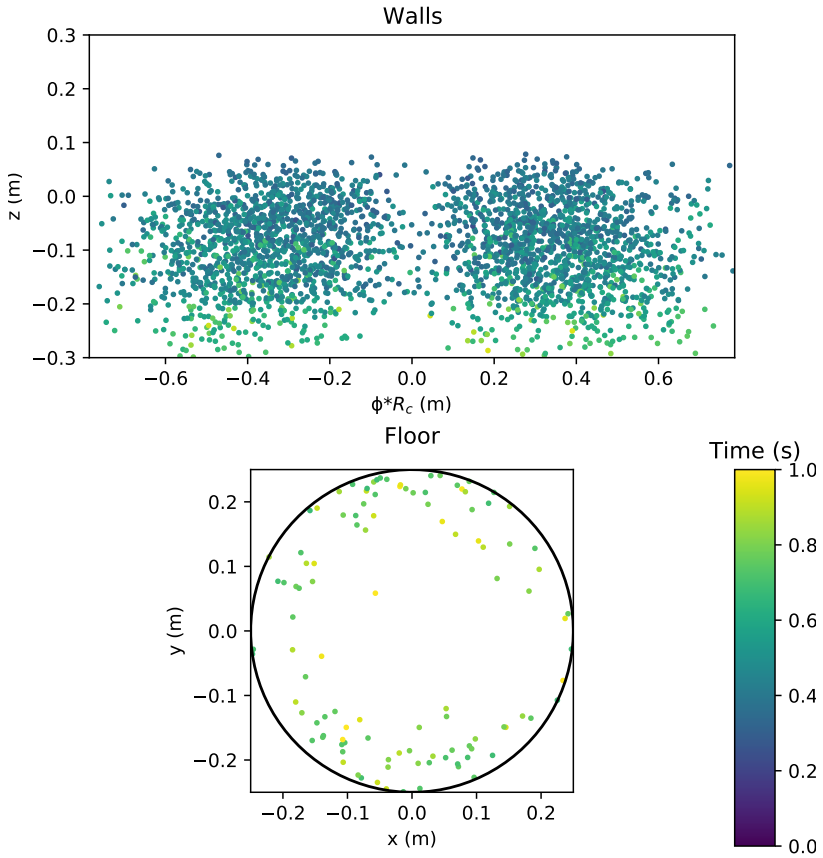

Figure I.26: Monte-Carlo generation of $N = 5000$ events. Distribution of events: 3% on the floor, 97% on the walls, 0% on the ceiling. Horizontal polarization of the laser.

I.4.2 Monte-Carlo analysis with disks

The parameters used are the same as the ones used for the previous designs, they are indicated in table I.1. Figure I.27 shows likelihood functions calculated for random draws of $N = 1000$ atoms. They are nearly flat, with sudden drops to zero. This behaviour is

due to the presence of obstacles and it can be qualitatively understood. Let us consider a position r and time of flight t reached by an atom for $g = g_0$. If this impact is close to the boundary of allowed area, and because the boundary depends on g, the impact may be in the shadow of the disk for a different value of g. Beyond this boundary, the likelihood drops to zero. The effect of the shadow and the presence of the critical time t_c is visible in the likelihood function.

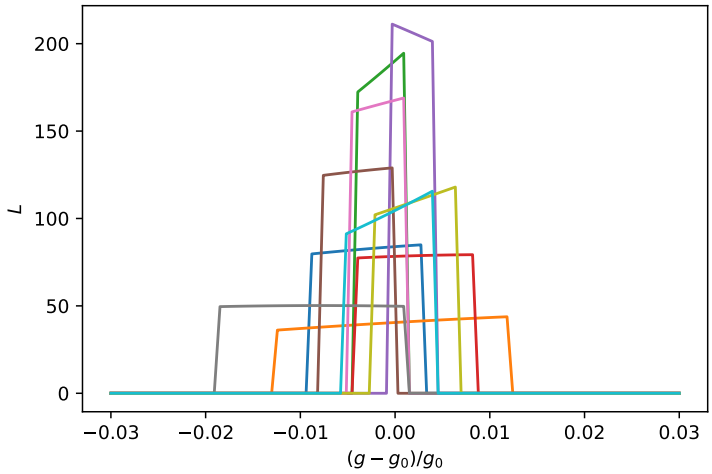

Figure I.27: Sample of 10 likelihoods, plotted for $N = 1000$ events, for the geometry with disks.

As mentioned previously, the usual method is to estimate the value of g by maximizing the likelihood (see equation (I.52)). However, we saw that with the current design, the likelihood functions don't have gaussian shape. They have trapezoidal shapes with an inclined plateau. Hence, their maximum will then fall on either side of the plateau of the likelihood function, which means that Maximum Likelihood Estimation is no longer the adapted method. This problem can be solved by defining a new estimator $\widehat{g}_{\text{mean}}$ as the mean value of the likelihood function [108]:

$$\widehat{g}_{\text{mean}} = \frac{\int g\mathcal{L}(g)dg}{\int \mathcal{L}(g)dg}. \tag{I.77}$$

The histogram of distribution obtained with this estimator is represented in figure I.28. The shape of the histogram is symmetrical and its bias is small because the disks are symmetrically positioned above and below the trap. The estimator $\widehat{g}$ is then unbiased and its distribution is a Laplace distribution:

$$f(g) = \frac{1}{\sqrt{2}\sigma_g} \exp\left(-\frac{|g - g_0|}{\sqrt{2}\sigma_g}\right). \tag{I.78}$$

where σ_g the dispersion of $\widehat{g}$ which scales as $1/N$ [117]. We note that if the two disks are not symmetric, then the estimator $\widehat{g}$ is biased.

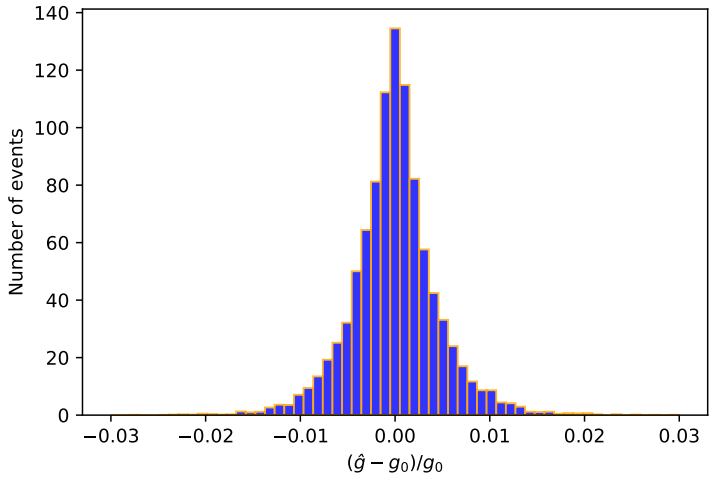

Figure I.28: Normalized histogram of estimators $\widehat{g}$ for 10000 random draws, for the geometry with disks.

Precise values of the bias and accuracy obtained with both estimators is indicated in the table I.4. The calculated value of the bias could be different for another simulation (it also shows fluctuations) but it would in any case remain much smaller than the dispersion.

Estimator	**Bias ± dispersion**
$\widehat{g}_{\text{max}}$	$-\ 0.01\%\ \pm\ 0.80\%$
$\widehat{g}_{\text{mean}}$	$-\ 0.001\%\ \pm\ 0.36\%$

Table I.4: Bias $(\mu_g - g_0)/g_0$ and Relative uncertainty σ_g/g_0 obtained with the design with disks, when using the estimators $\widehat{g}_{\text{max}}$ and $\widehat{g}_{\text{mean}}$.

We see that the Mean Likelihood Estimator $\widehat{g}_{\text{mean}}$ leads to smaller bias and relative uncertainty, which confirms the relevance of this estimator that we have introduced. Moreover, we also see that the accuracy is better than in the case without disks (2.93%), even if less atoms are detected. Indeed, extra information on the value of g comes with the presence of shadow borders on the detection area (the position of which depends on g).

We will now vary the radius of the disks R_d and their distance from the trap H_d to evaluate their effect on the accuracy. This will justify the values of the parameters previously used in this part ($R_d = 2$ cm and $H_d = 1$ cm).

Disk parameters We vary R_d from 0 to 4 cm and H_d from 0 cm to 2.5 cm with full cylindrical chamber. By increasing the radius of the disk (R_d) and by decreasing the distance trap-disk (H_d), the effect of the cut increases but the number of atoms detected decreases (see figure I.29, upper plot). So there should be optimal parameters to get the

best precision of the measurement. In the lower plot of figure I.29, we observe that the optimal result is obtained around $R_d = 2$ cm and $H_d = 1$ cm, which explains why we use those parameters in our simulations.

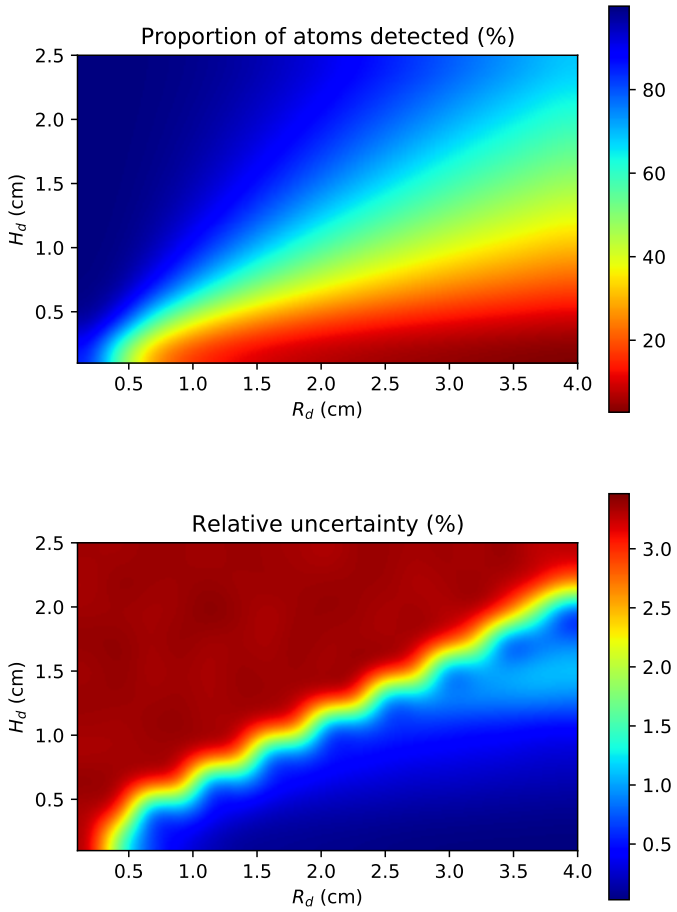

Figure I.29: Effect of disk radius R_d and distance from the trap H_d on the proportion of atoms detected (upper plot) and relative uncertainty σ_g/g (lower plot).

I.4.3 Smoothing of the current

The steps in the current lead to a Dirac distribution in the derivative of the current with respect to g and make the Cramer-Rao statistical method unapplicable, as the dispersion σ_g^{CR} is calculated from the Fisher information which is thus an ill-defined integral (the integrand diverges at the steps). This difficulty is purely formal as the steps are rounded up by the experimental details of the timing measurement. The uncertainty on the STOP

signal given by the Micromegas detectors, of the order of a few tenths of nanoseconds, is largely dominated by the uncertainty in the START signal, that is the finite duration of the photodetachment process. The experimentally detected current is a convolution of the current calculated above by the distribution of START time. The convolution rounds up the steps and brings the current back inside the domain of applicability of the Cramer-Rao method. In order to describe the rounding up mechanism, we introduce a smooth distribution δ_τ of width τ for the START signal. The model distribution of the START time used is the logistic distribution (see figure I.30):

$$\delta_\tau(t_0) = \frac{1}{4\tau \cosh^2(\frac{t_0}{2\tau})}. \tag{I.79}$$

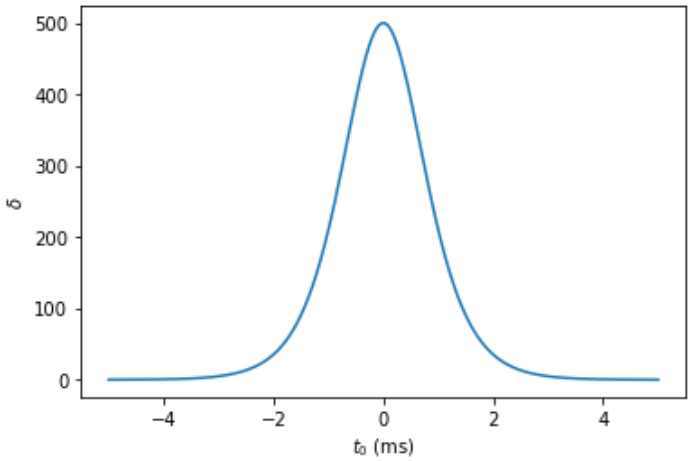

Figure I.30: Logistic distribution δ_τ, with $\tau = 500\ \mu s$.

The total time is now:

$$T = t_0 + t \tag{I.80}$$

where t_0 is the photodetachment time (within the distribution of width τ) and t the time of flight. The experimentally measured current J_τ is the convolution product of the function J by the distribution δ_τ of time t_0:

$$J_\tau(\boldsymbol{r}, T) = \int J(\boldsymbol{r}, T - t_0)\delta_\tau(t_0)dt_0. \tag{I.81}$$

J_τ can be computed analytically or numerically. After the convolution, the step at t_c in J in rounded up on a time of the order of τ. Currents calculated before and after the convolution on a cut with fixed altitude $z = -17$ cm are represented in figure I.31. Due to the small value of τ compared to the variation time scale in J, the convolution doesn't change appreciably the current, except in the vicinity of the steps. Indeed, the effect of the dispersion on t_0, calculated here for $\tau = 500\ \mu$s, is visible at the steps of the current corresponding to edges of the shadow of the disks.

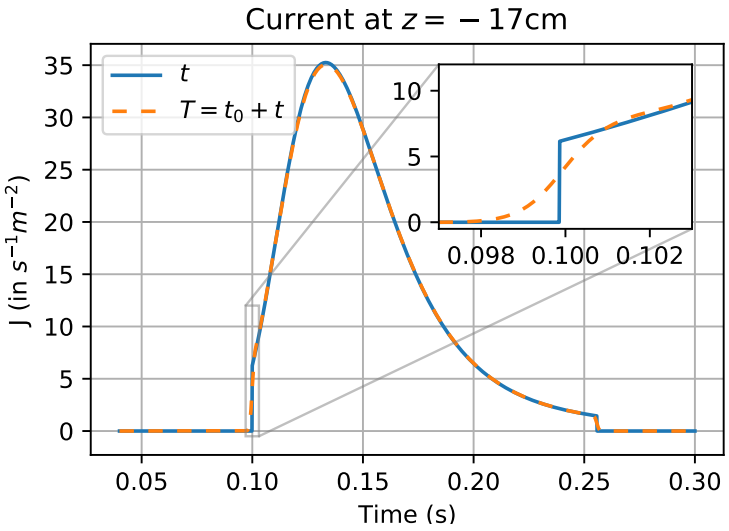

Figure I.31: Comparison between the currents $J(\boldsymbol{r}, t)$ and $J_\tau(\boldsymbol{r}, T)$ calculated with the same parameters as in figure I.25, the first one before the convolution, the second one after the convolution with $\tau = 500$ μs [117]. The effect of the dispersion on t_0 is visible on the edges of the shadow zone induced by the obstacles.

The relative uncertainty obtained with smoothing is slightly higher than the case without smoothing, which had of course to be expected:

$$\sigma_g/g \approx 0.58\%. \tag{I.82}$$

Variation with N and statistical efficiency Normalised likelihood functions are represented on figure I.32 for different values of N. For $N = 10$ and $N = 100$, the likelihoods are mostly flat with sudden drops to zero. The drop to zero is rounded up by the dispersion τ, with the rounding negligible for $N = 10$ or $N = 100$ but starting to be noticeable for $N = 1000$. For $N = 10000$, the likelihoods are closer to Gaussian functions because the numerous annihilation events produce an efficient sampling of the rounded step.

To illustrate the effect of the cut induced by the disks and analyze regimes of statistical efficiency, we draw in figure I.33 the predictions of Monte-Carlo/likelihood simulations versus the number N of events in a given random draw. We have compared them to the predictions deduced from Cramer-Rao bound, taking into account the contribution of the rounded step (orange line) or not taking it into account (green line).

In figure I.33, we can distinguish 2 regimes. For small values of N ($N < 1000$), the Monte-Carlo uncertainties follow a $1/N$ regime (the events close to the cut improve the accuracy); the presence of the disks brings information but not enough to reach the good efficiency limit. In this regime, the likelihoods are not gaussian (see figure I.32) and the

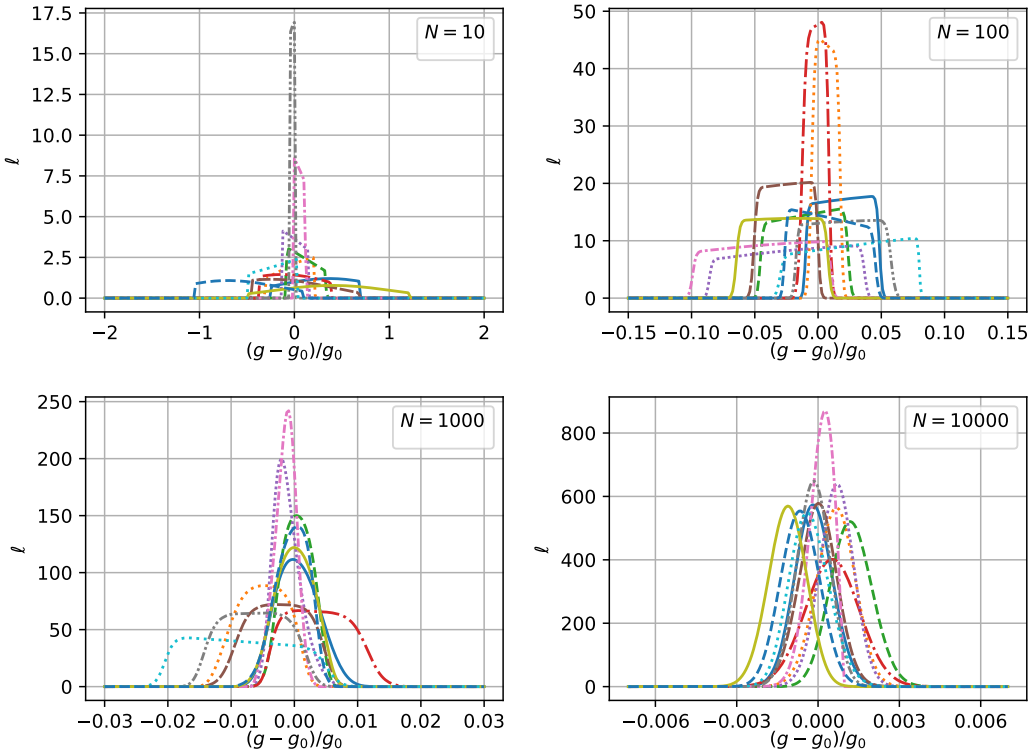

Figure I.32: Set of normalised likelihood for different values of the initial number of atoms N for $\tau = 500$ μs.

shape of the histogram is a Laplace distribution. For large values of N ($N >> 1000$), the Monte-Carlo uncertainties follow a $1/\sqrt{N}$ regime and approaches the Cramer-Rao bound with cut; the number of events in the vicinity of the step becomes sufficient so that statistical efficiency is recovered. In this regime, the likelihoods are nearly gaussian (see figure I.32), as well as the associated histogram. An analytical model is proposed in [117] to explain this behaviour.

In the following part, we will make the analysis more complete by evaluating the effect of quantum reflection of $\bar{H}$ atoms on the Casimir-Polder potential in the vicinity of matter surfaces of the free fall chamber [13].

I.5 Taking into account quantum reflection

Quantum reflection is a uniquely quantum phenomenon in which an atom or a small molecule is reflected in a wavelike fashion from an attractive surface. It is described in details in appendix B. As quantum reflection probability is not null at velocities of experimental interest, it is necessary to take this effect into account in the data analysis

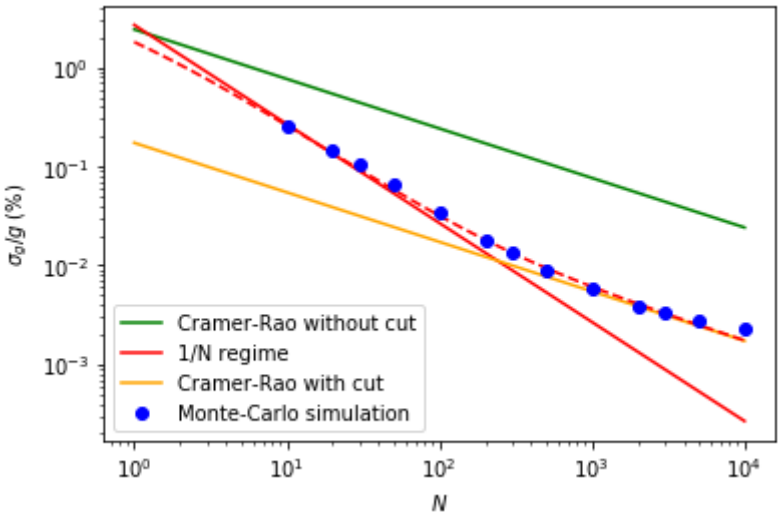

Figure I.33: Uncertainty on the estimation of g as function of the number N of initial events for $\tau = 500$ μs. The green line corresponds to the Cramer-Rao bound without disks and the orange one to the Cramer-Rao bound with disks using $\tau = 500$ μs. Both Cramer-Rao bounds scale as $1/\sqrt{N}$.

for GBAR and avoid systematic errors which could be due to reflected atoms.

A very good polishing of the chamber boundaries is mandatory for preventing diffuse quantum reflection. In this case, reflected atoms can be eliminated from the data analysis by using discrimination time windows (for example, atoms with an initial vertical velocity bouncing on the floor after a time t will touch it again after a further time $2t$). If quantum reflection is well mastered, it is even possible to take reflected atoms into account in the analysis, thus improving the statistics.

I.5.1 Quantum reflection probability

Ultra cold anti-hydrogen atoms falling onto the detection plate will suffer a quantum reflection before touching the plate and this will affect the measurement of the free fall [13, 14, 118]. Quantum reflection of antihydrogen on a plate depends on the component of the velocity orthogonal to the plate and on optical properties of the material. We assume boundaries to be well polished stainless steel plates behaving as good optical mirrors in the visible and near-IR domains. A good approximation of quantum reflection probabilities is obtained by taking the values calculated for a plate perfectly reflecting electromagnetic fields [13]. Quantum reflection probability depends on the atomic wavevector $k_\perp$ that is equivalently the orthogonal velocity $|v_b|$:

$$k_\perp = \frac{m}{\hbar}|v_b|. \tag{I.83}$$

Quantum reflection probability $|r|^2$ has known asymptotic behaviours at low and high values of these parameters. In particular, the low-energy behaviour is determined by the

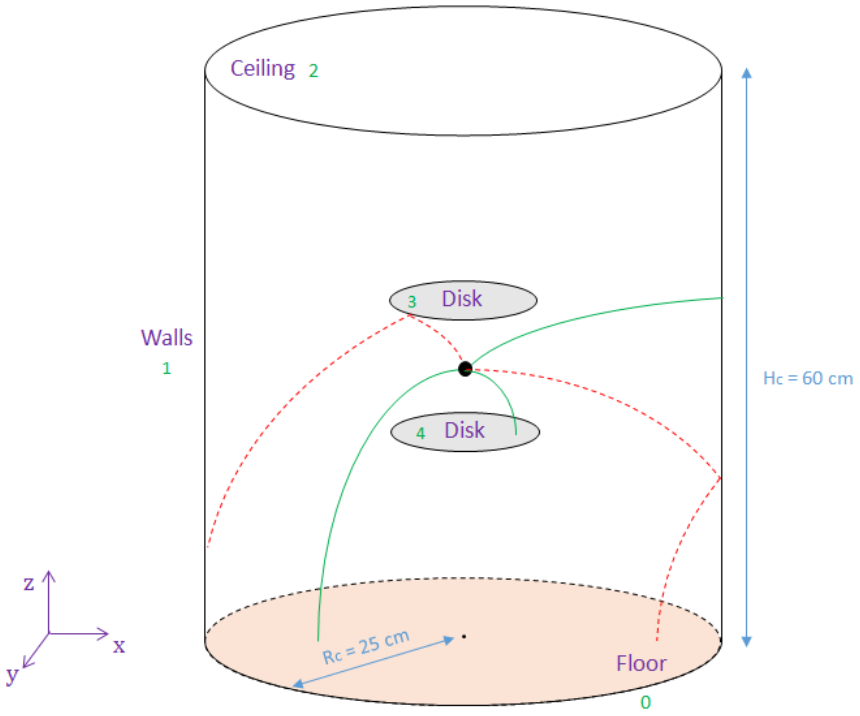

Figure I.34: Cylindrical chamber with disks, accounting for quantum reflection. Direct trajectories are represented with green full lines and QR trajectories are represented with red dotted lines.

imaginary part b of the scattering length, itself determined by the optical parameter of the mirror:

$$|r|^2 = e^{-4|b|k_\perp} = e^{-4B|v_b|} \quad , \quad \text{with} \quad B = |b|\frac{m}{\hbar}. \tag{I.84}$$

For a mirror perfectly reflecting electromagnetic fields (as stainless steel with good polishing), the module of the scattering length is [72]:

$$|b| \approx 543.345\ a_0 \approx 28.75\ \text{nm}. \tag{I.85}$$

with $a_0 \approx 5.29 \cdot 10^{-11}$ m the Bohr radius.

More precisely, an interpolation formula has been designed to reproduce accurately the intermediate and high-energy parts of the numerically calculated curves [72]:

$$|r|^2 = \exp\left(-\frac{4\kappa}{1+\frac{\alpha\kappa^{2/3}}{1+\beta\kappa^{-1}}}\right) \quad , \quad \kappa = |b|\frac{m}{\hbar}|v_b|. \tag{I.86}$$

The constants α and β have been obtained by a least-squares fit on the numerically calculated curves. For a perfect EM, we have:

Different velocities correspond to neatly different probabilities, so that it is necessary to account for the variation of quantum reflection for each individual trajectory. The

	$\boldsymbol{\alpha}$	$\boldsymbol{\beta}$
Perfect EM	0.708810	0.516300

dependence between the probability of quantum reflection and the orthogonal velocity is represented in figure I.35, where we observe that $|r|^2$ decreases when $|v_b|$ increases.

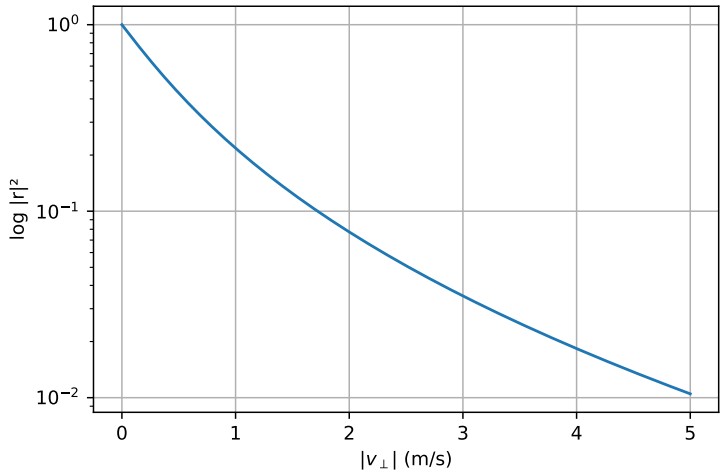

Figure I.35: Relation between the probability of quantum reflection $|r|^2$ (with log scale) and the orthogonal velocity $|v_b|$.

In particular, for an atom having initial vertical velocity $v_{z_0} = 0$ and falling down to a perfect EM mirror from a height $H = 30$ cm, the probability of quantum reflection is:

$$|v_b| = \sqrt{2gH} \approx 2.43 \text{ m/s} \rightarrow |r|^2 \approx 5.4\%. \tag{I.87}$$

Quantum reflection probabilities are higher on the disks (since the height H_d between the trap and the disks is 1 cm), and they can give rise to systematic effects of the same order of magnitude as the statistical accuracy looked for in GBAR experiment.

I.5.2 Current with quantum reflection

The reflected atoms are not be detected at the expected time, leading to a loss in statistics. Moreover, higher energy atoms are less affected by quantum reflection and are thus more likely to be detected. Accurately modeling quantum reflection is therefore necessary to correct this bias.

From a given detection point $(\boldsymbol{r}, t)$, we have to find back the initial velocity $\boldsymbol{v}_0$. There is a one to one matching between those values, but the relation between detection position and initial velocity depends on the existence of a reflection and the detection surface on which it happened. A detection point on a surface of the chamber can be reached directly

or by having undergone one or several reflections on the disks or on another surface of the chamber (see figure I.34). As elementary quantum reflection probabilities on detection surfaces are of the order of 5% and as the radius of the disks is small, we disregard in this analysis the case of multiple quantum reflections.

The probability current at detection point is obtained by adding the contribution of the different cases, with the probabilities associated:

$$J(\boldsymbol{r},t) = J_{\rm dir}(\boldsymbol{r},t) + \sum_s J_{\rm QR}^{(s)}(\boldsymbol{r},t) \tag{I.88}$$

where $J_{\rm dir}(\boldsymbol{r},t)$ is the contribution of the direct trajectory and $J_{\rm QR}^{(s)}(\boldsymbol{r},t)$ comes from the quantum reflection by the surface s. Each of the latter expressions contains the associated quantum reflection probability. For example, for a detection point on the floor, the total current is:

$$\begin{aligned} J(\boldsymbol{r},t) \quad = \quad & J_{\rm floor}(\boldsymbol{r},t) + J_{\rm QR}^{(\rm floor)}(\boldsymbol{r},t) + J_{\rm QR}^{(\rm walls)}(\boldsymbol{r},t) \\ & + J_{\rm QR}^{(\rm upper\ disk)}(\boldsymbol{r},t) + J_{\rm QR}^{(\rm lower\ disk)}(\boldsymbol{r},t). \end{aligned} \tag{I.89}$$

For a direct trajectory, the analytical expression of the current is:

$$J_{\rm dir}(\boldsymbol{r},t) = (1-p(v_\perp))\frac{m^3|v_\perp|}{t^3}\Pi_0(\boldsymbol{p}_0) \tag{I.90}$$

with $p(v_\perp)$ the probability of quantum reflection on the detection surface (the expression of which is given by equation I.86) and $v_\perp$ the orthogonal velocity at detection.

For a trajectory with QR on vertical surface (walls), we have:

$$J_{\rm QR}^{(s)}(\boldsymbol{r},t) = p(v_b)\frac{m^3|v_\perp|}{t^2\left|\frac{dz}{dv_{z_0}}\right|}\Pi_0(\boldsymbol{p}_0) = p(v_b)\frac{m^3|v_\perp|}{t^3}\Pi_0(\boldsymbol{p}_0) \tag{I.91}$$

with v_b the orthogonal velocity on the reflection surface and $v_\perp$ the orthogonal velocity on the detection surface. For a trajectory with QR on horizontal surface (floor or disks), we have:

$$J_{\rm QR}^{(s)}(\boldsymbol{r},t) = p(v_b)\frac{m^3|v_\perp|}{t^2\left|\frac{dz}{dv_{z_0}}\right|}\Pi_0(\boldsymbol{p}_0) = p(v_b)\frac{m^3|v_\perp|}{t^2(t-t_b)}\Pi_0(\boldsymbol{p}_0). \tag{I.92}$$

with t_b the time of bouncing on the horizontal surface.

How can we get t_b ? For the cases of one quantum reflection on a horizontal surface (at height z_b), the orthogonal velocity at bouncing v_b can be written:

$$|v_b| = \tfrac{z_b}{t_b} + \tfrac{g}{2}t_b \quad , \quad |v_b| = \tfrac{z-z_b}{t-t_b} + \tfrac{g}{2}(t-t_b) \tag{I.93}$$

$$\rightarrow -\tfrac{z_b}{t_b} - \tfrac{g}{2}t_b + \tfrac{z-z_b}{t-t_b} + \tfrac{g}{2}(t-t_b) = 0. \tag{I.94}$$

By isolating t_b, we get a 3^{rd} degree polynomial equation:

$$A\ t_b^3 + B\ t_b^2 + C\ t_b + D = 0 \tag{I.95}$$

$$A = 1 \quad , \quad B = -\tfrac{3}{2}t \quad , \quad C = \tfrac{-2z_b+z}{g} + \tfrac{t^2}{2} \quad , \quad D = \tfrac{z_b t}{g}.$$

The bouncing time t_b is obtained by solving numerically this equation with the module `numpy.roots` in `Python`. Moreover, we only keep the solutions that satisfy the following conditions (with t_d time spent above the reflecting surface):

$$t_b > t_0 \quad , \quad t_b < t_d \quad , \quad t_b + 2\frac{|v_b|}{g} > t_d \ . \tag{I.96}$$

Once t_b is obtained, the initial velocity is

$$v_{z_0} = \frac{z_b}{t_b} + \frac{g}{2}t_b. \tag{I.97}$$

I.5.3 Different cases of quantum reflection

Case walls → floor When the atom is reflected on the walls and is detected on the floor at position $(x, y, 0)$, we consider the "mirror" point symmetric to the detection position relative to the walls. Its coordinates are $(x_m, y_m, z_m) = (r_m \cos\theta, r_m \sin\theta, 0)$, with $r_m = 2R_c - \sqrt{x^2 + y^2}$ and $\theta = \arctan(y/x)$. The initial velocity is given by:

$$v_{x_0} = \frac{x_m}{t} \quad , \quad v_{y_0} = \frac{y_m}{t} \quad , \quad v_{z_0} = \frac{z}{t} + \frac{gt}{2} \ . \tag{I.98}$$

The orthogonal velocity on the reflection surface (walls) is $v_{xy} = \sqrt{v_{x_0}^2 + v_{y_0}^2}$ and the one on the detection surface (floor) is $v_z = v_{z_0} - gt$. The expression of the current is:

$$J_{\mathrm{QR}}^{(\mathrm{walls})}(\boldsymbol{r}, t) = p(v_{xy})\frac{m^3|v_z|}{t^3}\Pi_0(\boldsymbol{p}_0). \tag{I.99}$$

Case walls → walls When the atom is reflected on the walls and is detected on the walls at position (x, y, z), we consider the point symmetric to the detection position relative to the opposite walls. We note it $(x_m, y_m, z_m) = (r_m \cos\theta, r_m \sin\theta, z)$, and the initial velocity is given by:

$$v_{x_0} = \frac{x_m}{t} \quad , \quad v_{y_0} = \frac{y_m}{t} \quad , \quad v_{z_0} = \frac{z}{t} + \frac{gt}{2} \ . \tag{I.100}$$

The orthogonal velocity on the reflection surface and detection surface (walls) is $v_{xy} = \sqrt{v_{x_0}^2 + v_{y_0}^2}$. The expression of the current is:

$$J_{\mathrm{QR}}^{(\mathrm{walls})}(\boldsymbol{r}, t) = p(v_{xy})\frac{m^3|v_{xy}|}{t^3}\Pi_0(\boldsymbol{p}_0). \tag{I.101}$$

Case upper disk → floor When the atom is reflected on the upper disk and is detected on the floor, the initial velocity is given by:

$$v_{x_0} = v_x = \frac{x}{t} \quad , \quad v_{y_0} = v_y = \frac{y}{t} \quad , \quad v_{z_0} = \frac{z_b}{t_b} + \frac{g}{2}t_b \ . \tag{I.102}$$

We denote H_d the height between the trap and the upper disk (> 0). The orthogonal velocity on the reflection surface (upper disk) is $v_b = \sqrt{v_{z_0}^2 - 2gH_d}$. The time of bounce t_b is obtained by solving the cubic equation:

$$A\ t_b^3 + B\ t_b^2 + C\ t_b + D = 0 \tag{I.103}$$
$$A = 1 \quad , \quad B = -\tfrac{3}{2}t \quad , \quad C = \tfrac{-2z_b+z}{g} + \tfrac{t^2}{2} \quad , \quad D = \tfrac{z_b t}{g}\ .$$

The expression of the current is:

$$J_{\mathrm{QR}}^{(\text{upper disk})}(\boldsymbol{r}, t) = p(v_b)\frac{m^3|v_z|}{t^2(t-t_b)}\Pi_0(\boldsymbol{p}_0). \tag{I.104}$$

Case upper disk → walls The relations are the same as the case "upper disk → floor", the only difference being the orthogonal velocity at detection:

$$J_{\mathrm{QR}}^{(\text{upper disk})}(\boldsymbol{r}, t) = p(v_b)\frac{m^3|v_{xy}|}{t^2(t-t_b)}\Pi_0(\boldsymbol{p}_0) \quad , \quad v_{xy} = \sqrt{v_{x_0}^2 + v_{y_0}^2}. \tag{I.105}$$

Case lower disk → floor We denote H_d the height between the trap and the upper disk (< 0). The relations are the same as the case "upper disk → floor", the only difference being that we take $H_d < 0$.

Case lower disk → walls The relations are the same as the case "lower disk → floor", the only difference being the orthogonal velocity at detection $|v_{xy}| = \sqrt{v_{x_0}^2 + v_{y_0}^2}$.

I.5.4 Distribution of events and figures of the current

The fraction of atoms that reach the surfaces of the detection chamber is about 66% (the other 34% are annihilated on the disks and lost for our analysis) while 18% of the detected atoms have been reflected on another surface before their detection.

We represent in figure I.36 the current on the walls as function of time t and position coordinate z. The essential information on these plots is that quantum reflections allow atoms to reach the zone which was previously forbidden (figure I.23). This "shadow" zone represents $\sim 2.5\%$ of all the detection. We also observe that there remains a small forbidden zone which cannot be reached by any trajectory even when taking into account quantum reflections.

A Monte-Carlo random draw of $N = 5000$ initial atoms is represented in figure I.37, where red points correspond to detection events which have been reflected on another surface before their detection. Quantum reflection increases the proportion of atoms detected on the floor (13%), compared to the case without quantum reflection (3%).

We represent in figure I.38 the likelihood functions calculated for random draws of $N = 1000$ $\bar{H}$ atoms. We clearly see that the likelihoods are not Gaussian and contain different steps, in particular due to interception of some trajectories by the disks. We also notice that some likelihood functions are significantly biased.

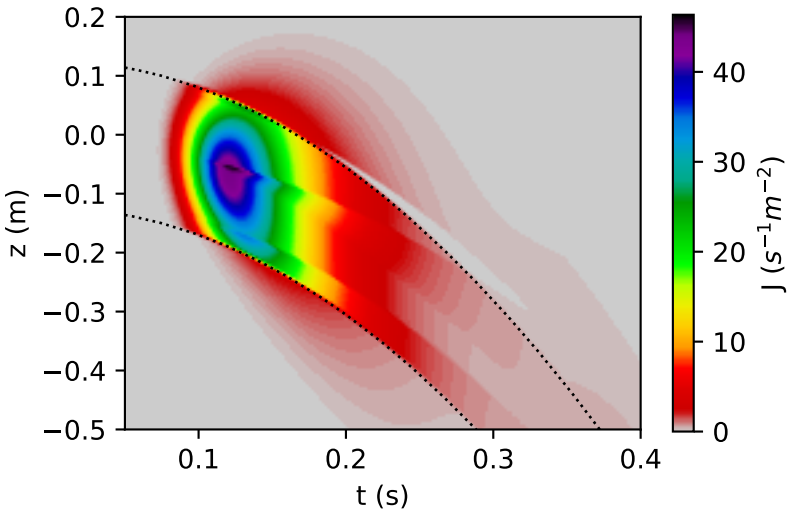

Figure I.36: Distribution of annihilation events ($J(\boldsymbol{R}, T)$ in $\mathrm{m}^{-2}s^{-1}$) on the walls as a function of t and z. The shadow zone is represented in grey color. Parameters: cylindrical chamber with disks and QR, horizontal polarization of the laser.

We then show in figure I.39 this histogram of the estimator $\hat{g}$ which follows a Laplace distribution as in the case without quantum reflection (figure I.28).

The dispersion found with disks by taking into account quantum reflection is, with the Monte-Carlo method:

$$\sigma_g/g \approx 0.84\%. \tag{I.106}$$

Accounting for quantum reflection doesn't degrade that much the accuracy compared to the case without quantum reflection (0.36%), provided that quantum reflection is mainly specular. Quantum reflection processes lead to detection in the shadow zone, which slightly reduces the advantage associated with the information coming from shadows borders. But it doesn't suppress the advantage as the accuracy is still improved with respect to the value of $\simeq 2.93\%$ obtained in the absence of shadow borders. For completeness, we also evaluated the confidence intervals containing 95% of the probability in the histogram of the estimators $\hat{g}$:

$$I_c = [9.751\ ;\ 9.868]\ , \quad \text{without taking into account QR}\ ; \tag{I.107}$$

$$I_c = [9.733\ ;\ 9.895]\ , \quad \text{accounting for quantum reflection.} \tag{I.108}$$

As could be expected, the confidence intervals are larger than if they were calculated for a Gaussian distribution with the known standard deviations. However, there is no significant difference in this respect associated with quantum reflection.

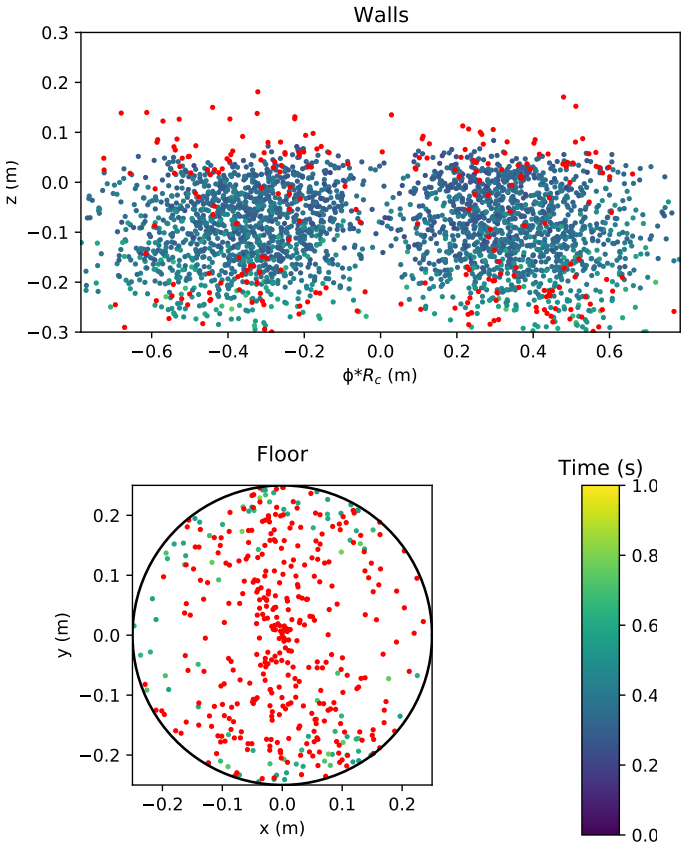

Figure I.37: Monte-Carlo generation of $N = 5000$ events, where the color indicates the time of flight t for direct trajectories and where quantum reflected trajectories are represented with red color. Distribution of events: 13% on the floor, 87% on the walls, 0% on the ceiling.

I.6 Conclusion of chapter I and discussions

In this chapter, we have evaluated the accuracy to be expected for the measurement of free fall acceleration g of antihydrogen in the GBAR experiment with the values of parameters indicated in table I.1, accounting for the recoil transferred in the photodetachment process. Using Monte-Carlo simulations and analytical calculations of the Cramer-Rao bound, we have shown that the final accuracy is determined mainly by the initial velocity distribution before photodetachment. The recoil velocity associated to photodetachment doesn't add noise in the data analysis even when its variance is larger than that of initial gaussian velocities. This is due to the fact that the components of recoil velocity have strong correlation (they lie on a sphere), a property which has been used in our analysis to minimize their contribution to final uncertainty. The results obtained here thus reduce

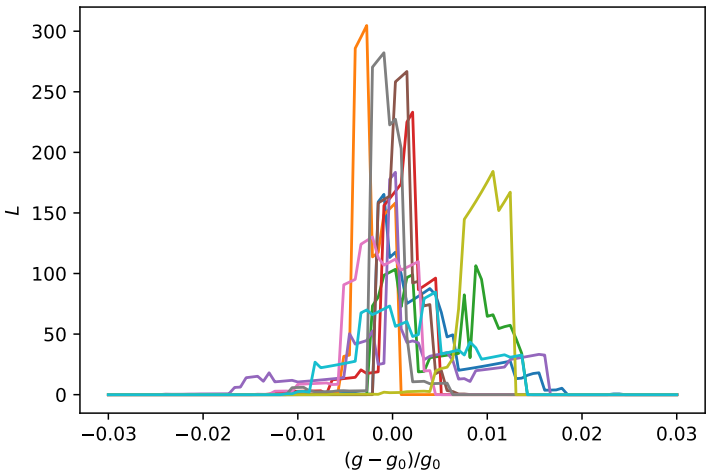

Figure I.38: Sample of 10 normalized likelihoods including quantum reflections calculated for independent random draws of 1000 atoms.

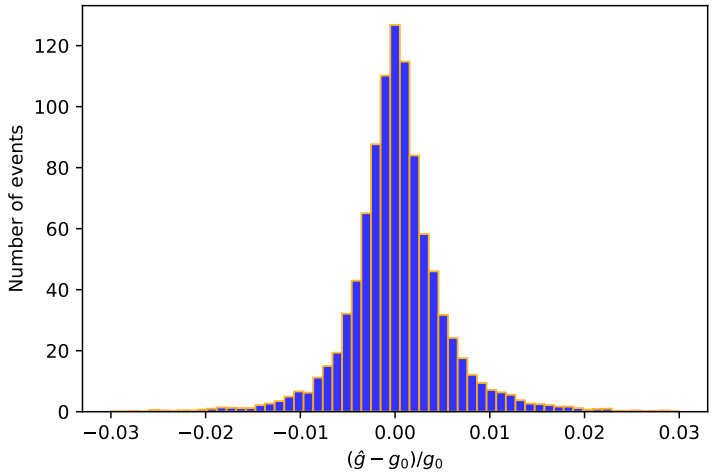

Figure I.39: Normalised histogram of 10000 estimators $\hat{g}$ obtained with quantum reflection.

the constraints on the choice of photodetachment parameters, as they allow an increase of δE which is certainly good for discussion of the photodetachment efficiency.

We have considered a clean geometry with two disks symmetrically positioned above and below the source to hide the obstacles. The accuracy is improved thanks to the additional information on the value of g gained from the presence of shadow edges, the positions of which depend on g.

We summarize below the relative uncertainty and proportion of atoms detected for the different designs considered in this chapter, for $f = 1$ MHz, $\delta E = 30$ μeV and horizontal polarization of the laser.

Design	**Dispersion σ_g/g**	**N_c/N**	**Stat. efficiency**
Horizontal plane	1.62%	100%	Yes
Cylindrical chamber	2.93%	100%	No
With disks	0.36%	60%	No
With disks and QR	0.84%	66%	No

Table I.5: Relative dispersion for the designs considered in this chapter.

For a precise analysis and good discussion of the results, we also need to discuss systematic effects and to take into account the uncertainty of design parameters: initial time t_0, detection position Z, position of the disks,...

Discussion of the uncertainty on the design parameters As mentioned previously in this chapter, there is an uncertainty on the initial time (time of the photodetachment), that we described by a logistic distribution δ_τ with width 500 μs. This uncertainty leads to a smoothing of the current and a small degradation of the relative uncertainty compared to the simplified case:

$$\sigma_g/g \approx 0.58\%. \tag{I.109}$$

Moreover, the detection in space isn't perfectly precise either. We implemented the probability distribution

$$p(z) = \frac{1}{\pi\Delta z \left(1 + \frac{z}{\Delta z}\right)^2}. \tag{I.110}$$

where $\Delta z \approx 0.63$ mm corresponds to the spatial resolution of the hits on the Micromegas; its value was obtained by Philipp Blumer at ETH Zurich by simulating the signal obtained in Micromegas. By taking into account this resolution, the relative uncertainty on g of the experiment obtained with our simulation is:

$$\sigma_g/g \approx 0.62\%. \tag{I.111}$$

The next point concerns the uncertainty on the position of the disks, i.e. the distance H_d from the trap. We implemented an uncertainty of 20 μm on the position of the disks. More precisely, in the Monte-Carlo simulation, we positioned the lower disk at the distance $H_d = 1$ cm - 20 μm from the trap and the upper disk at distance $H_d = 1$ cm + 20 μm from the trap. The analysis process is performed with values of height expected $H_d = 1$ cm. The bias and relative uncertainty obtained with this error of 20 μm is:

$$0.22\% \pm 0.38\%. \tag{I.112}$$

If the error is greater, then the bias is greater and this is not acceptable. 20 μm is then the maximal error acceptable for experimentators.

Diffraction on the borders of the disks Antihydrogen atoms exhibit wave properties and can therefore diffract. The diffraction effect consists in the bending of the wave around the corners of an obstacle or through an aperture. To estimate the importance of this effect, we calculate first the approximate De Broglie wavelength of antihydrogen atoms in our experiment:

$$\lambda_{dB} = \frac{h}{mv} \sim 1\ \mu m. \tag{I.113}$$

As this De Broglie wavelength is smaller than the acceptable uncertainty on the position of the disks (20 μm), we can deduce that the diffraction effect can be neglected.

The table I.6 sums up the bias and relative dispersion obtained with the cylindrical design with disks, by taking into account the uncertainties inherent to the experiment. With the parameters chosen, the relative dispersion remains below 1% and the bias is lower than the dispersion.

Case considered	**Bias ± dispersion σ_g/g**
Reference case (without uncertainties)	-0.001% ± 0.36%
With quantum reflection	0.002% ± 0.84%
Uncertainty on initial time t_0 (τ = 500 μs)	0.014% ± 0.58%
Uncertainty on detection position z (Δz = 0.63 mm)	-0.01% ± 0.62%
Uncertainty of 20 μm on the position of the disks	0.22% ± 0.38%

Table I.6: Bias and relative dispersion with the different sources of uncertainty, for the design with cylindrical shape and disks.

This work opens the way to a more realistic description of the experiment, which should take into account details which have not been treated here, such as the reconstruction of annihilation events from the detection of secondary particles [107].

Evolution of the free fall chamber Our simulations have led to an evolution of the design of the free fall chamber of the GBAR experiment in order to get the best precision possible. In particular, we stressed the need to implement two disks of radius 2 cm positioned 1 cm from the trap in order to hide the complexity of the trap; with horizontal polarization of the laser in order to launch the atoms preferably in the free interval between the two disks. We also highlighted the need to have a very good polishing of detection surfaces to prevent diffuse quantum reflection. Finally, we pointed out the fact that the increase of the radius of the chamber induces a better accuracy as it maximizes the time of flight, as illustrated in the table I.7.

Radius of the chamber	R_c = 25 cm	R_c = 35 cm	R_c = 50 cm
Relative uncertainty	0.36%	0.28%	0.23%

Table I.7: Relative dispersion for the design with disks by changing the radius of the chamber.

Based on these inputs coming from our analysis, a new design of the free fall chamber has been proposed and accepted by the collaboration GBAR. It has an hexagonal shape, with length of 1 m and width 50 cm (see figure I.40). This hexagonal form ensures mechanical stability, and the flat sides maximize pion detection efficiency with micromegas [119]. All the conclusions highlighted in this chapter also applies for this hexagonal shape. We stress that all the detailed analysis will be performed at ETH Zürich.

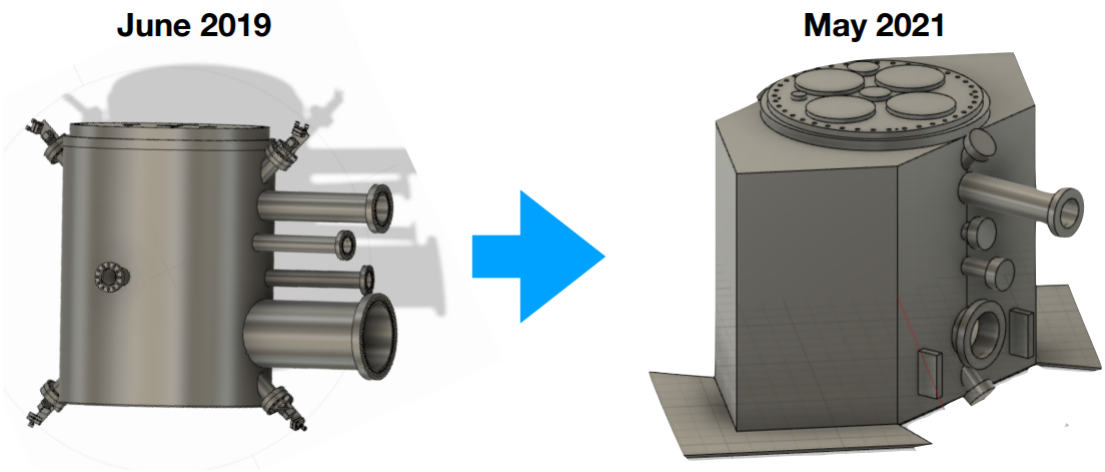

Figure I.40: Evolution of the GBAR free fall chamber from cylindrical shape to hexagonal shape [119].

Chapter II

Quantum interference measurement of the free fall of antihydrogen

In this part, we study a quantum interference experiment which was proposed [120] with the aim to improve drastically the accuracy of the GBAR measurement with respect to the classical timing measurement. The main idea is to use quantum techniques similar to those used on *Gravitational Quantum States* (GQS) of ultra-cold neutrons [19, 20, 21, 22]. Ultracold neutrons bounce above a matter surface due to the repulsive Fermi interaction [121, 122, 123, 124]. For atoms, quantum bounces may be produced by the rapidly varying attractive van der Waals/Casimir-Polder interaction above the surface [5, 7, 8, 9, 10, 11, 12, 125, 126, 127, 128, 129, 130]. This quantum reflection mechanism is expected to work with antihydrogen atoms, thus preventing their annihilation at the matter surface [13, 14, 23, 131].

The GBAR quantum design was proposed and studied in [120] without accounting for the photodetachment recoil, and it led to an uncertainty of about $8 \cdot 10^{-6}$; the overall movement over the quantum mirror was produced by an initial kick v_0 along a horizontal direction. Here, the photodetachment recoil $v_e \simeq 1\,\mathrm{m/s}$ is enough to produce the overall movement so that we don't need to consider an initial kick. For simplicity, we will even neglect the kick produced by the photon absorption ($v_\gamma = 0.24\,\mathrm{m/s}$) which is small with respect to v_e. One could be afraid of a degradation of the accuracy due to photodetachment, and the purpose of this chapter is to evaluate this effect.

II.1 GBAR Quantum design

The current design of the GBAR experiment is classical but it is also known that free fall acceleration can be measured by quantum interferometry [30, 38, 132, 133]. We propose to improve the accuracy of the GBAR free fall measurement by using the existence of GQS already proven by experiments performed on ultracold neutrons [19]. This new method assumes simultaneous measurement of many Gravitational Quantum States, thus enormously increasing statistics compared to previous proposals [134, 135] which considered one or a few quantum states. A practical implementation of this method is in

principle simple, since it does not need precision optics and mechanics and doesn't need the selection of a single quantum state.

The quantum design has been chosen to add minimal modifications to the GBAR classical free fall design [70]. A circular quantum reflecting mirror of diameter $d = 5\,\text{cm}$ is added at distance $h = 10\ \mu\text{m}$ below the center of the ion trap (see in figure II.1 the 2D view of the quantum design). The experimental setup is then decomposed into two zones: the interference zone, made of a mirror on which Gravitational Quantum States interfere; and the free fall zone with height $H = 30$ cm, that transforms the interference pattern at the end of the mirror to an interference pattern on the detector [120].

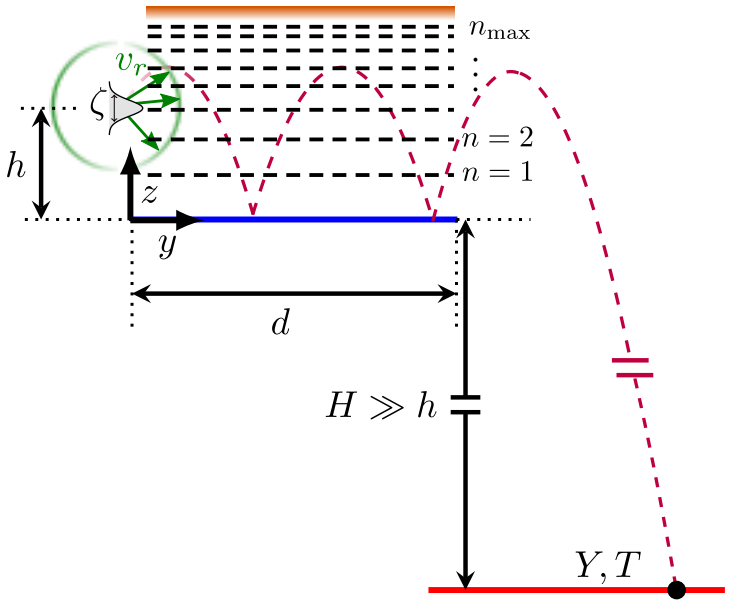

Figure II.1: 2D schematic representation of the quantum design. The quantum mirror of length d is the blue horizontal line. The wave packet has a mean height h above the mirror and a dispersion ζ in all space directions. An absorber (orange line) is placed above the surface allowing $n_{\max}$ Gravitational Quantum States to pass through the device. H is the free fall height, Y and T are the positions in space and time of the detection events in the detector plate in red.

In figure II.1, lowercase letters represent quantities relative to first stages of preparation and interference above the mirror, while uppercase letters represent quantities associated with free fall and detection stages. The parabolas in purple represent a classical motion with rebounds above the mirror while the horizontal dashed lines represent the paths through different quantum states which interfere in the detection pattern. This 2D figure is drawn in the y, z-plane (that is also $\Phi = \frac{\pi}{2}$ as azimuth angle). In the following, we will also account for velocities corresponding to other values of Φ in this 3D distribution.

The quantum mirror in the plane $z = 0$ produces bounces which constrain the atomic

wave packet to remain in the half space $z > 0$ until it reaches the end of the mirror. Atoms with a low vertical velocity above the surface are trapped by the combined action of quantum reflection and gravity [136, 137]. They bounce several times above the mirror (quantum reflection on Casimir-Polder potential, see appendix B for details), and the quantum paths corresponding to different GQS interfere [120]. Atoms having a larger vertical velocity are absorbed by a rough plate placed at some height above the quantum reflecting mirror [122]. Precisely, the absorber selects states with $n < n_{\max}$ such that the wave function can pass through the slit [72, 124]. This important point will be taken into account in the following by restricting the number of GQS to this range $n < n_{\max}$, which of course limits the number of atoms useful for the measurement.

After the end of the mirror, the atomic wave packet evolves through a free fall down to its annihilation on the detection plate. We expect that the quantum interference pattern on the detector contains much more information than the classical one.

In the following parts, we will study the evolution of the antihydrogen wave packet, with its initial distribution accounting for photodetachment process, its evolution in the GQS region, and its free fall to the detection plate. We will analyze the interference pattern at detection appearing as a consequence of interference between the different GQS. We present the estimation of the uncertainty obtained with numerical and analytical statistical methods, and compare the results to those of the classical analysis [108] as well as those of the quantum analysis presented in [120] without photodetachment recoil.

II.2 Description of the initial state

The equations presented in this part describing the initial state are the same as the ones in the classical design (chapter I).

Before photodetachment We take the same model as before for the initial distribution in the trap, i.e. a gaussian wave packet. We repeat some calculations with notations changed to meet our needs for the quantum design analysis.

Antihydrogen atoms of mass m are released from the trap at height $h = 10$ μm above the reflecting mirror chosen as the origin of altitudes. The ground state of the ion trap is represented by a wave-packet centered at $\boldsymbol{r}_h = (0, 0, h)$ with a Gaussian shape

$$\Psi_{\text{trap}}(\boldsymbol{r}_{\text{trap}}) = \left(\frac{1}{2\pi\zeta^2}\right)^{3/4} \exp\left(-\frac{(\boldsymbol{r}_{\text{trap}} - \boldsymbol{r}_h)^2}{4\zeta^2}\right) , \tag{II.1}$$

with $\boldsymbol{r}_{trap}$ the position, $\zeta = \Delta x = \Delta y = \Delta z = \sqrt{\frac{\hbar}{2m\omega}}$ the position dispersion of the initial wave packet which is determined by $\omega = 2\pi f$ with f the trap frequency. In our simulations, we use trap frequency of $f = 20$ kHz, which corresponds to position dispersion $\zeta = 0.5$ μm and velocity dispersion $\Delta v = \hbar/(2m\zeta) = 6.3$ cm/s.

In momentum representation, the wave function is read as

$$\widetilde{\Psi}_{\text{trap}}(\boldsymbol{p}_{\text{trap}}) = \left(\frac{1}{2\pi\Delta p^2}\right)^{3/4} \exp\left(-\frac{\boldsymbol{p}_{\text{trap}}^2}{4\Delta p^2} - \frac{i}{\hbar}\boldsymbol{p}_{\text{trap}} \cdot \boldsymbol{r}_h\right) . \tag{II.2}$$

Those distributions are normalized:

$$\int d^3\boldsymbol{r}_{\rm trap}|\Psi_{\rm trap}(\boldsymbol{r}_{\rm trap})|^2 = \int \frac{d^3\boldsymbol{p}_{\rm trap}}{(2\pi\hbar)^3}|\widetilde{\Psi}_{\rm trap}(\boldsymbol{p}_{\rm trap})|^2 = 1. \tag{II.3}$$

Photodetachment process We note $\boldsymbol{q}_e$ the momentum transferred to the atom in the photodetachment process (due excess e^+ recoil) with its fixed magnitude

$$|q_e| = \sqrt{2m\delta E} \tag{II.4}$$

and its expression in spherical coordinates

$$\boldsymbol{q}_e = q_e\hat{q}_e = q_e\ (\sin\theta_e\cos\varphi_e, \sin\theta_e\sin\varphi_e, \cos\theta_e). \tag{II.5}$$

In the following, we will take an excess energy above the threshold $\delta E = 10\ \mu$eV which corresponds to a recoil velocity $v_e = |q_e|/m \simeq 1$ m/s.

After the photodetachment, the momentum of the atom is given by the sum of the momentum $\boldsymbol{p}_{\rm trap}$ inside the trap and the recoil momentum $\boldsymbol{q}_e$ transferred in the photodetachment process

$$\boldsymbol{p}_0 = \boldsymbol{p}_{\rm trap} - \boldsymbol{q}_e. \tag{II.6}$$

In order to describe the angular distribution of recoil, we assume that the laser momentum is along the horizontal $x-$direction and the laser polarization along the horizontal $y-$direction. While the former assumption is just a convenient choice for installing the laser in the free fall chamber, the latter assumption is mandatory for maximizing the proportion of atoms going out of the slit (formed by the quantum mirror and the rough absorber) with a nearly horizontal velocity. With this choice (fixed throughout this chapter), the recoil velocities obey a dipolar distribution centered around the polarization direction y (with Ω the solid angle)

$$\varpi(\hat{q_e})d\Omega = \frac{3}{4\pi}(\hat{q_e}\cdot\hat{y})^2 d\Omega = \frac{3}{4\pi}(\sin\theta_e\sin\varphi_e)^2\sin\theta_e d\theta_e d\varphi_e. \tag{II.7}$$

In the current GBAR design, the photodetached positron is not detected and the initial state of $\bar{H}$ atoms has to be described by a density matrix corresponding to a statistical mixture with different recoil directions:

$$\hat{\rho}_0 = \int |\Psi_{q_e}\rangle\langle\Psi_{q_e}|\,\varpi(\hat{q}_e)d\Omega\ , \tag{II.8}$$

$$\Psi_{q_e}(\boldsymbol{r}_0) = \left(\frac{1}{2\pi\zeta^2}\right)^{3/4}\exp\left(-\frac{(\boldsymbol{r}_0-\boldsymbol{r}_h)^2}{4\zeta^2} + \frac{i}{\hbar}\boldsymbol{q_e}\cdot(\boldsymbol{r}_0-\boldsymbol{r}_h)\right). \tag{II.9}$$

The distribution ϖ of the different recoil directions appears in the density matrix to describe the incoherent sum over the undetected photodetached positrons. This incoherent part of the preparation of the $\bar{H}$ atoms could blur the interference pattern predicted without photodetachment [120] and then lead to a degradation of the accuracy expected

for the quantum measurement. The goal of the present chapter is precisely to evaluate how the photodetachment recoil affects the quantum interference fringes and the accuracy expected for the quantum measurement.

The distribution of momenta $\boldsymbol{p}_0$ after the photodetachment then results from a convolution of the Gaussian distribution in the trap and the distribution of photodetachment recoil (details in chapter I). From now on, we use velocity $\boldsymbol{v}_0 = \dfrac{\boldsymbol{p}_0}{m}$ instead of momentum as the mass of the atom is not relevant for free fall. The velocity distribution $\Pi(\boldsymbol{v}_0)$ is shown as density plot in figure II.2 for $f = 20$ kHz, $\delta E = 10$ μeV and horizontal polarization of the laser. The recoil velocity associated to detached positron lies on a sphere with radius $v_e = 1.02$ m/s (with dipolar distribution aligned on the polarization direction y), with the width of the shell $\Delta v = 6.3$ cm/s smaller than the radius v_e.

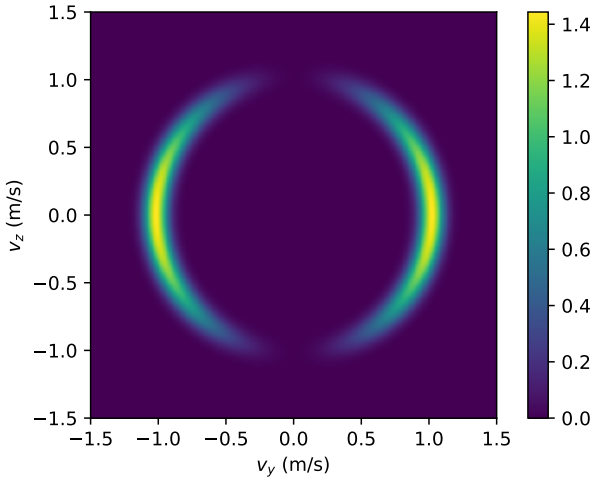

Figure II.2: Density plot of the velocity distribution in the (v_y, v_z) plane for $\delta E = 10$ μeV (corresponding to $v_\mathrm{e} = 1.02$ m/s) and $f = 20$ kHz (corresponding to $\Delta v = 6.3$ cm/s).

II.3 Interferences above the mirror

Once the excess positron is photodetached, the antiatom is released from the trap and can evolve above the reflecting mirror.

We suppose that most atoms survive their flight above the reflecting surface, due to nearly perfect quantum reflection for atoms having a small orthogonal velocity above the reflecting surface (see appendix B for details of quantum reflection). The wave packet obeying the Schrödinger equation remains factorized:

$$\Psi_t(x, y, z) = \phi_t(x, y)\ \psi_t(z). \tag{II.10}$$

with t the time spent above the reflecting mirror. This condition of separability of the Hamiltonian in x and z coordinates imposes constraints on the quality of the mirror surface roughness and material homogeneity. The free horizontal evolution leads to a mere spreading of the wave packet $\phi_t(x, y)$.

II.3.1 Vertical evolution above the reflecting mirror

We consider that, in our conditions of experiment, the quantum reflection probability of hydrogen and antihydrogen above reflecting mirror is 1 (perfect reflection) at the vertical velocities relevant for the experiment

$$r = -1 \;\rightarrow\; |r|^2 = 1. \tag{II.11}$$

In the approximation of a perfectly reflecting mirror, the particle is reflected by an abrupt step. We now want to solve the stationary Schrodinger equation:

$$\begin{aligned} \left[-\frac{\hbar^2}{2m}\frac{d^2}{dz^2} + mgz\right]\psi(z) &= E\;\psi(z) \quad , \quad z > 0 \\ \psi(z) &= 0 \quad , \quad z < 0. \end{aligned} \tag{II.12}$$

For that we introduce the following change of variables:

$$x \equiv \frac{z}{l_g} - \frac{E}{\epsilon_g}\ , \tag{II.13}$$

with

$$l_g \equiv \left(\frac{\hbar^2}{2m^2 g}\right)^{1/3} \approx 5.87\ \mu m \quad , \quad \epsilon_g \equiv mgl_g = \left(\frac{\hbar^2 m g^2}{2}\right)^{1/3} \approx 0.6\ \text{peV}. \tag{II.14}$$

l_g and ϵ_g are the typical scales in length and energy associated with quantum effect in the Earth gravity field. In addition, we deduce the associated typical scales for time and velocity:

$$v_g = \frac{\hbar}{ml_g} = \left(\frac{2\hbar g}{m}\right)^{1/3} \approx 1.07\ cm/s \quad , \quad t_g = \frac{\hbar}{\epsilon_g} = \left(\frac{2\hbar}{mg^2}\right)^{1/3} \approx 1.09\ ms. \tag{II.15}$$

With a radius of 5 cm for the mirror, the time spent above the mirror is approximately 50 ms, typically a large number of bounces as the time scale for bounces is of the order of 1 ms.

The Schrodinger stationary equation becomes, with ψ here replaced by χ:

$$\chi''(x) - x\;\chi(x) = 0. \tag{II.16}$$

The general solution of this equation is given by a linear combination of independent solutions of the Airy functions Ai and Bi [111, 112, 138, 139]:

$$\chi(x) = a\ \text{Ai}(x) + a\ \text{Bi}(x). \tag{II.17}$$

with a, b constants. In terms of our initial variables, this expression becomes

$$\chi(z) = a\ \mathrm{Ai}\left(\frac{z}{l_g} - \frac{E}{\epsilon_g}\right) + b\ \mathrm{Bi}\left(\frac{z}{l_g} - \frac{E}{\epsilon_g}\right). \tag{II.18}$$

The Airy function was introduced by Airy in 1838 to describe optical caustics such as rainbows [140, 141]. More generally, the Airy function is the solution to the time-independent Schrödinger equation for a particle confined within a triangular potential well (gravity potential in our case). The Airy function is illustrated in figure II.3, it has a countable infinity of zeros, written as $(-\lambda_n)$. More properties of the Airy functions can be found in the NIST Handbook of Mathematical Functions [111] or in the book by Vallée and Soares [139].

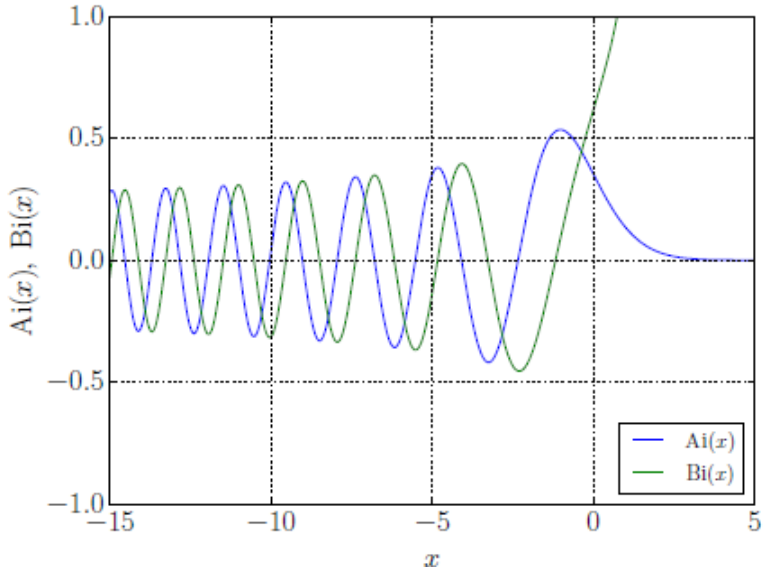

Figure II.3: Graphical representation of the Airy functions Ai and Bi.

With the requirement that the wave function vanishes as $z \to +\infty$ and as the function Bi diverges for $z \to +\infty$, then we have to set $b = 0$ in the expression of the wave function [18, 22]:

$$\chi(z) = a\ \mathrm{Ai}\left(\frac{z}{l_g} - \frac{E}{\epsilon_g}\right). \tag{II.19}$$

The abrupt step in $z = 0$ enforces the boundary condition $\psi(0) = 0$, which gives the energy levels E_n of the ideal quantum bouncer in terms of the zeros $(-\lambda_n)$ of the Airy function [22]:

$$E_n = \lambda_n \epsilon_g \quad , \quad \mathrm{Ai}(-\lambda_n) = 0 \quad , \quad n = 0, 1, 2, ... \tag{II.20}$$

There exist many solutions for equation $\mathrm{Ai}(-\lambda_n) = 0$ and they are best found via nu-

merical modules in `Python`. The coefficients a_n can be calculated from the condition

$$\int_0^{+\infty} |a_n \ \mathrm{Ai}(z/l_g - \lambda_n)|^2 dz = 1 \tag{II.21}$$

$$\longrightarrow a_n = \left(\int_0^{+\infty} |\mathrm{Ai}(z/l_g - \lambda_n)|^2 dz\right)^{-1/2} = \frac{1}{\sqrt{l_g}\mathrm{Ai}'(-\lambda_n)}. \tag{II.22}$$

The wave functions of the gravitationally bound states are then:

$$\chi_n(z) = \Theta(z)\frac{\mathrm{Ai}(z/l_g - \lambda_n)}{\sqrt{l_g}\mathrm{Ai}'(-\lambda_n)}. \tag{II.23}$$

with Θ the Heavisde step function expressing perfect quantum reflection. The wave functions of the first states ($n = 0$ to $n = 9$) are plotted in figure II.4. From the graphs of each wave function it can be deduced that there is a non-zero probability of finding a particle outside of the described triangular potential because the graphs do not flatten entirely after crossing the line representing the potential. This means that some particles may experience tunnelling and escape the potential.

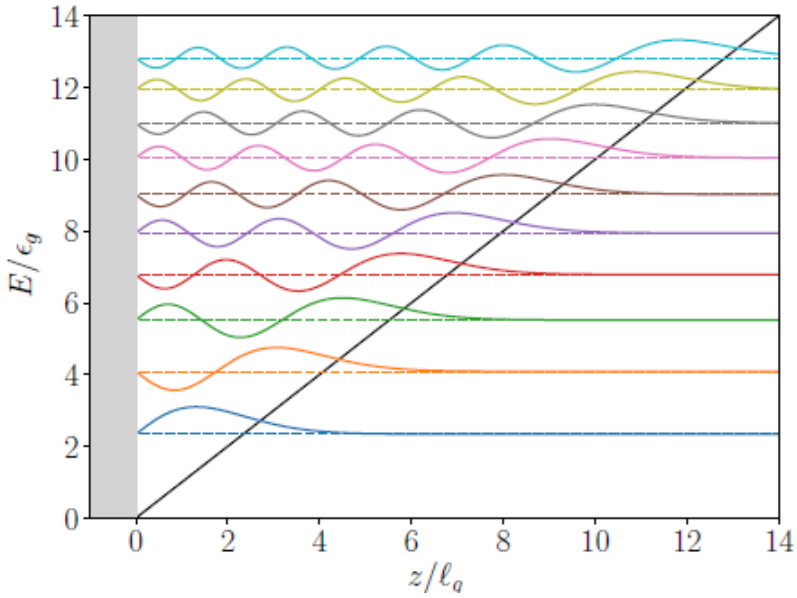

Figure II.4: Wave functions χ_n of the first 10 gravitational bound states [14]. The black line corresponds to the linear potential mgz.

For detection purposes, it is useful to convert each E_n to its corresponding height h_n above the mirror surface. These heights are readily obtained by setting E_n and $V_{g,n} = mgh_n$ equal and subsequently rearranging:

$$h_n = \frac{E_n}{mg}. \tag{II.24}$$

Table II.1 summarises the values of both E_n and h_n found for antihydrogen atoms. The h_n computed show that it is feasible to build an experiment for the detection of antihydrogen GQS. Constructing a mirror-absorber region of several micrometers height difference is not only possible, but can be done with enough accuracy to measure variations of height at a level better than l_g. This is one of the aims of the international collaboration GRASIAN (*GRAvity, Spectroscopy and Interferometry with ultra-cold Atoms and Neutrons*), which pursues research with the lightest neutral particles/atoms at lowest kinetic energies [142].

n	λ_n	E_n (peV)	h_n (μm)
1	2.338	1.407	13.72
2	4.088	2.461	24.00
3	5.521	3.324	32.42
4	6.787	4.086	39.85

Table II.1: Values of the zeros λ_n of the Airy function, GQS energy levels $E_n = \lambda_n \epsilon_g$ and corresponding heights above the mirror surface h_n for hydrogen/antihydrogen atoms.

The vertical evolution is strongly affected above the quantum bouncer and it is therefore convenient to decompose the wave packet along z on the orthonormal basis of Airy functions $|\chi_n\rangle$ [139]:

$$|\psi_{q_z,t}\rangle = \sum_n c_n(q_z)\,|\chi_n\rangle\, e^{-i\varphi_n(t)} \tag{II.25}$$

where the phase shift has a simple expression in this representation:

$$\varphi_n(t) = \lambda_n t/t_g. \tag{II.26}$$

The Airy function is already implemented in `Python`, it can be used with the function `scipy.special.airy`. The zeros of the Airy function are obtained by using the function `scipy.special.aizeros`. See appendix C for details of the code.

The amplitudes c_n in (II.25) depend on the vertical component q_z of the recoil momentum and can be calculated as overlap integrals:

$$\begin{aligned} c_n(q_z) &= \langle\chi_n|\psi_{q_z}\rangle = \int_{-\infty}^{+\infty} \psi_{q_z}(z)\chi_n(z)^* dz \\ &= \int_0^{+\infty} \left(\frac{1}{2\pi\zeta^2}\right)^{1/4} \exp\left(-\frac{(z-h)^2}{4\zeta^2} + \frac{i}{\hbar} q_z (z-h)\right) \chi_n(z)^* dz. \end{aligned} \tag{II.27}$$

When the vertical dispersion ζ is sufficiently small with respect to h, the lower bound in the integral (II.27) can be changed to $-\infty$ and the coefficients c_n have an analytical

expression:

$$\begin{aligned} c_n(q_z) &\approx \frac{\left(\frac{1}{2\pi\zeta^2}\right)^{1/4}}{\sqrt{l_g}Ai'(-\lambda_n)} \int_{-\infty}^{+\infty} \exp\left(-\frac{(z-h)^2}{4\zeta^2} + \frac{i}{\hbar}q_z(z-h)\right) Ai(z/l_g - \lambda_n)dz \\ &= \frac{\left(\frac{1}{2\pi\zeta^2}\right)^{1/4}}{\sqrt{l_g}Ai'(-\lambda_n)} \exp\left(-\frac{q_z^2\zeta^2}{\hbar^2}\right) \int_{-\infty}^{+\infty} \exp\left(-\left(\frac{z-h'}{2\zeta}\right)^2\right) Ai(z/l_g - \lambda_n)dz \end{aligned}$$

by noting $h' \equiv h + \frac{2iq_z\zeta^2}{\hbar}$. With the change of variables $x = \frac{z-h'}{2\zeta} \Leftrightarrow z = 2\zeta x + h'$, we get:

$$\begin{aligned} c_n(q_z) &= \frac{\left(\frac{1}{2\pi\zeta^2}\right)^{1/4}}{\sqrt{l_g}\mathrm{Ai}'(-\lambda_n)} \exp\left(-\frac{q_z^2\zeta^2}{\hbar^2}\right) \int_{-\infty}^{+\infty} \exp(-x^2)\mathrm{Ai}\left(2\frac{\zeta}{l_g}x + \frac{h'}{l_g} - \lambda_n\right) 2\zeta dx \\ &= \frac{(8\pi\zeta^2)^{1/4}}{\sqrt{l_g}Ai'(-\lambda_n)}\mathrm{Ai}\left(\frac{h'}{l_g} - \lambda_n + \frac{\zeta^4}{{l_g}^4}\right) \exp\left(\frac{\zeta^2}{{l_g}^2}\left(\frac{h'}{l_g} - \lambda_n + \frac{2}{3}\frac{\zeta^4}{{l_g}^4}\right) - \left(\frac{q_z\zeta}{\hbar}\right)^2\right) \end{aligned}$$

where at the last step we used the formula [14]

$$\int_{-\infty}^{+\infty} \exp(-x^2) Ai(2ax + b)dx = \sqrt{\pi}\exp\left(a^2b + \frac{2a^6}{3}\right) Ai(b + a^4) \qquad \text{(II.28)}$$

$$a = \frac{\zeta}{l_g} \quad , \quad b = \frac{h'}{l_g} - \lambda_n.$$

We checked that this expression leads to the same result as the numerical computation (performed with `scipy.integrate.simps`) for the range of parameters considered in this study. We represent in figure II.5 the plots of the coefficient c_n (real and imaginary parts), where we see a very good agreement between the analytical expression and the numerical-integral expression.

In the particular case $q_z = 0$, then $h' = h$, and we get:

$$c_n = \frac{(8\pi\zeta^2)^{1/4}}{\sqrt{l_g}Ai'(-\lambda_n)}\mathrm{Ai}\left(\frac{h}{l_g} - \lambda_n + \frac{\zeta^4}{{l_g}^4}\right) \exp\left(\frac{\zeta^2}{{l_g}^2}\left(\frac{h}{l_g} - \lambda_n + \frac{2}{3}\frac{\zeta^4}{{l_g}^4}\right)\right). \qquad \text{(II.29)}$$

which corresponds to the formula obtained in [120] without taking into account the photodetachment process.

The relevant quantity after the interference zone is the squared wave function in the momentum representation, which we compute in the next part.

II.3.2 Momentum distribution above the mirror

In this part, we compute the momentum distribution in order to see the shape of the signal at the end of the interference zone. We express the density matrix after a time t spent above the quantum mirror:

$$\rho_t(\boldsymbol{r}, \boldsymbol{r'}) = \int \Psi_{q_e,t}(\boldsymbol{r})\Psi^*_{q_e,t}(\boldsymbol{r'})\ \varpi(\hat{q}_e)d\Omega. \qquad \text{(II.30)}$$

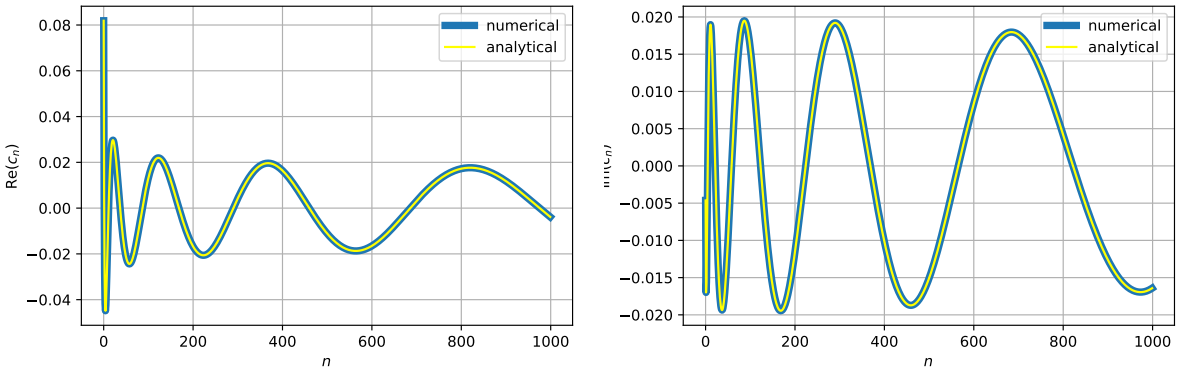

Figure II.5: Plot of the coefficient c_n as function of n for $q_z = q_e/5 \approx 19\ p_g$ - comparison between the analytical and numerical computations. Left: real part of c_n; right: imaginary part of c_n.

For the purpose of treating the free fall in the next section, the density matrix will be conveniently represented by the following Wigner distribution:

$$W_t(\boldsymbol{r},\boldsymbol{p}) = \frac{1}{(2\pi\hbar)^3}\int_{\mathbb{R}^3} \exp\left(-\frac{i}{\hbar}\boldsymbol{p}\cdot\boldsymbol{s}\right)\rho_t\left(\boldsymbol{r}+\frac{\boldsymbol{s}}{2},\boldsymbol{r}-\frac{\boldsymbol{s}}{2}\right)d^3\boldsymbol{s}. \tag{II.31}$$

We then calculate the relevant signal as the probability in momentum space at the end of the mirror, it is defined as the marginal of the Wigner function integrated over position:

$$\begin{aligned}\Pi_t(\boldsymbol{p}) &= \int_{\mathbb{R}^3} W_t(\boldsymbol{r},\boldsymbol{p})d^3\boldsymbol{r}\\ &= \int d\Omega\ \varpi(\hat{q}_e)\ \left|\widetilde{\phi}_{q_{xy},t}(p_x,p_y)\right|^2\ \left|\widetilde{\psi}_{q_z,t}(p_z)\right|^2\\ &= \int d\Omega\ \varpi(\hat{q}_e)\frac{1}{2\pi\Delta p^2}e^{-\frac{(p_x-q_x)^2+(p_y-q_y)^2}{2\Delta p^2}}\left|\sum_n c_n(q_z)\widetilde{\chi}_n(p_z)e^{-i\varphi_n(t)}\right|^2\end{aligned} \tag{II.32}$$

where we have introduced the Fourier transforms $\widetilde{\chi}_n$ of the eigenfunction χ_n

$$\widetilde{\chi}_n(p_z) = \frac{1}{\sqrt{2\pi\hbar}}\int_{-\infty}^{+\infty} e^{-\frac{ip_z z}{\hbar}}\chi_n(z)dz. \tag{II.33}$$

These Fourier transforms are the sources of the interference pattern, as discussed in [120]. They are computed numerically by using the module `numpy.fft.fft()`. The functions $\widetilde{\chi}_n(p_z)$ are represented in figure II.6 for the first values of n. They contribute as oscillations with time frequency λ_n/t_g. The number of peaks of the real and imaginary parts of the function $\widetilde{\chi}_n(p_z)$ increase when n increases.

As highlighted in equation (II.32), the signal is composed of two sums: a coherent sum over the n Gravitational Quantum States which produces interference fringes; and

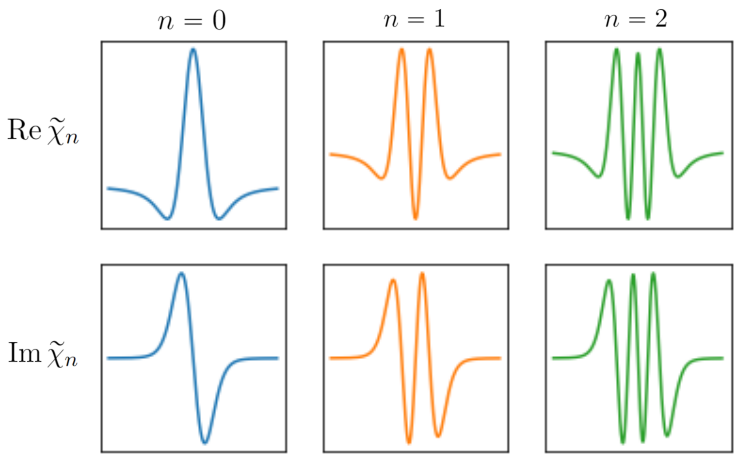

Figure II.6: Illustration of $\widetilde{\chi}_n(p_z)$ for $0 \leqslant n \leqslant 2$ with their real part (1^{st} line) and their imaginary part (2^{nd} line).

an incoherent sum over photodetachment recoil which introduces noise on the figure and could blur the interference pattern. The goal of our simulations is to evaluate the extent to which the incoherent part may degrade the interference fringes with respect to the case without photodetachment studied in [120].

In (II.32), the double integral over photodetachment angles θ_e and φ_e is performed numerically, where θ_e varies from 0 to π and φ_e varies from 0 to 2π. Moreover, the sum over the Gravitational Quantum States n is accelerated by using the compiler `Numba` (see appendix C for details).

The probability density in velocity space at the end of the mirror $\Pi_t(\boldsymbol{v})$ is drawn in figure II.7 as function of v_z and t, by fixing $v_x = 0$ and $v_y = v_e$. In this figure, bright oblique lines can be seen, corresponding to constructive interferences. They are aligned along classical motions, with velocity linearly decreasing from a high positive value to the opposite negative value, before abruptly changing sign at the bounce on the mirror. The timing bounds have been chosen to correspond to the time spent above the mirror by the fastest and slowest antiatoms respectively. The brightest fringes are analogous to classical trajectories. Indeed, when time passes, we see that the impulsion is alternatively positive and negative; this corresponds to a situation of a classical object bouncing on a surface. Let us emphasize however that our calculation is fully quantum.

The figure II.8 illustrates the fine details of the pattern obtained at the end of the mirror. The pattern is quite complex, with small oscillations and high peaks, but it clearly reveals interference fringes. These fringes are encoded in the velocity or momentum distribution at the end of the mirror, due to interference between the paths corresponding to the different GQS above the quantum mirror. The pattern contains many fringes with details of their variation highlighted in the zoom shown in the inset for a narrow range. This is the first confirmation that the interference pattern isn't degraded significantly by the photodetachment process.

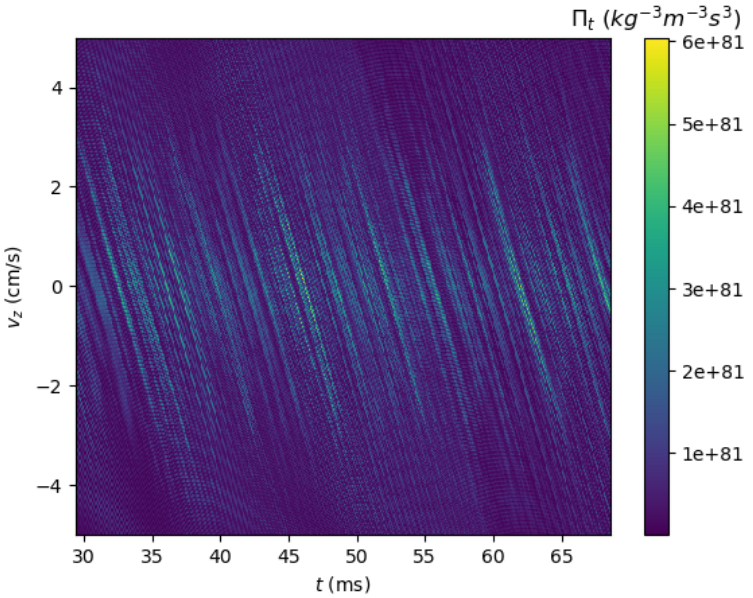

Figure II.7: Probability density in velocity space $\Pi_t(v_z)$ - 2D plot. Parameters: $f = 20$ kHz, $\delta E = 10$ μeV, $n_{\max} = 1000$.

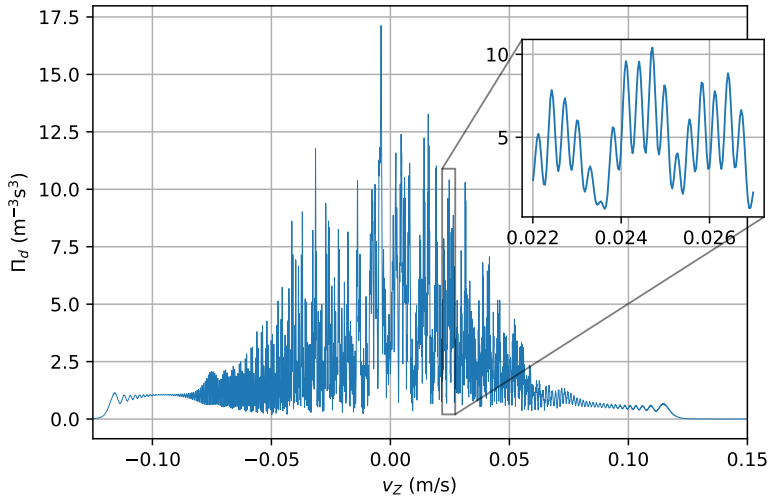

Figure II.8: 1D plot of figure II.7 by fixing $t = d/v_e \approx 49$ ms.

We suppose that the wave function matches at the virtual surface separating the GQS zone and the free fall zone. This matching corresponds to the continuity of the wave function (and its derivative) at the surface $x = d$ with:

$$\begin{aligned} \Psi(d^-, z) &= \Psi(d^+, z) \ , \\ \frac{\partial \Psi}{\partial x}(d^-, z) &= \frac{\partial \Psi}{\partial x}(d^+, z). \end{aligned} \tag{II.34}$$

This treatment neglects horizontal quantum reflection induced by the change of the potential landscape at $x = d$. The same approximation used in the theoretical description of neutron whispering gallery modes leads to a satisfactory agreement with experiments [135].

After the mirror, the antiatom evolves though a free fall. This free fall will be modelled by using Wigner formalism as was done in chapter I, and also by using the quantum propagator.

II.4 Detection annihilation events

As already explained, the free fall is intended to reveal in the pattern on the detector the interferences which were mainly encoded on momentum at the end of the quantum mirror [120]. The interference pattern produced at the end of the quantum mirror is read out after a free fall from the positions in space and time of annihilation events of $\bar{H}$ at the detector.

II.4.1 Effect of an absorber and number of atoms detected

The high-lying GQS are truncated by putting an absorber at some height $z_{\max}$ above the quantum reflecting mirror [72, 120, 122]. Only states with spatial size z_n smaller than the slit size can penetrate through the slit, and the other ones are absorbed. For example, the spatial size of the first GQS is $z_1 = 13.8$ μm and then a slit larger than 13.8 μm is enough to make it pass.

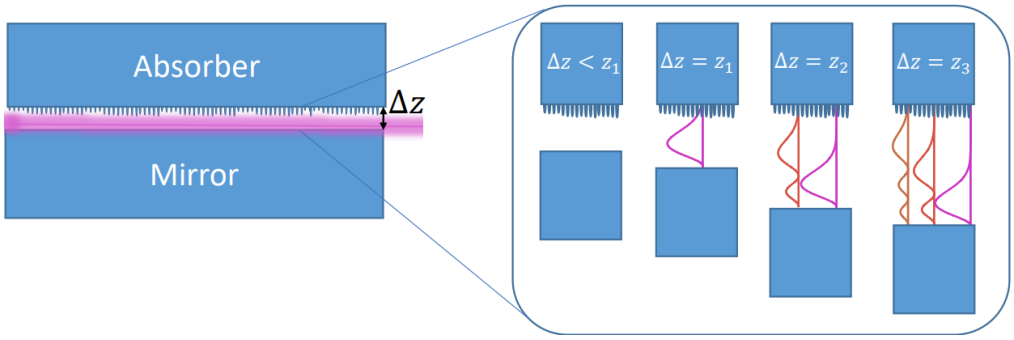

Figure II.9: Illustration of the GQS region: mirror and absorber separated by a slit of height $z_{\max}$. Only states with spatial size $z_n < z_{\max}$ can pass.

The absorber selects states with $n < n_{\max}$ such that the wave function χ_n can pass through the slit [72, 124]. This important point will be taken into account in the following

by restricting the number of GQS to the range $n \in [0, n_{\max}]$, which of course limits the number of atoms useful for the measurement.

The number of atoms detected (noted N_c) is given by the following expression:

$$N_c = N \int d\Omega \; \varpi(\hat{q_e}) \sum_n |c_n(q_z)|^2. \tag{II.35}$$

For a horizontal polarization of the laser, this expression simplifies:

$$N_c = N \; \frac{3}{4} \int_0^\pi d\theta_e \sin^3 \theta_e \sum_n |c_n(q_e \cos\theta_e)|^2. \tag{II.36}$$

This integral is performed numerically with the module `numpy.integrate.quad`. With the numbers used here ($f = 20\,\text{kHz}$, $\delta E = 10\ \mu\text{eV}$ and $n_{\max} = 1000$), we deduce that 26% of the initial atoms pass through the slit and are detected ($N_c = 260$ when $N = 1000$).

In order to determine the spatial size $z_{\max}$ for a given number $n_{\max}$ of GQS, two methods can be used. In the first one, $z_{\max}$ is obtained when the squared eigenfunction $|\chi_n(z)|^2$ (normalized such that its maximum value is 1) becomes nearly null:

$$|\chi_n(z)|^2 < 10^{-2} \quad \text{for} \quad z > z_{\max} \; . \tag{II.37}$$

Or $z_{\max}$ can be extracted from the normalized initial velocity distribution $\Pi_0(\boldsymbol{v})$, integrated from $-\sqrt{2gz_{\max}}$ to $\sqrt{2gz_{\max}}$ along the v_z component:

$$\int_{-\infty}^{+\infty} \int_{-\infty}^{+\infty} \int_{-\sqrt{2gz_{\max}}}^{+\sqrt{2gz_{\max}}} \Pi_0(\boldsymbol{v}) \; d^3\boldsymbol{v} = N_c/N \; .$$

With both methods, we get $z_{\max} \simeq 1.66$ mm for $n_{\max} = 1000$. We plot in the figure II.10 the values of $z_{\max}$ as function of $n_{\max}$ in log-log scale, and we observe that the regime is nearly linear.

For high values of $n_{\max}$, we estimate that the dependence between $z_{\max}$ and $n_{\max}$ is:

$$z_{\max} \simeq 1.66 \text{ mm} \left(\frac{n_{\max}}{1000}\right)^{2/3} . \tag{II.38}$$

It's compatible with the asymptotic properties of the Airy functions presented in [143].

II.4.2 Annihilation current density

We assume for simplicity that antiatoms are annihilated with 100% probability at the detection plate as their kinetic energy is large after a free fall height $H = 30$ cm. We note (x, y, z, t) the positions in space and time at the end of the mirror and (X, Y, Z, T) the measured observables at the detector.

With the numbers corresponding to the experiment, we can neglect the effect of initial position dispersions $\zeta_x = \zeta_y \simeq 0.5\ \mu$m with respect to the macroscopic dimensions of the whole setup. However, the situation is completely different for the dispersion Δz which has the same value but will be taken into account carefully in the following, as Δz is not

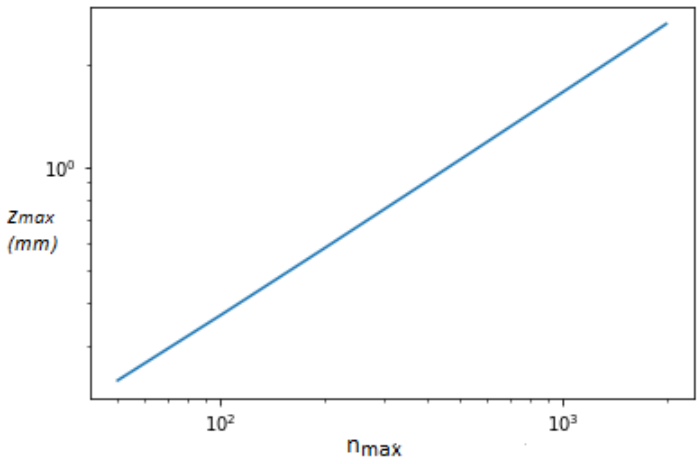

Figure II.10: Relation between $z_{\max}$ and $n_{\max}$ in log-log scale.

so small in comparison for the parameters l_g and h of interest for vertical evolution. We will also use the fact that horizontal velocities are preserved during the whole experiment to relate them to the measured observables that are the positions (X, Y, Z, T) in space and time of the annihilation event. The relations of classical mechanics between variables at the end of the mirror and the ones at the detection are presented below.

The total time of detection is the sum of the time t spent above the interference zone and the free fall time τ:

$$T = t + \tau \quad , \quad t = \frac{d}{\sqrt{X^2 + Y^2}} T \ . \tag{II.39}$$

The horizontal components of the velocity at the end of the mirror are:

$$v_x = \frac{x}{t} = \frac{X}{T} \quad , \quad v_y = \frac{y}{t} = \frac{Y}{T} \quad , \quad \sqrt{v_x^2 + v_y^2} = \frac{R}{T} \quad , \quad R = \sqrt{X^2 + Y^2} \ . \tag{II.40}$$

The vertical components of velocity at the end of the mirror and at detection are denoted v_z and V_z respectively and they can be written in terms of the observed vertical position Z and of the altitude z at the end of the mirror:

$$v_z = \frac{Z - z}{\tau} + \frac{g\tau}{2} \quad , \quad V_z = v_z - g\tau = \frac{Z - z}{\tau} - \frac{g\tau}{2} \ . \tag{II.41}$$

The observable is the particle current J, which is counted as a number of particle per unit of time and per unit of surface. As the Hamiltonian describing the free fall is at most quadratic in positions and momenta, the free fall can be described as classical in the Wigner representation. The free fall acts in a similar way as a diffraction process, with the space and time positions of the annihilation event on the detector reading the interaction time and momentum of the atom leaving the interference zone.

Approximate method By considering $z = 0$, the free fall time τ depending only on the free fall height H:

$$\tau \approx \tau_H \equiv \sqrt{\frac{2H}{g}} \tag{II.42}$$

and the approximate expression of the vertical velocity at the end of the mirror is:

$$v_z \approx \frac{Z}{\tau} + \frac{g}{2}\tau = \frac{Z}{T-t} + \frac{g}{2}(T-t). \tag{II.43}$$

Using Wigner formalism and the classical connection between the point at the end of the mirror and the one at the detection, one can write the particle current J from the marginal of Wigner function Π_t:

$$\begin{aligned} J(\boldsymbol{R},T) &= V_\perp \int_{\mathbb{R}^3} W_T(\boldsymbol{R},\boldsymbol{P}) d^3\boldsymbol{P} = \frac{m^3 V_\perp}{\tau^3} \int_{\mathbb{R}^3} W_t(\boldsymbol{r},\boldsymbol{p}) d^3\boldsymbol{r} \\ &= \frac{m^3 V_\perp}{\tau^3} \Pi_t(\boldsymbol{p}) \end{aligned} \tag{II.44}$$

with

$$V_\perp = |V_z| \quad , \quad \boldsymbol{p} = m\left(\frac{\boldsymbol{R}-\boldsymbol{r}}{\tau} - \frac{\boldsymbol{g}\tau}{2}\right) \quad , \quad \boldsymbol{g} = (0,0,-g) \tag{II.45}$$

and where the factor $\frac{m^3}{\tau^3}$ comes from the Jacobian in the corresponding change of variables. Using the expression (II.32) of the momentum distribution, one thus gets the observable detection current J.

With this simplified method, we considered that the interference information was essentially imprinted in the velocity distribution at the end of the interference zone. This has led us to neglect the fact that atoms reach a non null height at the end of this zone. This description can only be an approximation as we know that atoms reach an height up to $z_{\max} \approx 1.66$ mm for $n_{\max} = 1000$.

More precise Wigner method A safer calculation method is to use the Wigner function which is a function of z and p_z at the end of the interaction zone, and to integrate the exact free flight equations over all possible values without any restriction on the value of z.

$$\begin{aligned} J(\boldsymbol{R},T) &= \frac{m^3}{\tau^3} \int_{\mathbb{R}^3} V_\perp W_t(\boldsymbol{r},\boldsymbol{p}) d^3\boldsymbol{r} \\ &= \int d\Omega\ \varpi(\hat{q_e}) \frac{m^2}{\tau^2} \left|\widetilde{\phi}_{q_{xy},t}(p_x,p_y)\right|^2 \frac{m}{\tau} \int V_\perp w_{q_z,t}(z,p_z) dz \end{aligned} \tag{II.46}$$

with

$$\left|\widetilde{\phi}_{q_{xy},t}(p_x,p_y)\right|^2 = \frac{1}{2\pi\Delta p^2} e^{-\frac{(p_x-q_x)^2+(p_y-q_y)^2}{2\Delta p^2}} \tag{II.47}$$

the momentum distribution on horizontal axis at the end of the mirror, and the Wigner function $w_{q_z,t}(z,p_z)$ on vertical axis

$$\begin{aligned} w_{q_z,t}(z,p_z) &= \frac{1}{2\pi\hbar}\int e^{-\frac{i}{\hbar}p_z s_z}\psi_{q_z,t}\left(z+\frac{s_z}{2}\right)\psi^*_{q_z,t}\left(z-\frac{s_z}{2}\right)ds_z, \qquad \text{(II.48)} \\ & \psi_{q_z,t}(z)=\sum_n c_n(q_z)\chi_n(z)e^{-i\varphi_n(t)}. \end{aligned}$$

By integrating the Wigner function over z, we have:

$$\frac{m}{\tau}\int V_\perp w_{q_z,t}(z,p_z)dz = \frac{m}{\pi\hbar\tau}\int\int V_\perp(z)e^{-\frac{2i}{\hbar}p_z(z)s_z}\psi_{q_z,t}(z+s_z)\psi^*_{q_z,t}(z-s_z)ds_z dz$$

with

$$p_z(z)=\frac{m(Z-z)}{\tau}+\frac{mg\tau}{2} \quad , \quad V_\perp(z)=|V_z|=\left|\frac{Z-z}{\tau}-\frac{g\tau}{2}\right|>0. \qquad \text{(II.49)}$$

After several steps of calculation with changes of variables, we get:

$$\begin{aligned} \frac{m}{\tau}\int V_\perp w_{q_z,t}(z,p_z)dz &= \int\int V_\perp\left(\frac{u+v}{2}\right)f(v)f^*(u)dudv \\ &= \int\int\left(\frac{V_\perp(u)}{2}+\frac{V_\perp(v)}{2}\right)f(v)f^*(u)dudv \\ & \quad \text{with } f(x)=\sqrt{\frac{m}{2\pi i\hbar\tau}}e^{\frac{im}{2\hbar\tau}\left(Z+\frac{g\tau^2}{2}-x\right)^2}\psi_{q_z,t}(x), \\ &= \frac{1}{2}\left(\int f(v)dv\int V_\perp(u)f^*(u)du+\int V_\perp(v)f(v)dv\int f^*(u)du\right) \\ &= \mathrm{Re}\left[\int f(v)^*dv\int V_\perp(u)f(u)du\right]. \qquad \text{(II.50)} \end{aligned}$$

The final expression of the current is:

$$J(\boldsymbol{R},T)=\int d\Omega\ \varpi(\hat{q_e})\frac{1}{2\pi\Delta v^2\tau^2}e^{-\frac{(p_x-q_x)^2+(p_y-q_y)^2}{2\Delta p^2}}\ \mathrm{Re}\left[\int f^*(v)dv\int V_\perp(u)f(u)du\right].$$

with

$$\begin{aligned} & \tau=T-t=T\left(1-\frac{d}{\sqrt{X^2+Y^2}}\right) \quad , \quad p_x=m\frac{X}{T} \quad , \quad p_y=m\frac{Y}{T}\ , \\ & f(z)=\sqrt{\frac{m}{2\pi i\hbar\tau}}e^{\frac{im}{2\hbar\tau}\left(Z+\frac{g\tau^2}{2}-z\right)^2}\psi_{q_z,t}(z)\ , \\ & \psi_{q_z,t}(z)=\sum_n c_n(q_z)\chi_n(z)e^{-i\varphi_n(t)}. \end{aligned}$$

The integral over z in formula (II.51) is performed numerically from 0 to $z_{\max}$. The discretization of the integral depends on the De Broglie wavelength $\lambda_{dB} = \frac{h}{mv}$. In this expression, v corresponds to the velocity of the kinetic energy:

$$\frac{1}{2}mv^2 = E_n = \lambda_n \epsilon_g \quad \rightarrow \quad v = \sqrt{\frac{2\lambda_n \epsilon_g}{m}} \tag{II.51}$$

We take $\lambda_{dB}/10$ for the discretization step of the integral.

Quantum propagator method Another method is to use the propagator K, which is the Green function that specifies the probability amplitude for the particle to travel from z to Z in a time τ [144, 145]. This is the method used in [146] and we write it here to check that it gives that same result as (II.51).

For a pure wave function $\psi_{q_z,t}$ at time t, the pure wave function $\psi_{q_z,T}$ at time T after the free fall time τ is conveniently described by a quantum propagator. The propagator is represented as follows in the position representation with position z at time t and Z at time T

$$\begin{aligned} \psi_{q_z,T}(Z) &= \int dz K_\tau^g(z,Z)\psi_{q_z,t}(z) \ , \\ K_\tau^g(z,Z) &= \sqrt{\frac{m}{2i\pi\hbar\tau}} \exp\left(\frac{imS_\tau^g(z,Z)}{\hbar}\right) \ . \end{aligned} \tag{II.52}$$

with $S_\tau^g(z,Z)$ the action of the classical trajectory from z to Z in a constant gravity field g on a time τ [145]

$$S_\tau^g(z,Z) = \frac{(Z-z)^2}{2\tau} - \frac{g\tau\,(Z+z)}{2} - \frac{g^2\tau^3}{24} \ . \tag{II.53}$$

The quantum propagator K_τ^g in presence of the gravity field can easily be rewritten in terms of the same quantity K_τ^0 evaluated in the absence of gravity and of a change of final altitude amounting for the mean free fall height:

$$\begin{aligned} K_\tau^g(z,Z) &= \exp\left(-i\Phi_\tau(Z)\right) K_\tau^0\left(z, Z + \frac{g\tau^2}{2}\right) \ , \\ \Phi_\tau(Z) &= \frac{mg\tau}{\hbar}\left(Z + \frac{g\tau^2}{6}\right) \ . \end{aligned} \tag{II.54}$$

The last formula is interesting as it dissociates the description of gravity by the mean free fall height $\frac{1}{2}g\tau^2$ and that of diffraction by the propagator K_τ^0 containing only the first term $S_\tau^0\left(z, Z + \frac{g\tau^2}{2}\right) = \frac{\left(Z + \frac{g\tau^2}{2} - z\right)^2}{2\tau}$ in the full action S_τ^g. The treatment of gravity is thus compatible with the equivalence principle while that of diffraction depends on the value of $m/\hbar$.

The orthogonal probability current has the following expression:

$$J(\boldsymbol{R},T) = \int d\Omega\ \varpi(\hat{q_e}) \frac{1}{2\pi\Delta v^2\tau^2} e^{-\frac{(p_x-q_x)^2+(p_y-q_y)^2}{2\Delta p^2}} j_{q_z}(Z,T) \ , \tag{II.55}$$

with $j_{q_z}(Z,T)$ the probability current on z axis

$$\begin{aligned} j_{q_z}(Z,T) &= \frac{\hbar}{2im}\left(\psi^*_{q_z,T}(Z)\frac{\partial\psi_{q_z,T}(Z)}{\partial Z} - \psi_{q_z,T}(Z)\frac{\partial\psi^*_{q_z,T}(Z)}{\partial Z}\right) \\ &= \mathrm{Re}\left[\psi^*_{q_z,T}(Z)\frac{\hbar}{im}\frac{\partial\psi_{q_z,T}(Z)}{\partial_Z}\right]. \end{aligned} \tag{II.56}$$

An explicit expression of the current is then obtained by rewriting the wave function $\Psi_{q_z,T}$

$$\begin{aligned} \psi_{q_z,T}(Z) &= e^{-i\Phi_\tau(Z)}\int dz\ K^0_\tau\left(z, Z+\frac{g\tau^2}{2}\right)\psi_{q_z,t}(z)\ , \\ K^0_\tau\left(z, Z+\frac{g\tau^2}{2}\right) &= \sqrt{\frac{m}{2i\pi\hbar\tau}}e^{\frac{im}{2\hbar\tau}\left(Z+\frac{g\tau^2}{2}-z\right)^2}. \end{aligned} \tag{II.57}$$

as well as its gradient versus Z

$$\begin{aligned} \frac{\hbar}{im}\frac{\partial\psi_{q_z,T}(Z)}{\partial_Z} &= e^{-i\Phi_\tau(Z)}\int dz\ V_\perp(z)K^0_\tau\left(z, Z+\frac{g\tau^2}{2}\right)\psi_{q_z,t}(z)\ , \\ V_\perp(z) &= |V_z| = \left|\frac{Z-z}{\tau} - \frac{g\tau}{2}\right|. \end{aligned} \tag{II.58}$$

The expression of the current is then

$$\begin{aligned} J(\boldsymbol{R},T) &= \int d\Omega\ \varpi(\hat{q_e})\frac{1}{2\pi\Delta v^2\tau^2}e^{-\frac{(p_x-q_x)^2+(p_y-q_y)^2}{2\Delta p^2}}j_{q_z}\ , \\ j_{q_z} &= \mathrm{Re}\left[\int dz\ K^0_\tau\left(z, Z+\frac{g\tau^2}{2}\right)^*\psi^*_{q_z,t}(z)\int dz\ V_\perp(z)K^0_\tau\left(z, Z+\frac{g\tau^2}{2}\right)\psi_{q_z,t}(z)\right]. \end{aligned} \tag{II.59}$$

and is the same as (II.51).

Equation (II.59) describes quantum diffraction with the effect of gravity accounted for by the altitude change $Z \to Z + \frac{g\tau^2}{2}$. It allows to discuss easily the approximation of far-field diffraction which was used in [120]. When τ is longer than a time of the order of $\frac{mz^2_{\max}}{\hbar}$, the far-field limit can be used and the current expressed in terms of the momentum distribution at the end of the mirror. With the numbers used in [120], this approximation gave a fairly good result. With the numbers used here, the approximation can no longer be used, and we have to proceed with the more demanding numerical evaluation of the formula (II.59).

II.4.3 Interference pattern on the detector

We represent in figure II.11 the current obtained with formula (II.51) or (II.59) as function of Y and T by fixing $X = 0$ and $Z = -H$. This figure is centered at the classical detection point $(Y,T) = (d + v_e\tau, d/v_e + \tau) \approx (302\text{ mm}, 296\text{ ms})$. It clearly shows horizontal interference fringes, which means that the interference is now essentially encoded on the

time of arrival, directly related by the free fall equations to the vertical momentum at the end of the mirror. The pattern is organized around a most probable line corresponding to the diagonal $Y = v_e T$. The units are given in millimeters for Y and in milliseconds for T.

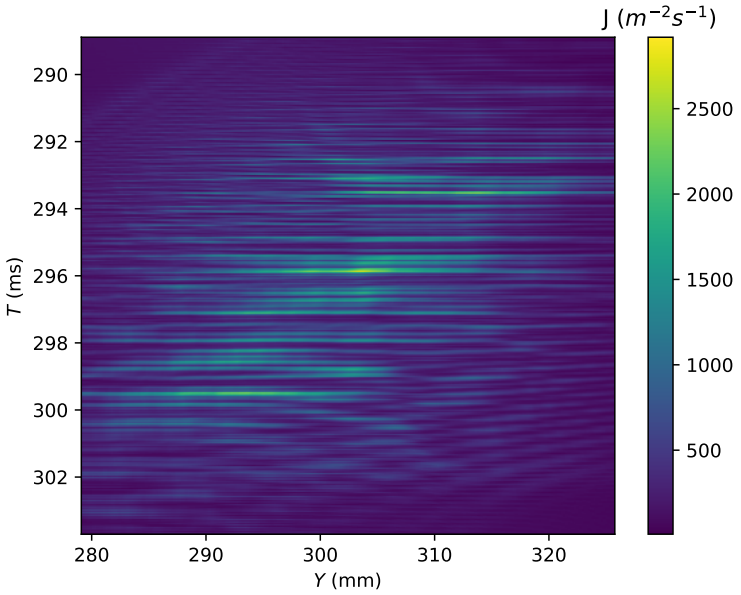

Figure II.11: Probability current density $J(Y,T)$ on the detection plate, by fixing $Z = -H$ and $X = 0$. Parameters: $f = 20$ kHz, $\delta E = 10$ μeV, $n_{\max} = 1000$. [146]

In order to understand the relation between the 2D figures of the momentum distribution and the annihilation current (figures II.7 and II.11), it is worth looking at the anamorphosis relations. In the detection pattern (figure II.11), the constructive interferences are horizontal lines, i.e. $\delta T = 0$. From the formula (II.43), we get the resulting variations of v_z and t:

$$\delta T = 0 \;\rightarrow\; \delta v_z = \frac{\delta v_z}{\delta t}\delta t = \left(\frac{Z}{(T-t)^2} - \frac{g}{2}\right)\delta t \approx \left(\frac{Z}{\tau_H^2} - \frac{g}{2}\right)\delta t = -g\;\delta t. \qquad \text{(II.60)}$$

It follows that the bright oblique lines corresponding to constructive interferences and classical free fall movement in figure II.7 become the bright horizontal lines on figure II.11 which correspond to constructive interferences and are parallel to the Y axis on the detector plate.

II.4.4 Cuts of the interference pattern

In order to discuss in more details the interference pattern in figure II.11, we represent a cut of this figure along the diagonal $Y = v_e T$ corresponding to the most probable line in

figure II.11. We plot it as a function of time T around the center 296 ms in figure II.12. The space and time positions of the annihilation event on the detector are translations of variable at the end of the mirror according to the translation law (II.44). This explains why the interference pattern in space obtained has nearly the same shape as the one obtained for the momentum distribution at the end of the mirror (figure II.8). A zoom of this plot is represented in figure II.13 which emphasizes that the pattern is indeed an interference signal rather than a mere noise.

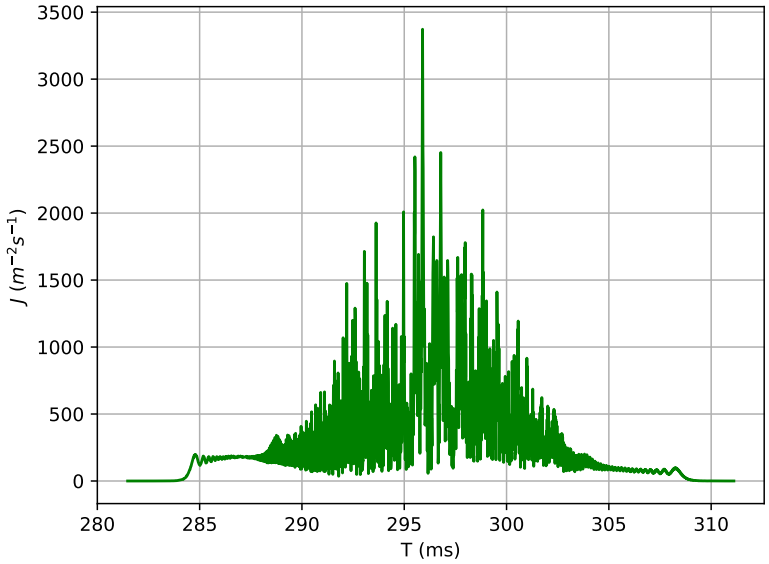

Figure II.12: Probability current density J in $m^{-2}s^{-1}$ on the detection plate, by fixing $Z = -H$, $X = 0$ and $Y = v_eT$, for $n_{\max} = 1000$.

Changing the number $n_{\max}$ of GQS by 10% (from $n_{\max} = 1000$ to $n_{\max} = 900$), we observe in figure II.14 that the pattern isn't significantly modified, which shows that the signal is deterministic rather than chaotic. This property also implies that the specification of this number $n_{\max}$ is not critical.

The interference pattern on the detection screen is characterized by its contrast and its fringe-spacing. A large number of Gravitational Quantum States (GQS) leads to a smaller contrast and finer structure, because the different states present minima and maxima at different positions. This is illustrated in the comparison between the figure II.13 for $n_{\max} = 1000$ and the figure II.15 for $n_{\max} = 100$.

The final interference pattern depends sensibly on the choice of some parameters that can be tuned for preparing a given initial state: the trap frequency f, the height of the center h of the initial wave packet and the photodetachment recoil velocity v_e. The change of the two first parameters leads to different ways of populating the gravitational quantum state. A smaller frequency trap corresponds to a smaller energy dispersion and

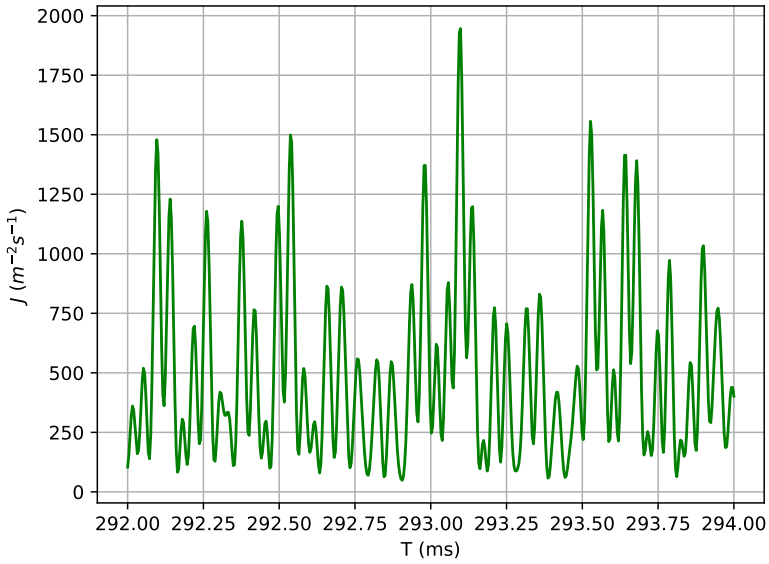

Figure II.13: Zoom of figure II.12 to highlight interference fringes.

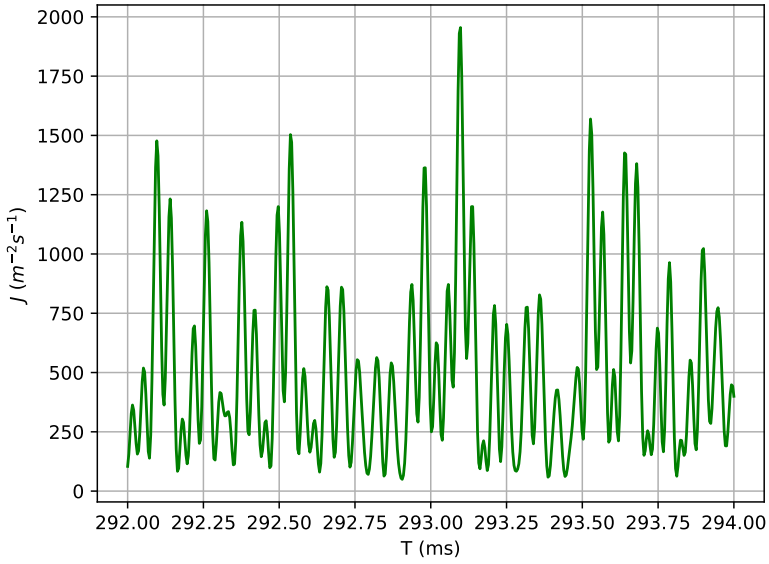

Figure II.14: Interference pattern at detection for $n_{\max} = 900$.

tends to decrease the number of states in the gravitational quantum state decomposition. Similarly, a higher h leads to taking into account Gravitational Quantum States with

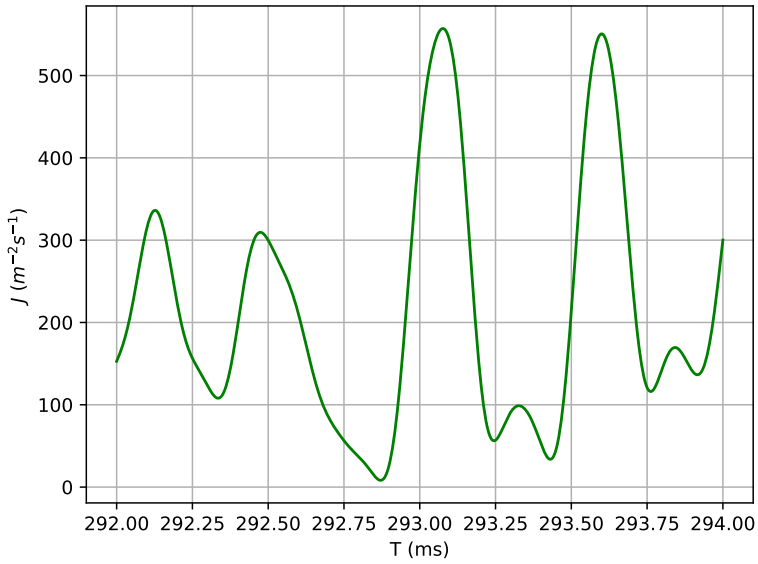

Figure II.15: Interference pattern at detection for $n_{\max} = 100$.

larger energy, that oscillate more rapidly.

We now have all the necessary ingredients to model the evolution of the wave packet from the initial slit to detection, including quantum bounces on the mirror. We will use them to estimate the precision of the experiment with the statistical methods described in chapter I, and compare with the purely classical design.

II.5 Estimation of the uncertainty

Previously, we saw that the figure of the current contains interference fringes, even by taking into account photodetachment process. The question is now to what extent photodetachment degrades the accuracy.

As the distance between fringes depends on g, it could be tempting to measure g directly from it. This technique is however unpractical here, because we have only a small number of annihilation events to sample the details of the probability distribution. We use much more robust methods detailed in the chapter I of this thesis to estimate the parameter g and then deduce a variance for this estimation: Cramer-Rao analytical method and Monte-Carlo numerical method. This analysis study was already performed in [120], but without taking into account the photodetachment process: it led to an uncertainty of $\sigma_g/g \approx 8 \cdot 10^{-6}$. We saw previously that the photodetachment process doesn't degrade that much the interference pattern, so one would expect that the precision wouldn't be degraded as well. We will confirm this conclusion below.

We restrict the estimation of the uncertainty on the range of parameters that can be

experimentally achieved, as known from the existing analysis of the GBAR experiment (see table II.2).

Parameter	**Value**
Trap frequency	$f = 20$ kHz
Initial velocity dispersion	$\Delta v = 6.3$ cm/s
Photodetachment energy	$\delta E = 10$ μeV
Photodetachment velocity	$v_e = 1.02$ m/s

Table II.2: Values of the parameters of the trap and photodetachment process.

Moreover, the simulations are performed for $N = 1000$ $\bar{H}$ atoms developing their wave functions on the $n_{\max} = 1000$ first GQS, which corresponds to $N_c = 260$ atoms detected. Atoms annihilate on a horizontal detector plate, each detection point being characterized by its position in space (X_i, Y_i) and time (T_i), the coordinate $Z_i = -30$ cm being fixed. Cylindrical coordinates are used, each detection point being characterized by a radial distance from the center of the mirror (R_i) and an azimuth angle (Φ_i).

II.5.1 Monte-Carlo simulation

The generation of events is a bit different than the one used in the classical design, since it's very difficult to perform a Monte-Carlo simulation in the GQS region. Detection events are generated directly from the expression (II.51) or (II.59) of the current J at detection. We choose randomly N_c detection events in the probability distribution J corresponding to the value $g_0 = 9.81$ m/s^2. We consider that the set of detection events $\mathcal{D}$ simulates the output of one experiment:

$$\mathcal{D} = (R_i, \Phi_i, T_i) \ , \ 1 \leqslant i \leqslant N_c. \tag{II.61}$$

The atomic evolution from the source to the detector doesn't depend on the azimuth angle Φ. We can then restrict our analysis by fixing $\Phi = \frac{\pi}{2}$, which produces an equivalent 2D analysis which gathers all available information. The $y - z$ plane (that is also $\Phi = \frac{\pi}{2}$ as azimuth angle) corresponds to the most probable plane in the distribution of velocities.

The figure II.16 shows likelihoods corresponding to 10 independent random draws. The colors have no meaning, they only allow one to distinguish the various functions. The horizontal axis scales as $\frac{g-g_0}{g_0}$. We observe that the likelihoods have nearly Gaussian shapes with nearly equal variances, the main difference from one to the other being the maximum value which corresponds to an estimation of g.

As the likelihoods are gaussian functions, we use the max likelihood method described in part I to get an estimator $\widehat{g}$ of the parameter g as would be done in the data analysis of the experiment. In order to give a robust estimation of the variance, we finally repeat the full procedure for M different random draws of the N_c points. The histogram shown in figure II.17 corresponds to $M = 10000$ such draws of N_c points.

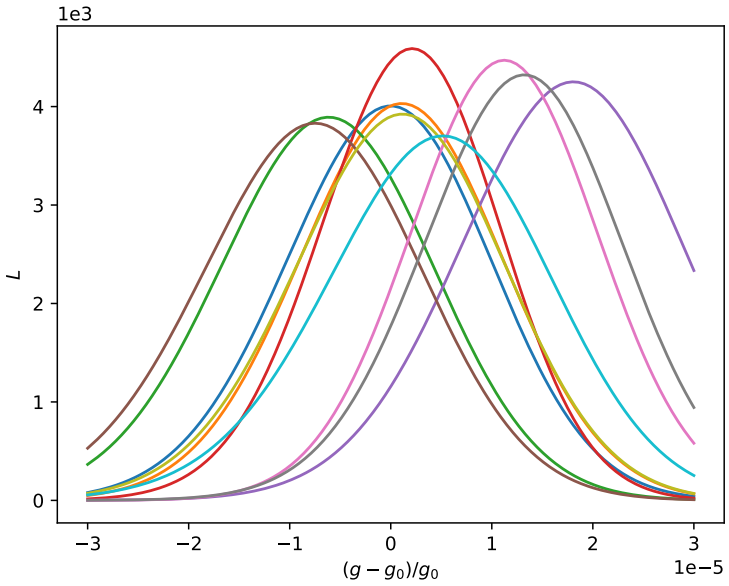

Figure II.16: Normalized likelihood functions calculated for 10 random draws of $N_c = 260$ atoms in the quantum design [146].

This histogram has nearly a gaussian shape, with a dispersion which corresponds to the dispersion of the likelihoods in average. From this histogram, we can extract the average μ_g (around 9.81 m/s^2) and the dispersion σ_g^{MC} of the estimator $\hat{g}$, from which we calculate the relative uncertainty [146]:

$$\sigma_g^{MC}/g_0 \approx 1.0 \cdot 10^{-5}. \tag{II.62}$$

In the case without photodetachment, with the same design parameters and an initial horizontal kick $v_0 = 1.02$ m/s, about 995 atoms are detected since the dispersion of initial vertical velocity is much smaller and the relative uncertainty obtained is:

$$\sigma_g^{MC}/g_0 \approx 5.8 \cdot 10^{-6}. \tag{II.63}$$

Taking into account the fact that the number of detected atoms is reduced by a factor 0.26 by the spread of photodetachment recoil, we see that the latter only slightly decreases the precision per detected atom. In other words, the photodetachment degrades the precision not so much as a result of blurring of the interference figure, but rather because about 74% of the initial atoms are absorbed in the slit above the quantum mirror.

II.5.2 Cramer-Rao lower bound and statistical efficiency

The Cramer-Rao method is performed by the same way as previously described in part I for the classical case, but here the detector only has one spatial component Y. The

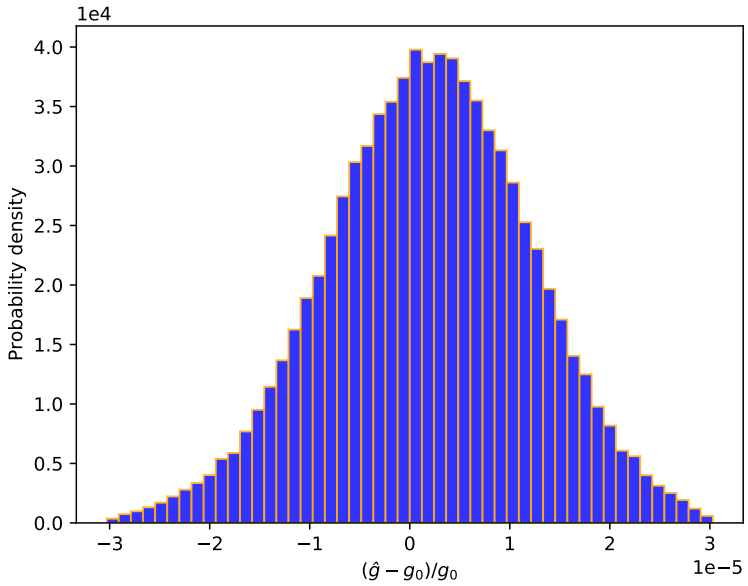

Figure II.17: Normalized histogram of the relative variations $(\hat{g} - g_0)/g_0$ obtained by repeating 10000 times the Monte-Carlo simulation on $N_c = 260$ atoms in the quantum design [146].

expression of the Fisher information is then:

$$\mathcal{I} = \int dY\, dT\, \frac{(\partial_g J_g(Y,T))^2}{J_g(Y,T)} \tag{II.64}$$

with J_g the current whose expression is (II.51) or (II.59).

Then the Cramer-Rao lower bound is given by the number of initial atoms N and the Fisher information $\mathcal{I}$:

$$\sigma_g^{CR} = \frac{1}{\sqrt{N\,\mathcal{I}}}. \tag{II.65}$$

We note that N is the initial number of atoms if J_g accounts for the absorption of atoms in the slit above the mirror. In other words, $\mathcal{I}_g$ is the Fisher information per incident atom, which is reduced by the fact that around 74% of the atoms are absorbed and do not bring any information on the value of g.

In the present problem, the relative uncertainty obtained by evaluating (II.65) is effectively slightly smaller than the one (II.62) calculated by the Monte Carlo simulation:

$$\sigma_g^{CR}/g_0 \approx 9.8 \cdot 10^{-6}. \tag{II.66}$$

This means that the statistical efficiency [115], defined as the ratio between (II.66) and

(II.62) is good (e close to 1)

$$e = \left(\frac{\sigma_g^{CR}}{\sigma_g^{MC}} \right)^2 \approx 0.96. \tag{II.67}$$

From an experimental point of view, a good efficiency means that the unique random draw to be obtained in one experiment is representative of the variety of results for different random draws in the numerical simulations. The dispersion σ_g^{MC} is obtained by repeating a numerical experiment in conditions where the real experiment can't be repeated due to the small number of available $\bar{H}$ atoms. It is more reliable than the value obtained directly on a single draw corresponding to a single experiment. Thanks to the good efficiency however, the experiment value of the estimator σ_g obtained in a single draw is close to it while its relative dispersion is small.

II.5.3 Variation of $n_{\max}$

We now want to evaluate how the number of Gravitational Quantum States $n_{\max}$ influence the precision of the experiment. To do so, we use the Cramer-Rao analytical method, we calculate the Fisher information per atom detected and the relative uncertainty.

	$n_{\max} = 100$	$n_{\max} = 500$	$n_{\max} = 1000$
N_c	118	206	269
$\mathcal{I}_g$ per atom	$4.8 \cdot 10^4$	$1.2 \cdot 10^5$	$4.2 \cdot 10^5$
σ_g/g	$4.3 \cdot 10^{-5}$	$2.1 \cdot 10^{-5}$	$9.8 \cdot 10^{-6}$

Table II.3: Number of atoms detected N_c, Fisher information per atom detected and relative uncertainty σ_g/g obtained for different number of Gravitational Quantum States.

It follows from our calculations that a large number of Gravitational Quantum States is preferable, as the number of atoms detected is higher, as well as the Fisher information per atom detected. A more complex pattern contains more information on the value of the parameter g, so that we can at the end extract a better estimation of g.

II.5.4 Comparison classical - quantum cases

We now compare quantitatively the uncertainty of the quantum interference method with that of the classical timing measurement corresponding to the current design of GBAR, by using the same parameters in the quantum and classical methods: $f = 20$ kHz, $h = 10$ μm, horizontal polarization of the laser and $H = 30$ cm). The relative uncertainty obtained for the classical design is:

$$\sigma_g^{\text{classical}}/g_0 \approx 3.3 \cdot 10^{-2} \tag{II.68}$$

$$\sigma_g^{\text{classical}}/\sigma_g^{\text{quantum}} \approx 3300. \tag{II.69}$$

The calculations presented here show that a spectacular improvement of σ_g/g by about 3 orders of magnitude is attained by using quantum interference methods rather than classical timing. The quantum interference pattern contains much more information than the classical one, which explains why the uncertainty in the estimation of g is much better. Fine details act as thin graduations that make it easier to observe small displacement and distortion on the probability current distribution when g varies.

As discussed above, this quantum analysis is reliable as long as the variance obtained in the Monte-Carlo simulation is close to the Cramer-Rao lower bound. When the number of atoms detected N_c decreases, the distance of the two values increases, meaning that the statistical efficiency is degraded. A smaller recoil velocity would enhance the duration of the interference period above the mirror while also increasing the probability of the atom to be annihilated on the mirror.

For a more realistic treatment of the uncertainty calculation, we should account for the quantum reflection on the mirror and on the detection plate by adding an energy dependent annihilation probability at each bounce of the atom above the surface [13, 24]. Moreover, the effect of position resolution at the detection plate [107] should be included in the analysis as it can blur the finest fringes. These advances will be needed for a precise analysis of the quantum experiment when the latter will be built up and performed but they will not change the main result obtained in this thesis, namely that the quantum design leads to a better accuracy than the classical one.

Conclusion

The exploration of a system as simple as a anti-hydrogen atom offers beautiful and interesting physics to study: propagation of an atomic wave packet in a gravitational field, quantum reflection of the matter wave on a material surface, use of Gravitational Quantum States to improve the accuracy of a measurement. An important goal of our work was to highlight the crucial experimental parameters which affect the detection pattern and the accuracy of the GBAR experiment.

Conclusions on the classical experiment

In the first part of this thesis, we have evaluated the accuracy to be expected for the classical timing measurement of free fall acceleration $\bar{g}$ of antihydrogen in the GBAR experiment, accounting for the recoil transferred in the photodetachment process. During a free fall on a macroscopic height, although the wave packet propagates classically, its quantum nature imposes that it is extended in phase space, which results in a spread of the time of arrival distribution on an ideal detector. Using Monte-Carlo numerical simulations and analytical calculations of the Cramer-Rao bound, we have shown that the final accuracy is mainly determined by the width of the initial velocity dispersion in the trap and not by the larger velocity dispersion due to the photodetachment process. This important result will allow to set a large enough excess energy above photodetachment threshold (say $\delta E > 30$ μeV) and thus to get a better photodetachment efficiency.

The source of antihydrogen atoms, precisely an ion trap from which neutral atoms are extracted by the photodetachment process, has a complicated geometry which has to be masked for an efficient modelling of the experiment. We have included in the analysis the presence of two disks symmetrically positioned in the vicinity of the source of antiatoms to hide these details and we have shown that their presence creates a shadow zone with symmetrical cuts on the detection current, which can be used to improve the measurement accuracy. More precisely, the accuracy is improved thanks to the additional information on the value of g gained from the presence of shadow edges, the positions of which depend on g. The polarization of the laser should be horizontal in order to launch atoms preferably in the free interval between the two disks.

The detection surface of the GBAR chamber is not ideal, it behaves as reflective surface and matter waves can bounce on it. This quantum reflection is a probabilistic process which depends on the characteristics of the material surface and on the orthogonal

velocity of the atom. These subtle processes lead to detection of $\bar{H}$ atoms in the shadow zones, which could have been detrimental for the accuracy. We have however shown that quantum reflection only slightly reduces the advantage coming from the gain of information associated with shadow edges. We also highlighted the need to have a very good polishing of detection surfaces to prevent diffuse quantum reflection.

Our results have led to a change of the design of the GBAR experiment, with the aim of optimizing the accuracy to be obtained in the experiment. The precise analysis have to be redone with the modified design. This will affect the precise numbers but not the main qualitative conclusions presented in this thesis.

Conclusions on the quantum experiment

In the second part of this thesis, we have studied in details the quantum design of the GBAR experiment already proposed in the thesis of P.P. Crépin [73]. We have improved the analysis presented there by taking into account the photodetachment process and also by developing a more rigorous description of antimatter wave propagation. The goal of the quantum design is to improve drastically the precision of the experiment compared to the classical free fall timing. We described precisely the evolution of the matter wave in this new experimental setup made of two parts: in the first part, the atom bounces on a high reflecting surface, thus building quantum interferences between Gravitational Quantum States; in the second part, a macroscopic free fall reveals the interferences on the detector. The numerical calculations were done for a superposition of thousand states, which corresponds to about 26% of atoms detected with the parameters used in this analysis.

We then used the same statistical tools as in the classical design to estimate $\bar{g}$, i.e. Monte Carlo simulation and Cramer-Rao lower bound estimation. We checked that a good statistical efficiency was reached with this method, which is quite surprising regarding the complexity of the interference pattern and the relatively low number of atoms probing this pattern. The main conclusion of this part is that the photodetachment process degrades the precision mainly because the spreading of the vertical velocity leads to a loss of atoms absorbed in the slit above the quantum mirror. Meanwhile, the blurring of the interference pattern which could have affected the precision of the quantum experiment is rather small.

In the end, the relative uncertainty σ_g/g is spectacularly improved when going from the classical timing measurement to the quantum one. Indeed, with the set of parameters considered in the present paper, we get a relative accuracy of $3.3 \cdot 10^{-2}$ for the classical design and about 10^{-5} for the quantum one, improving the uncertainty of the initial classical design by more than 3 orders of magnitude. The main reason for this improvement is that the quantum interference pattern contains much more information on the value of g than the classical pattern. Fine details act as thin graduations that make it easier to observe small displacement and distortion of the probability current distribution when g varies. Of course, the quantum experiment is more difficult than the classical one and the latter will be performed before the former.

Further advances would be necessary for a fully realistic estimation of the uncertainty. In particular, the quantum reflection on the mirror and on the detection plate should be accounted for and the effect of position resolution at the detection plate should be included in the analysis as it can blur the finest fringes. It would also be necessary to treat the effect of the shifts of Gravitational Quantum States on the Casimir-Polder potential, an effect which has already been calculated with the required accuracy [73]. These advances will be needed for a precise analysis of the quantum experiment when it will be performed but they will not change the main result obtained in this paper, namely that the quantum design leads to a better accuracy than the classical one.

The precise description of the Gravitational Quantum States offers new perspectives for a measurement of the free fall acceleration using quantum spectroscopic techniques. Such "quantum bouncer" experiments could take advantage of spectroscopic and interferometric measurement techniques to perform fundamental tests with an unprecedented resolution. This work opens new ways to test tiny effects and new interactions of the microscopic world.

Perspectives

GBAR event reconstruction and Geant 4 simulation A more realistic description of the experiment should take into account the event reconstruction process. During an annihilation event, the proton p of H and antiproton $\bar{p}$ of $\bar{H}$ combine to form pions (3 in average by annihilation). Those pions are then detected with micromegas (particularly for spatial position) and scintillators (for the time of flight). Pions loose energy if they cross detection surfaces. The process of reconstruction consists in finding the position of annihilation vertex of $\bar{H}$ once we know the spatial positions of the detected secondary particles (like pions), with a topology much different from that of a typical cosmic ray. This reconstruction process can be easily performed with Geant4, which is a Monte-Carlo plateform to simulate the interactions of elementary particles with matter [147]. It is very useful for the reconstruction of events and to model complicated geometries. The difference between the real annihilation position and the reconstructed one is due to the resolution of micromegas (400 μm in average). This reconstruction also allows to distinguish between "real" particles and cosmic particles (like muons). In the GBAR collaboration, the Geant4 simulation allows the Monte-Carlo generation of events, reconstruction process and analysis. It will be performed at ETH Zürich.

New statistical methods In this thesis, we focused on two statistical methods to estimate the precision of the GBAR experiment: the Cramer-Rao analytical method and the Monte-Carlo numerical method. However, those methods imply the computation of the probability current J, which could be problematic if the physical processes considered are complex. Machine Learning (ML) method can be used for the analysis process, it requires the Monte-Carlo generation of events but doesn't need the computation of the annihilation current J. We detail here an example of ML process than can be implemented for the analysis of the GBAR cylindrical chamber. We consider an

interval $[g_{\min}, g_{\max}]$ of values of g centered on $g_0 = 9.81\ m/s^2$. We proceed Monte-Carlo generation of $N = 1000$ atoms for those different values of g, and we extract the annihilation data for each atom (radius r, height z, time of flight t and detection surface s). This database constitutes the dataset of the ML model. The statistical model can be implemented by using the modules `TensorFlow` or `Keras` in Python. Different types of model can be implemented, like a multi-variable linear regression model, artifical neural network, convolutional neural network,... Once the model is built, the model has to be trained by using our dataset. More precisely, the Python algorithm will iteratively adjust the parameters of the model, gradually finding the best combination of weights and bias to minimize a loss function (Mean Absolute Error for example). We now proceed $M = 10000$ Monte-Carlo random draws for the standard value $g_0 = 9.81\ m/s^2$. For each simulation, we extract the values of r, z, t and s, and we predict the value of g based on the model built previously. The list of $\widehat{g}$ estimated can be plotted in an histogram, and the relative uncertainty can be extracted. We note that these suggestions are only qualitative for the moment and more simulations would be needed to confirm its interest for GBAR analysis.

In addition, the deep learning approach with neural network can be used to analyze data from antimatter trap experiments and identify antihydrogen annihilation signatures without relying on explicit track reconstruction. In this case, the model is trained using Monte Carlo simulated data to distinguish between antihydrogen-like signal and background annihilation events. This novel technique improves the performance compared to the traditional track and vertex reconstruction method, as shown in [148] for the ASACUSA antihydrogen experiment at CERN. Improving the efficiency of the antihydrogen annihilation detection plays a central role in the final sensitivity of the antihydrogen experiments. Machine learning and deep learning techniques are more and more popular in High-Energy physics, for searches of exotic particles, event classification, fast simulation [149].

Gravitational Quantum States for Hydrogen atoms Analogously to the GBAR quantum design for antihydrogen atoms, we can also investigate quantum interferences of hydrogen atoms bouncing on a quantum reflection mirror. The measurement of Gravitational Quantum States (GQS) with atomic hydrogen will be conducted at ETH Zürich, and it would be the first experimental proof of Gravitational Quantum States for atoms. This experiment is part of the GRASIAN collaboration (*GRAvity, Spectroscopy and Interferometry with ultra-cold Atoms and Neutrons*), which pursues research with the lightest neutral particles/atoms at lowest kinetic energies, nearly at rest.

It was noted above that the ultra cold antihydrogen atoms are statistically limited. Hydrogen, on the hand, is available in much larger fluxes even when cryogenically cooled so that it promises better statistics. Hydrogen atoms have a large lifetime on the surfaces considered, so it should be possible to trap them for long enough to produce interferences between Gravitational Quantum States. The experiment is decomposed in different steps, from the production of hydrogen from dihydrogen to its detection with a microchannel plate detector (see figure 1). Like in the GBAR quantum design, an hydrogen beam

is sent onto a horizontal mirror on which atoms bounce, so that the quantum paths corresponding to different GQS interfere. The interference pattern produced at the end of the mirror is revealed by letting atoms evolve through free flight to their detection.

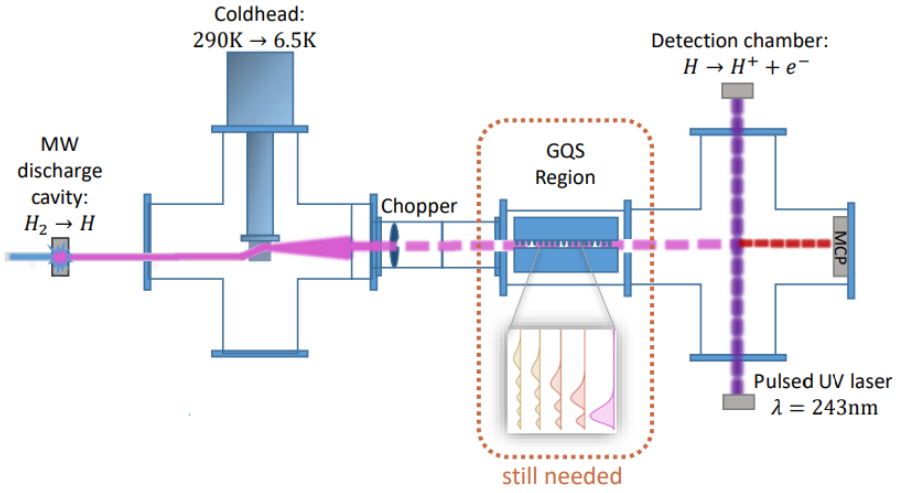

Figure 1: Schematic representation of the experimental setup, from the production of H_2 to the detection of H atoms [150].

This GRASIAN experiment may be considered as a "testbed" for quantum projects in the GBAR experiment. Indeed, it's very useful to study GQS for hydrogen atoms (normal matter) at first, before applying it to atoms of antihydrogen. Gravitational quantum states are a promising tool for metrology, as their energy levels depend on the local gravitational acceleration and could bear the signature of unknown short-range forces. Methods developed in part II of this thesis may be applied for calculating the quantum interference signals which will be studied by the GRASIAN collaboration.

Whispering Gallery States for Hydrogen atoms This is also the case for experiments using a curved mirror instead of a horizontal plane mirror. Localization of waves near a curved material surface is known as the Whispering Gallery (WG) effect [151] and it has been an object of growing interest due to its multiple applications [98, 152]. In the quantum mechanical description, the WG effect consists in the evolution of a quantum object settled in long-living quasi-stationary states near a curved surface [153] (see figure 2). Such effect has already been observed for neutrons by the team of V. Nesvizhevsky [154]. Deeply bound WG states are long-living and weakly sensitive to surface potential; highly excited states are short-living and very sensitive to the wall potential shape.

Applied to the hydrogen atoms, the WG states would be situated some nanometers from the reflecting surface (against some micrometers for a plane mirror). Extreme smallness of both WG energies (~ 1 peV) and contributions of other fundamental interactions provide the high sensitivity of WG to the presence of new interactions between particle and mirror. The sensitivity depends on WG lifetimes τ and particle phase-space

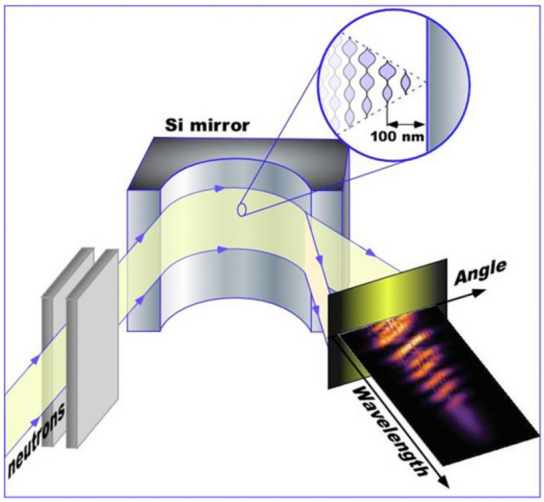

Figure 2: Illustration of the neutron whispering gallery experiment [154].

densities ρ. Studies with hydrogen promise a dramatic increase of ρ and τ compared to those achieved with neutrons, then leading to a better sensitivity. New fundamental interactions would equally modify energies of WG states of hydrogen, allowing to test the existence of a short-range fifth fundamental force for example [155, 156]. Prospects for the exclusion or possible detection of hypothetical interactions are bright in next generation hydrogen gravity experiments [157]. Again the research presented in this thesis opens new ways to probe tiny effects of the microscopic world and comes as a complement to the approaches testing the Standard Model besides High-Energy Physics explored at colliders [44, 156].

Appendices

A Propagation of a wave paquet in a gravitational field

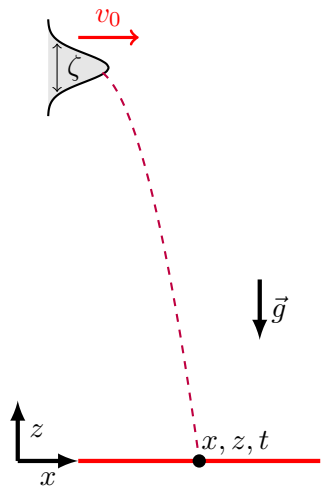

Figure 1: Illustration of the free fall of a wave paquet with initial dispersion ζ.

We start with a gaussian wave paquet in x and z axes, and we want to study its propagation in a gravitational field (with gravity along the z axis). We note $(\overline{x}_0,\ \overline{z}_0)$ the average initial position, $(\overline{p}_{x_0},\ \overline{p}_{z_0})$ the average initial momentum, $(\zeta_x,\ \zeta_z)$ the initial spatial dispersions and $(\Delta v_x,\ \Delta v_z)$ the initial velocity dispersions. The initial state can be written in position representation

$$\begin{aligned}
\Psi_0(x_0, z_0) &= \phi_0(x_0)\ \psi_0(z_0)\ , \qquad (A.1)\\
\phi_0(x_0) &= \left(\frac{1}{2\pi\zeta_x^2}\right)^{1/4} \exp\left(-\frac{(x_0-\overline{x}_0)^2}{4\zeta_x^2} + \frac{i}{\hbar}\overline{p}_{x_0}(x_0-\overline{x}_0)\right)\ ,\\
\psi_0(z_0) &= \left(\frac{1}{2\pi\zeta_z^2}\right)^{1/4} \exp\left(-\frac{(z_0-\overline{z}_0)^2}{4\zeta_z^2} + \frac{i}{\hbar}\overline{p}_{z_0}(z_0-\overline{z}_0)\right).
\end{aligned}$$

or equivalently in momentum representation

$$\begin{aligned}
\widetilde{\Psi}_0(p_{x_0}, p_{z_0}) &= \widetilde{\phi}_0(p_{x_0})\ \widetilde{\psi}_0(p_{z_0})\ , \\
\widetilde{\phi}_0(p_{x_0}) &= \left(\frac{1}{2\pi\Delta p_x^2}\right)^{1/4} \exp\left(-\frac{(p_{x_0}-\overline{p}_{x_0})^2}{4\Delta p_x^2} - \frac{i}{\hbar}p_{x_0}\overline{x}_0\right)\ , \\
\widetilde{\psi}_0(p_{z_0}) &= \left(\frac{1}{2\pi\Delta p_z^2}\right)^{1/4} \exp\left(-\frac{(p_{z_0}-\overline{p}_{z_0})^2}{4\Delta p_z^2} - \frac{i}{\hbar}p_{z_0}\overline{z}_0\right).
\end{aligned} \tag{A.2}$$

Moreover, the expression of the Wigner quasi-probability distribution (defined as a mixed position-momentum representation) at initial state is:

$$\begin{aligned}
W_0(x_0, z_0, p_{x_0}, p_{z_0}) = \frac{1}{(\pi\hbar)^2} \quad & \exp\quad \left(-\frac{(x_0-\overline{x}_0)^2}{2\zeta_x^2} - \frac{(z_0-\overline{z}_0)^2}{2\zeta_z^2}\right) \\
& \exp\quad \left(-\frac{(p_{x_0}-\overline{p}_{x_0})^2}{2\Delta p_x^2} - \frac{(p_{z_0}-\overline{p}_{z_0})^2}{2\Delta p_z^2}\right).
\end{aligned} \tag{A.3}$$

We consider that the initial velocity is null: $(\overline{p}_{x_0}, \overline{p}_{z_0}) = (0,0)$. The expression of the wave function after the propagation along the x axis is, by noting S_t the classical action:

$$\begin{aligned}
S_t(x_0, x) &= \frac{m(x-x_0)^2}{2t}\ , \\
\phi_t(x) &= \int \mathrm{d}x_0\ \phi_0(x_0)\sqrt{\frac{m}{2\pi i\hbar t}}\exp\left(\frac{iS_t(x_0,x)}{\hbar}\right) \\
&= \left(\frac{1}{2\pi(\zeta_x + i\Delta v_x t)^2}\right)^{1/4} \exp\left(-\frac{\Delta v_x t\ S_t(\overline{x}_0, x)/\hbar}{\zeta_x + i\Delta v_x t}\right).
\end{aligned} \tag{A.4}$$

The propagation along the z-axis has to take into account gravity:

$$\begin{aligned}
S_t(z_0, z) &= \frac{m(z-z_0)^2}{2t} - \frac{mgt(z_0+z)}{2} - \frac{mg^2t^3}{24}\ , \\
\psi_t(z) &= \int \mathrm{d}z_0\ \psi_0(z_0)\sqrt{\frac{m}{2\pi i\hbar t}}\exp\left(\frac{iS_t(z_0,z)}{\hbar}\right) \\
&= \left(\frac{1}{2\pi(\zeta_z + i\Delta v_z t)^2}\right)^{1/4} \exp\left(-\frac{\frac{\Delta v t}{\hbar}S_t(\overline{z}_0, z) + \frac{i}{2\Delta v}gt(z - \overline{z}_0 + gt^2/6)}{\zeta_z + i\Delta v_z t}\right).
\end{aligned} \tag{A.5}$$

After time t, by assuming that $\zeta_x = \zeta_z \equiv \zeta$, the Wigner distribution can be written in terms of the classical propagator laws:

$$\begin{aligned}
W_t(x, z, p_x, p_z) &= W_0\left(x - \frac{p_x}{m}t, z - \frac{p_z}{m}t - \frac{g}{2}t^2, p_x, p_z + mgt\right) \\
&= \frac{1}{(\pi\hbar)^2}\exp\left(-\frac{(x-\overline{x}_0 - p_x t/m)^2 + (z - \overline{z}_0 - p_z t/m - gt^2/2)^2}{2\zeta^2}\right) \\
&\qquad \exp\left(-\frac{p_x^2 + (p_z + mgt)^2}{2\Delta p^2}\right).
\end{aligned} \tag{A.6}$$

We plot in figure 2 the Wigner quasi-distribution W_t in (z, p_z) space while x and p_x coordinates follow the classical trajectory. The initial wave packet is gaussian, and we take a free fall height of $H = 20\ l_g \approx 11.7\ \mu$m for more visibility in the plot. Marginal distributions $\psi_t(z)$ and $\widetilde{\psi}_t(p_z)$ are also represented in figure 2. The classical free fall time of a classical particle dropped with no initial velocity is defined as:

$$T_H = \sqrt{\frac{2H}{g}}. \tag{A.7}$$

The Wigner function is plotted at $t = 0$, $t = t_H/2$ and $t = t_H$. We can note that the momentum distribution is centered on the classical momentum $p_z^{cl}(t) = -mgt$ and that it keeps its shape. The center of the position distribution also moves along the classical trajectory $z^{cl}(t) = H - gt^2/2$ but the wave packet spreads as it falls.

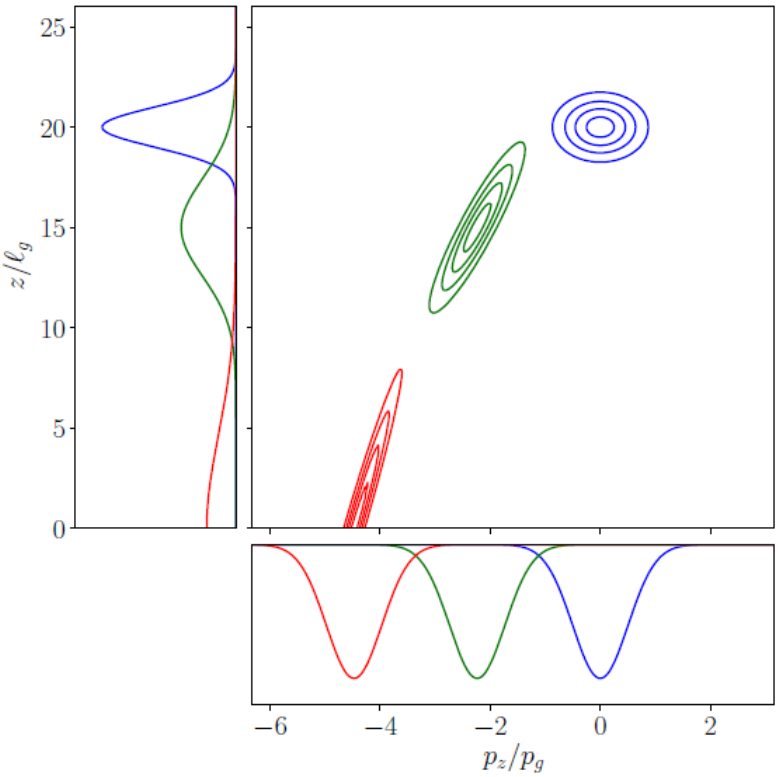

Figure 2: Freely falling Gaussian wave packet dropped from height $H = 20\, lg$ with no average initial velocity, at times $t = 0$ (blue), $t = t_H/2$ (green) and $t = t_H$ (red), with $t_H = \sqrt{\frac{2H}{g}}$. Central panel: Wigner function $w(z, p_z)$, left panel: probability density in coordinate space $\psi(z)$, bottom panel: probability density in momentum space $\widetilde{\psi}(p_z)$. [73]

By combining the two components, the expressions of the wave function and intensity

at time t are:

$$\Psi_t(x,z) = \phi_t(x)\ \psi_t(z)\ , \tag{A.8}$$

$$I(x,z,t) = |\Psi_t(x,z)|^2 = |\phi_t(x)|^2\ |\psi_t(z)|^2 \tag{A.9}$$

$$= \frac{1}{2\pi\,(\zeta^2 + (\Delta v\ t)^2)} \exp\left(-\frac{(x-\overline{x}_0)^2 + (z-\overline{z}_0 + gt^2/2)^2}{2\,(\zeta^2 + (\Delta v\ t)^2)}\right).$$

The evolution of the wave-function or equivalently the intensity for the z component is illustrated in figure 3. The wave paquet spreads along the propagation and has after time t a dispersion of:

$$\zeta(t) = \sqrt{\zeta^2 + (\Delta v\ t)^2}. \tag{A.10}$$

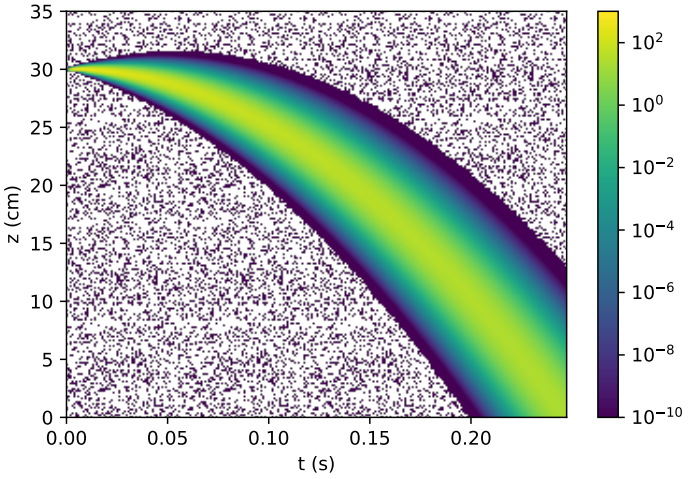

Figure 3: Illustration of the evolution of the intensity $|\psi_t(z)|^2$ (log scale) in space and time for initial position dispersion $\zeta = 0.5$ μm, null initial average velocity and free fall height $H = 30$ cm.

The current on a horizontal plate can be calculated from the wave function Ψ:

$$J(x,z,t) = \frac{i\hbar}{2m}\left[\Psi_t(x,z)\nabla\Psi_t^*(x,z) - \Psi_t^*(x,z)\nabla\Psi_t(x,z)\right] \tag{A.11}$$

$$= \frac{i\hbar}{2m}\left[\Psi_t(x,z)\left(\frac{\partial\Psi_t^*(x,z)}{\partial x} + \frac{\partial\Psi_t^*(x,z)}{\partial z}\right) - \Psi_t^*(x,z)\left(\frac{\partial\Psi_t(x,z)}{\partial x} + \frac{\partial\Psi_t(x,z)}{\partial z}\right)\right].$$

B Quantum reflection on a material surface

We detail here theoretical considerations concerning quantum reflection on Casimir-Polder potential. Those theoretical problems have been studied and developped in the thesis of G. Dufour [14] and P.P. Crépin [73], and we present here the main formulas.

In the wave mechanics description, a wave packet may split into both propagating and counter-propagating components. This phenomenon, when occurring for matter waves, may therefore predict non-zero reflection probability for particles. It is this departure from the classical particle picture which we call quantum reflection [5, 128].

We will present here briefly how the Casimir force works, and more details can be found in [158]. Casimir force is an attractive force between two parallel mirrors in vacuum, with intensity [159]:

$$F = \frac{\hbar c \pi^2 A}{240 r^4} \tag{B.12}$$

with r the distance between the plates and A their area. This force can be seen as a radiation pressure associated with the thermal and quantum fluctuations of the electromagnetic field [160]. It constitutes macroscopic evidence of the predictions of quantum field theory. We consider two objects at rest in vacuum, whose interaction with the electromagnetic field is described by the reflection operator $\mathcal{R}$ which gives the field $\vec{\mathcal{E}}_{\text{refl}}$ reflected by the object for a given incident field $\vec{\mathcal{E}}_{\text{in}}$:

$$\vec{\mathcal{E}}_{\text{refl}} = \mathcal{R}\vec{\mathcal{E}}_{\text{in}} \tag{B.13}$$

The presence of two objects induces a shift in the energy of the electromagnetic field compared with the situation where they are infinitely far apart. The energy difference induces a force, called the Casimir force, as illustrated by the figure below:

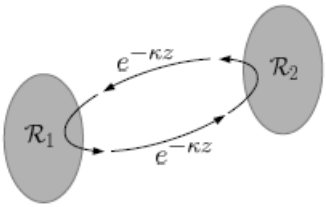

Figure 4: Casimir force - representation of a round trip of the field between two objects separated by a distance z and described by reflection operators $\mathcal{R}_1$ and $\mathcal{R}_2$.

We consider the case of Casimir interaction between an atom and a plane matter surface. It's called the Casimir-Polder force [161]. We note z the height of the atom above the surface, as it is represented in figure 5.

The approximative expression of the Casimir-Polder potential is [13]:

$$V_{cp}(z) \approx \frac{\hbar}{c^2} \int_0^{+\infty} \frac{d\xi}{2\pi} \xi^2 \alpha(i\xi) \int \frac{d^2\vec{k}_\perp}{(2\pi)^2} \frac{e^{-2K_z z}}{2K_z} \sum_p s_p r_p. \tag{B.14}$$

where $\alpha(i\xi)$ is the dynamic polarizability of the atom, p indices the field polarization and $K_z = \sqrt{\vec{k}_\perp^2 + \xi^2/c^2}$. In Casimir-Polder interaction, the atom and the surface interact through the electromagnetic field modified by their presence.

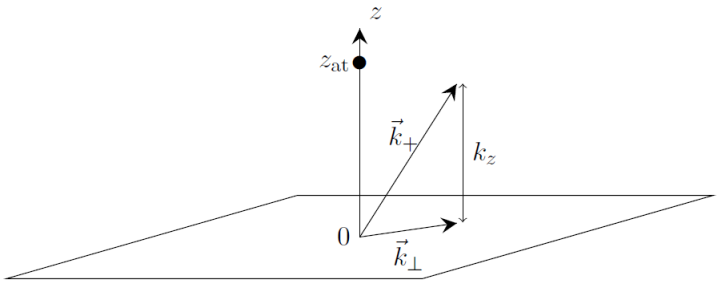

Figure 5: Representation of an atom at height z above a plane surface. The wavevector $\vec{k}$ is decomposed along its transverse $\vec{k}_\perp$ and longitudinal k_z components.

The mirror can be made with different materials : helium, silicon, silica, gold,... The quantum reflection probability in the low energy limit is given by [13]:

$$|r(k)|^2 \approx e^{4k\mathrm{Im}(a)} \tag{B.15}$$

with k the wave vector and a the scattering length. The scattering length a is a complex number which characterizes absorptive (reflective) properties of a material wall in the limit of low energy atom scattering. Scattering properties of the material wall are important ingredients in precision studies of gravitational properties of atoms, localized in Gravitational Quantum States above the material surface [9, 125, 162]. We present in the table 4 the value of the scattering length a for different materials, in Bohr radius unit ($a_0 \approx 5.29 \cdot 10^{-11}$ m) [73]:

Material	$\boldsymbol{a\ [a_0]}$
Perfectly reflective	$-53.5 - 554i$
Silicon	$-97.8 - 436i$
Silica	$-77.8 - 273i$
Gold	$-150.9 - 459.9i$
Liquid ^{3}He	$-30.1 - 35.4i$
Liquid ^{4}He	$-35.0 - 44.8i$

Table 4: Scattering length a in atomic units corresponding to the scattering of antihydrogen atom above different bulks [73].

In agreement with figure 6, the smallest values of $b \equiv |Im(a)|$ correspond to better reflectivity. Moreover, larger quantum reflection probability is obtained for weaker Casimir-Polder potentials.

The imaginary part of the scattering length also determines the mean lifetime τ for atoms bouncing above the bulk [24]:

$$\tau = \frac{\hbar}{2mgb}. \tag{B.16}$$

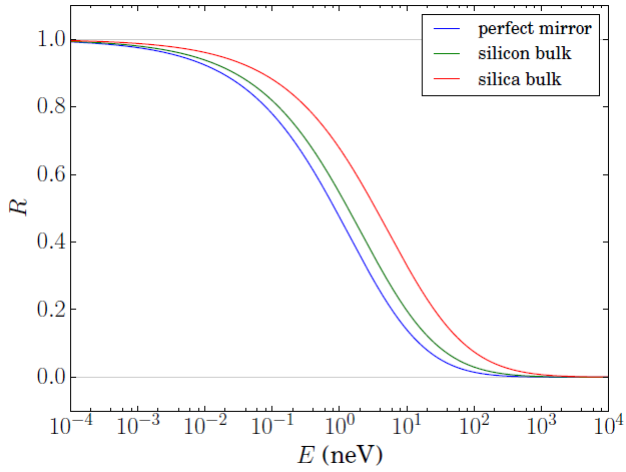

Figure 6: Quantum reflection probability $R = |r|^2$ as function of energy of the atom $E = mgh$, for different materials: perfect mirror ($b \approx 544$), silicon ($b \approx 436$) and silica ($b \approx 273$) [14].

In table 5, we compare the values obtained for τ for different material surfaces. In a classical picture, the bouncing period for an atom prepared at height $h = 10$ μm is

$$t_b = 2\sqrt{\frac{2h}{g}} \approx 2.85 \text{ ms}. \tag{B.17}$$

We give in table 5 the values of the number of bounces, expressed as function of t_b:

$$N_b = \frac{\tau}{t_b}. \tag{B.18}$$

Material	$\boldsymbol{\tau}$ **[s]**	$\boldsymbol{N_b}$
Perfectly reflective	0.11	38
Silicon	0.14	48
Silica	0.22	77
Gold	0.13	46
Liquid ^{3}He	1.35	474
Liquid ^{4}He	1.71	600

Table 5: Lifetime τ above various material surfaces and number N_b of bounces for hydrogen/antihydrogen atom in the first GQS for different materials.

The numbers show that liquid helium is a much better reflector for hydrogen/antihydrogen matter waves than the other materials. The much larger lifetime, that is also

the much larger number of bounces before annihilation, implies that it should be possible to trap hydrogen/antihydrogen atoms for long enough to improve significantly the spectroscopy measurements, or to produce interferences between Gravitational Quantum States.

With the Casimir-Polder potential, the total potential becomes:

$$V(z) = mgz + V_{cp}(z) \tag{B.19}$$

We represent in figure 7 this total potential V as function of z.

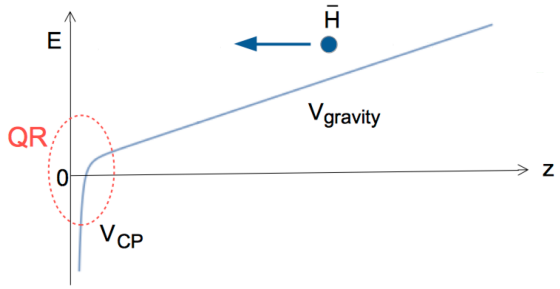

Figure 7: Representation of gravity and Casimir-Polder potentials $V(z) = mgz + V_{cp}(z)$.

The evolution of the wave function in presence of the gravity and CP potentials is governed by the equation

$$i\hbar\frac{\partial\psi}{\partial t} = \left(-\frac{\hbar^2}{2m}\Delta + V\right)\psi = \left[-\frac{\hbar^2}{2m}\left(\frac{\partial^2}{\partial x^2} + \frac{\partial^2}{\partial z^2}\right) + mgz + V_{cp}(z)\right]\psi. \tag{B.20}$$

These equations have been studied in particular in the thesis of G. Dufour [14] and P.P. Crepin [73].

C Details of algorithms and numerical computations

In this part, we detail how the calculations have been performed numerically.

Algorithms for the analysis processes

We first detail in figures 8 and 9 the algorithms used for the MC-likelihood analysis and Cramer-Rao estimation. It's a sum up for what we detailed in the part I particularly.

Programming languages and functions used

We used the programming language `Python 3` for main of the calculations [163, 164, 165], and occasionally `Mathematica` for simple calculations [166].

The following Python functions/modules were used [163, 167]:

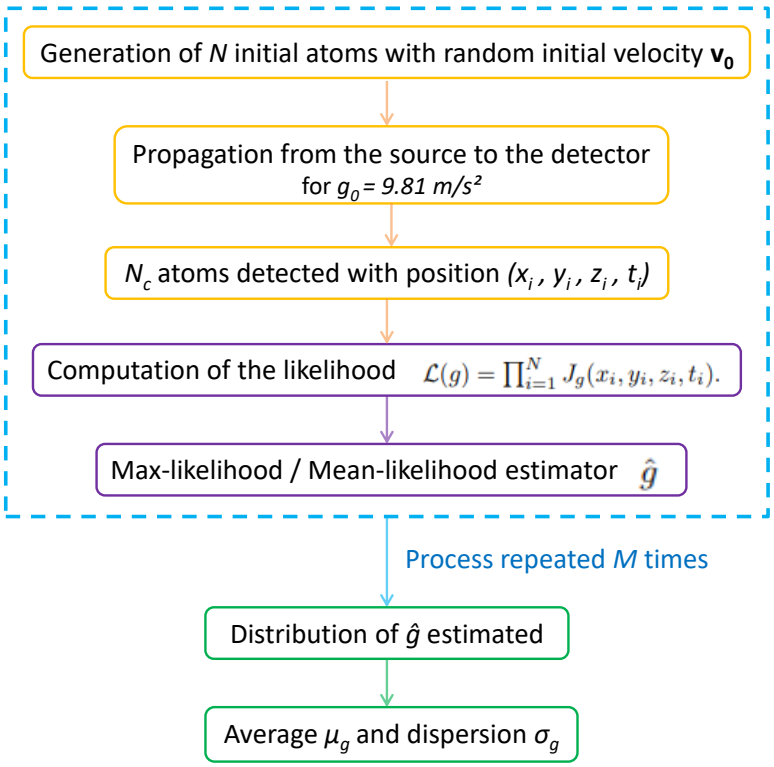

Figure 8: Details of the algorithm used for the Monte-Carlo likelihood analysis: Monte-Carlo generation of events (in orange), likelihood and estimator computation (in purple) and evaluation of the dispersion (in green).

- Fourier transform ⟶ `numpy.fft.fft()` ;
- Inverse Fourier transform ⟶ `numpy.fft.ifft()` ;
- Integral ⟶ `scipy.integrate.quad()` or `scipy.integrate.simps()` ;
- Derivative ⟶ `scipy.misc.derivative()` ;
- Find roots of a polynomial ⟶ `numpy.roots()` ;
- Airy function ⟶ `scipy.special.airy()` ;
- Random number in [0,1[uniform distribution ⟶ `numpy.random.rand()` ;
- Graph in 1D ⟶ `matplotlib.pyplot.plot()`
- Graph in 2D ⟶ `matplotlib.pyplot.imshow()`

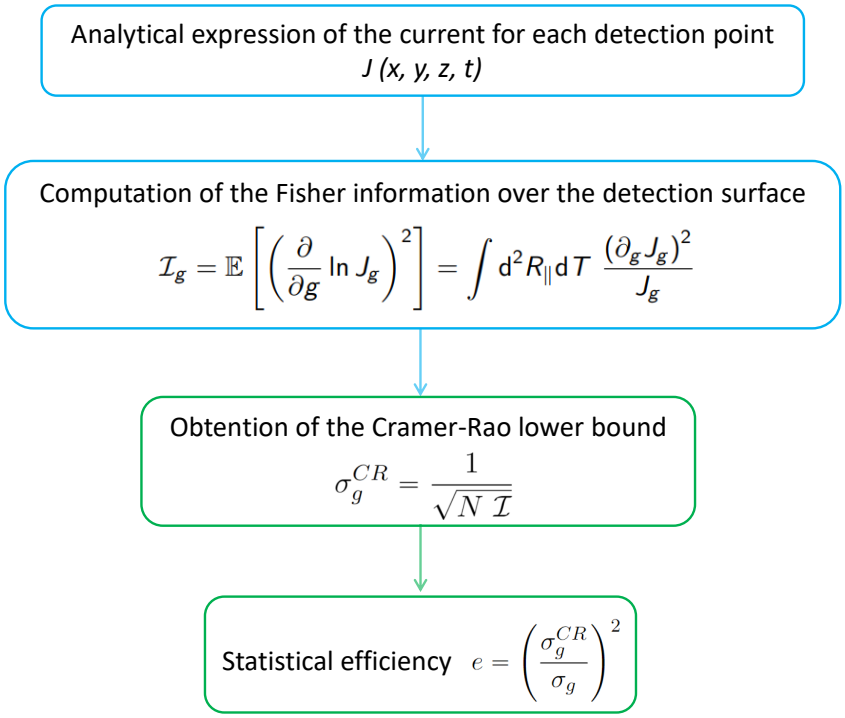

Figure 9: Details of the algorithm used for the Cramer-Rao analysis: computation of the current and Fisher information (in blue) and evaluation of the dispersion (in green).

Examples of code

We present below different examples of code which are important to compute the main functions of our program. The comments in the code are indicated with #. The following Python modules are used:

```
import numpy as np
from scipy.integrate import simps # Simpson integral
from scipy import integrate.nquad # Multiple continuous
    integral
import scipy.constants as cst # Physical constants
from scipy.special import * # For Airy function
```

Moreover, the following physical constants and parameters are used for the classical and the quantum cases.

```
g0 = 9.81 # Standard value of g
m_u = 1.660e-27
m = 1.00784*m_u # Mass of antihydrogen
```

```
hbar = cst.h/(2*np.pi) # Reduced Planck constant
lg = (hbar**2/(2*m**2*g0))**(1/3) # Length quantum scale
θn = np.pi/2 # Horizontal polarization of the laser
δE = 10 # in micro-eV
ve = np.sqrt(2*δE/m) # Photodetachment velocity recoil
ζ = 0.5e-6 # Position dispersion
Δv = hbar/(2*m*zeta) # Initial velocity dispersion (in m/s)
τ = np.sqrt(2*H/g0) # Classical free fall time
Δx = Δv*tau # Position dispersion after the free fall
N = 1000 # Number of initial atoms
λ = -ai_zeros(10000)[0] # Zeros of Airy function
d = 5e-2 # Mirror radius
```

For example, the code to generate the photodetachment recoil velocity $\boldsymbol{v}_e$ (I.50) and total initial velocity $\boldsymbol{v}_0$ (I.3) in Monte-Carlo is, by noting N the number of initial atoms:

```

def photodetachment-recoil_MC(N):
    θe = np.arccos(np.cbrt((1-2*np.random.rand(N))))
    φe = 2*np.pi*np.random.rand(N)
    return (ve*np.sin(θe)*np.cos(φe), ve*(np.cos(θn)*np.sin(θe
        )*np.sin(φe)-np.sin(θn)*np.cos(θe)),  ve*(np.sin(θn)*np
        .sin(θe)*np.sin(φe)+np.cos(θn)*np.cos(θe)))

def initial-velocity_MC(N):
    ve_x,ve_y,ve_z = photodetachment-recoil_MC(N)
    v0x = np.random.normal(size=N)*Δv - ve_x
    v0y = np.random.normal(size=N)*Δv - ve_y
    v0z = np.random.normal(size=N)*Δv - ve_z
    return (v0x,v0y,v0z)
```

After having generated MC events, the code to compute the likelihoods, the max-likelihood / mean-likelihood estimators and then the relative uncertainty is:

```

def get_likelihood(X,Y,Z,T,g):
    like = J(X,Y,Z,T,g) # Array of the values of J for the
        different detection points
    like[like<=0.] = 1e-100 # We attribute minimal value for
        J
    res = np.sum(np.log(like)) # Log likelihood
    return np.exp(res) # Likelihood

```

```
Tg = np.linspace(-0.01, 0.01, 1000)*g0+g0 # Range of the
    values of g considered

M = 10000 # Number of random draws
out = []
for i in range(M):
    X, Y, Z, T = MC.generate_time_position(N) # Detection
        events (X,Y,Z,T) generated with MC simulation
    Tlike = np.array([get_likelihood(X, Y, Z, T, g) for g in
        Tg]) # Likelihoods for the different values of g
    ghat_max = Tg[np.argmax(Tlike)] # Max likelihood
        estimator
    ghat_mean = simps(like*Tg, Tg) # Mean likelihood
        estimator
    out.append(ghat_max)
out = np.array(out)
bias = (out.mean()-g0)/g0 # Bias
sigma = abs(out.std()/g0) # Monte-Carlo dispersion
```

Now the computation of the Fisher information $\mathcal{I} = \int\int\int dXdYdT \, \frac{(\partial_g J_g(X,Y,T))^2}{J_g(X,Y,T)}$ is computed by using the module `nquad`:

```
def dJ(x,y,z,t,g): # Derivative of the current J
    dg=g/100000
    return (J(x,y,z,t,g+dg)-J(x,y,z,t,g-dg))/(2*dg)

def fisher_integrand(x,y,z,t,g): # Integrand
    if J(x,y,z,t,g)!=0:
        return dJ(x,y,z,t,g)**2/J(x,y,z,t,g)
    else:
        return 0

I = nquad(lambda x,y,t: fisher_integrand(x,y,-H,t,g), [[Xmin,
    Xmax],[Ymin, Ymax],[Tmin,Tmax]])[0] # Fisher information
sigma = 1/np.sqrt(N*I)/g0 # Cramer-Rao dispersion
```

In quantum design, the code to compute the eigenfunction $\chi_n = \Theta(z)\frac{Ai(z/l_g-\lambda_n)}{\sqrt{l_g}Ai'(-\lambda_n)}$ and the coefficients $c_n(q_z)$ is:

```
def χ(z,n):
    if z>=0:
        return airy(z/lg-λ[n])[0]/(np.sqrt(lg)*airy(-λ[n])
            [1])
```

```
    else:
        return 0

def c(n,qz):
    h2 = h + 2*1j*qz*ζ**2/hbar
    return (8*np.pi*ζ**2)**(1/4)/(np.sqrt(lg)*airy(-λ[n])[1])
       *airy(h2/lg-λ[n]+(ζ/lg)**4)[0]*np.exp((ζ/lg)**2*(h2/lg-
       λ[n]+2/3*(zeta/lg)**4)-(qz*ζ/hbar)**2)
```

In the quantum case, the statistical analysis in the quantum case is performed by fixing $x = 0$ for simplicity. The N_c detection events are generated randomly from the expression of the quantum current J corresponding to the value $g_0 = 9.81\ \mathrm{m/s^2}$. The max-likelihood method is used to compute the estimator.

```
Y = np.linspace((d+ve*τ)-5*Delta_x, (d+ve*τ)+5*Delta_x, 600)
T = np.linspace((d/ve+τ)*0.9, (d/ve+τ)*1.1, 600)

Jg0 = np.array([J(0,y,-H,t,g0) for y in Y for t in T]) #
   Table of the values of the current J for the different
   detection points, for g=g0
Jg0 = Jg0/np.sum(Jg0) # Normalization

gTable = np.linspace(-3e-5, 3e-5, 300)*g0+g0 # Values of g
   evaluated
JgTable = [[J(0,y,-H,t,g) for y in Y for t in T] for g in
   gTable] # Table of the values of the current J for the
   different detection points, for the different values of g
JgTable = [element/np.sum(element) for element in JgTable] #
   Normalization

M = 10000 # Number of random draws
Sample = np.array([np.random.choice(len(Y)*len(T), Nc, p=list
   (Jg0)) for i in range(M)]) # Sample of Nc atoms among the
   detection points for g=g0, ponderated by the weights of
   the list Jg0.
out = np.array([gTable[np.argmax([np.sum(np.log(jg[sample]))
   for jg in JgTable])] for sample in Sample]) # List of the
   values of g estimated with max-likelihood
bias = (out.mean()-g0)/g0 # Bias
sigma = abs(out.std()/g0) # Relative uncertainty
```

Acceleration of the simulations

In `Python`, the calculations of loops were accelerated by using the module `Numba` (Python high performance JIT compiler) [168, 169]. More precisely, `Numba` translates Python functions to optimized machine code at runtime using the LLVM compiler library. Numba-compiled numerical algorithms in Python can approach the speeds of the language C. `Numba` can be used by simply applying the `numba.njit` decorator to a Python function that does numerical computations [170]:

```
import numba
@numba.njit() # Numba decorator
def function(...):
    for i in range(...): # Loop
        ...
    return ...
```

Moreover, such process can be parallelized on CPUs by the following way:

```
import numba
@numba.njit(parallel=True) # Numba decorator with
   parallelization
def function(...):
    for i in numba.prange(...):
        ...
    return ...
```

For example, the code to compute the wave function at the end of the mirror $\psi_d(z, q_z, t) = \sum_n c_n(q_z)\chi_n e^{-i\varphi_n(t)}$ is:

```
GQS = 1000
@numba.njit(parallel=True)
def ψd(z,qz,t):
    A = 0
    for n in numba.prange(GQS):
        A += c(n,qz)*χ(z,n)*np.exp(-1j*λ[n]*t/tg) # Sum over
           GQS
    return A
```

Duration of the simulations

The simulations were performed on the servers at LKB managed by Dominique Delande. We used `Numba` and parallelization to increase the speed of the simulations. We analyse here the duration of the simulation for the analysis process in the quantum design case, for $n_{\max} = 1000$. The Cramer-Rao analysis process takes about 1 day by using a server with 24 cores, while the Monte-Carlo generation of events and max-likelihood estimation takes about 13 days (then about 13 times longer). Of course, the duration of the quantum

simulation increases when we simulate more GQS. Finally, we mention that the simulation of the quantum design takes about 100 times longer than the classical design.

Index of notations

Acronyms and symbols

- H hydrogen atom ; $\bar{H}$ antihydrogen atom
- p proton ; antiproton $\bar{p}$
- e^- electron ; e^+ positron
- P_s positronium
- GBAR: *Gravitational Behaviour of Antihydrogen at Rest*
- GRASIAN: *GRAvity, Spectroscopy and Interferometry with ultra-cold Atoms and Neutrons*

Physical constants

- Plank constant $h \approx 6.62 \cdot 10^{34}$ J.s
- Reduced Plank constant $\hbar \approx 1.05 \cdot 10^{34}$ J.s
- Speed of light $c \approx 2.998 \cdot 10^{8}$ m/s
- Bohr radius $a_0 \approx 5.29 \cdot 10^{-11}$ m

Wave packet characteristics and evolution

- $\Psi_t(\boldsymbol{r})$ time dependant wave function
- $\widetilde{\Psi}_t(\boldsymbol{p})$ wave function in momentum space
- λ_{dB} De Broglie wavelength
- ζ dispersion of positions
- Δv dispersion of velocity

- $\rho(\boldsymbol{r}, \boldsymbol{r})$ density matrix
- $W(\boldsymbol{r}, \boldsymbol{p})$ Wigner function
- $\Pi(\boldsymbol{p})$ momentum distribution

Photodetachment process

- θ_n polarization angle
- δE photodetachment energy above the threshold
- v_e/q_e photodetachment recoil velocity/momentum
- (θ_e, φ_e) photodetachment spherical angles
- ϖ angular distribution probability due to photodetachement
- Ω solid angle
- q total momentum transfer

Classical timing of the free fall

- $m \approx 1.67 \cdot 10^{-27}$ kg mass of antihydrogen atom
- $g_0 = 9.81$ m/s^2 gravity field on earth
- $\overline{g}$ gravity acceleration of antimatter on earth. We use $\overline{g} = g_0$ for all numerical estimations.
- N initial number of antiatoms
- N_c number of atoms detected
- t_0 initial time
- $v_{x_0}, v_{y_0}, v_{z_0}$ initial velocity
- f trap frequency (with $\omega = 2\pi f$)
- H free fall height
- R_c radius of the chamber
- H_d height between the trap and disks
- R_d radius of the disks
- t free fall time

- t_c critical time
- δ_τ logistic distribution taking into account uncertainty on initial time t_0
- x, y, z detection positions
- $v_\perp$ velocity orthogonal to detection surface

Quantum measurement

- l_g /ϵ_g / p_g / t_g typical scales (length/energy/momentum/time) for the GQS
- V_{cp} Casimir-Polder potential
- Ai Airy function
- $(-\lambda_n)$ zeros of the Airy function
- χ_n wave functions of the GQS
- c_n amplitudes associated to the GQS
- Θ Heavide function
- h average initial height above the mirror
- d length of the reflecting mirror
- x, y, z position at the end of the mirror
- v_x, v_y, v_z velocity at the end of the mirror
- τ free fall time
- $T = t + \tau$ total time
- X, Y, Z detection position
- $V_\perp$ velocity orthogonal to detection surface

Statistics

- J probability density current
- $\mathbb{E}$ expected value
- $\mathcal{I}$ Fisher information
- $\mathcal{L}$ likelihood function

- $\widehat{g}$ estimator of g
- σ_g^{CR} standard deviation of the estimators obtained with Cramer-Rao method
- σ_g^{MC} standard deviation of the estimators obtained with Monte-Carlo method
- e statistical efficiency

List of publications

Articles in peer-reviewed journals

O. Rousselle, P. Cladé, S. Guellati, R. Guérout and S. Reynaud, *Analysis of the timing of freely falling antihydrogen*, New Journal of Physics 24, 033045, 2022.
Abstract: We evaluate the accuracy to be expected for the measurement of free fall acceleration of antihydrogen in the GBAR experiment, accounting for the recoil transferred in the photodetachment process. We show that the uncertainty on the measurement of gravity comes mainly from the initial velocity dispersion in the ion trap so that the photodetachment recoil is not the limiting factor to the precision as a naive analysis would suggest. This result will ease the constraints on the choice of the photodetachment laser parameters.

O. Rousselle, P. Cladé, S. Guellati, R. Guérout and S. Reynaud, *Improving the statistical analysis of anti-hydrogen free fall by using near edge events*, Physical Review A 105, 022821, 2022.
Abstract: An accurate evaluation of the gravity acceleration from the timing of free fall of antihydrogen atoms in the Gravitational Behaviour of Anti-hydrogen at Rest (GBAR) experiment requires one to account for obstacles surrounding the antimatter source. These obstacles reduce the number of useful events but may improve accuracy since the edges of the shadows of obstacles on the detection chamber depend on gravity, bringing additional information about the value of g. We perform Monte Carlo simulations to obtain the dispersion and give a qualitative understanding of the results by analyzing the statistics of events close to an edge. We also study the effect of specular quantum reflections of antihydrogen on surfaces and show that they do not degrade the accuracy that much.

O. Rousselle, P. Cladé, S. Guellati, R. Guérout and S. Reynaud, *Quantum interference measurement of the free fall of anti-hydrogen*, To be submitted in The European Physical Journal D, arXiv:2204.10778, 2022
Abstract: We analyze a quantum measurement designed to improve the accuracy for the free-fall acceleration of anti-hydrogen in the GBAR experiment. Including the effect of photo-detachment recoil in the analysis and developing a full quantum analysis of anti-matter wave propagation, we show that the accuracy is improved by approximately three orders of magnitude with respect to the classical timing technique planned for the

current experiment.

D. Arruga, O. Rousselle and O. Minazzoli, Compact Objects in Entangled Relativity, Physical Review D 103, 024034, 2021.
Abstract: We describe the first numerical Tolman-Oppenheimer-Volkoff solutions of compact objects in entangled relativity, which is an alternative to the framework of general relativity that does not have any additional free parameter. Assuming a simple polytropic equation of state and the conservation of the rest-mass density, we notably show that, for any given density, compact objects are always heavier (up to 8%) in entangled relativity than in general relativity – for any given central density within the usual range of neutron stars' central densities, or for a given radius of the resulting compact object.

Articles of the GBAR collaboration in peer-reviewed journals

A. Husson and GBAR collaboration, *A pulsed high-voltage decelerator system to deliver low-energy antiprotons*, Nuclear Instruments and Methods in Physics Research Section A 1002, 165245, 2021.
Abstract: The GBAR (Gravitational Behaviour of Antihydrogen at Rest) experiment at CERN requires efficient deceleration of 100 keV antiprotons provided by the new ELENA synchrotron ring to synthesize antihydrogen. This is accomplished using electrostatic deceleration optics and a drift tube that is designed to switch from 99 kV to ground when the antiproton bunch is inside - essentially a charged-particle "elevator" - producing a 1 keV pulse. We describe the simulation, design, construction and successful testing of the decelerator device at 92 kV on-line with ELENA.

M. Charlton and GBAR collaboration, *Positron production using a 9 MeV electron linac for the GBAR experiment*, Nuclear Instruments and Methods in Physics Research Section A 985, 164657, 2021.
Abstract: For the GBAR (Gravitational Behaviour of Antihydrogen at Rest) experiment at CERN's Antiproton Decelerator (AD) facility we have constructed a source of slow positrons, which uses a low-energy electron linear accelerator (linac). The driver linac produces electrons of 9 MeV kinetic energy that create positrons from bremsstrahlung-induced pair production. Staying below 10 MeV ensures no persistent radioactive activation in the target zone and that the radiation level outside the biological shield is safe for public access. An annealed tungsten-mesh assembly placed directly behind the target acts as a positron moderator. The system produces 5×10^7 slow positrons per second, a performance demonstrating that a low-energy electron linac is a superior choice over positron-emitting radioactive sources for high positron flux.

Articles in peer-reviewed conference proceedings

O. Rousselle and S. Reynaud, *Analysis of measurements of free fall acceleration of antihydrogen in the GBAR experiment*, Proceedings of the 56^{th} Rencontres de Moriond

2022, ARISF.
Abstract: An accurate evaluation of the gravity acceleration $\bar{g}$ from the timing of free fall of anti-hydrogen $\bar{H}$ atoms in the GBAR experiment requires to take into account obstacles surrounding the anti-matter source. These obstacles reduce the number of useful events but may improve accuracy since the edges of the shadow of obstacles on the detection chamber depends on gravity, bringing additional information on the value of $\bar{g}$. We perform Monte Carlo simulations to obtain the dispersion and give a qualitative understanding of the results by analysing the statistics of events close to an edge. We also take into account the effect of specular quantum reflection of $\bar{H}$ atoms on detection surfaces.

O. Rousselle, P. Cladé, S. Guellati, R. Guérout and S. Reynaud, *Does antimatter fall like matter?: simulation of the GBAR experiment*, Andromeda proceedings, BSM 2021.
Abstract: One of the main questions of fundamental physics is the action of gravity on antimatter. We present here the simulation of the last part of the experiment GBAR at CERN, i.e. the measurement of the free fall acceleration $\bar{g}$ of antihydrogen atoms in the gravitational field of the Earth. It includes the Monte-Carlo generation of trajectories and the analysis leading to the estimation of $\bar{g}$. A precision of the measurement beyond the % level is confirmed when taking into account the experimental design.

O. Rousselle and T. Sykora, *Fast simulation of Time-of-Flight detectors at the LHC*, EPJ Web of Conferences 251, 03027, CHEP 2021.
Abstract: The modelling of Cherenkov based detectors is traditionally done using Geant4 toolkit. In this work, we present another method based on Python programming language and Numba high performance compiler to speed up the simulation. As an example we take one of the Forward Proton Detectors at the CERN LHC - ATLAS Forward Proton (AFP) Time-of-Flight, which is used to reduce the background from multiple proton-proton collisions in soft and hard diffractive events. We describe the technical details of the fast Cherenkov model of photon generation and transportation through the optical part of the ToF detector. The fast simulation is revealed to be about 200 times faster than the corresponding Geant4 simulation, and provides similar results concerning length and time distributions of photons. The study is meant as the first step in a construction of a building kit allowing creation of a fast simulation of an arbitrary shaped optical part of detectors.

Bibliography

[1] L. de Broglie. Recherches sur la théorie des quanta. *thèse Université de Paris*, 1924.

[2] C.J. Davisson and L.H. Germer. Reflection of electrons by a crystal of nickel. *Proceedings of the National Academy of Sciences of the United States of America*, 14:317–322, 1928.

[3] E. Schrödinger. Quantisierung als eigenwertproblem. *Annalen der Physik*, 384:361–376, 1926.

[4] W. Heisenberg. Über den anschaulichen inhalt der quantentheoretischen kinematik und mechanik. *Zeitschrift für Physik*, 43:172–198, 1927.

[5] M.V. Berry and Mount K.E. Semiclassical approximations in wave mechanics. *Reports on Progress in Physics*, 35:315, 1972.

[6] L. Brekhovskikh. *Waves in layered media*. Elsevier, 2012.

[7] J.E. Lennard-Jones and A.F. Devonshire. The interaction of atoms and molecules with solid surfaces. iii. the condensation and evaporation of atoms and molecules. *Proceedings of the Royal Society of London A*, 156:6–28, 1936.

[8] J.E. Lennard-Jones and A.F. Devonshire. The interaction of atoms and molecules with solid surfaces. iv. the condensation and evaporation of atoms and molecules. *Proceedings of the Royal Society of London A*, 156:29–36, 1936.

[9] I.A. Yu, J.M. Doyle, J.C. Sandberg, C.L. Cesar, D Kleppner, and T.J. Greytak. Evidence for universal quantum reflection of hydrogen from liquid ^{4}He. *Physical Review Letters*, 71:1589–1592, 1993.

[10] H. Shimizu. Specular reflection of very slow metastable neon atoms from a solid surface. *Physical Review Letters*, 86:987–990, 2001.

[11] T.A. Pasquini, Y. Shin, C. Sanner, M. Saba, A. Schirotzek, D.E. Pritchard, and W. Ketterle. Quantum reflection from a solid surface at normal incidence. *Physical Review Letters*, 93:223201, 2004.

[12] T. A. Pasquini, M. Saba, G.-B. Jo, Y. Shin, W. Ketterle, D.E. Pritchard, T.A. Savas, and N. Mulders. Low velocity quantum reflection of Bose-Einstein condensates. *Physical Review Letters*, 97:093201, 2006.

[13] G. Dufour, A. Gérardin, R. Guérout, A. Lambrecht, V. V. Nesvizhevsky, S. Reynaud, and A. Yu. Voronin. Quantum reflection of antihydrogen from the Casimir potential above matter slabs. *Physical Review A*, 87:012901, 2013.

[14] G. Dufour. Quantum reflection from the Casimir-Polder potential. *thèse Sorbonne Université*, 2015.

[15] G. Breit. The propagation of Schrödinger waves in a uniform field of force. *Physical Review*, 32:273–276, 1928.

[16] P.W. Langhoff. Schrödinger particle in a gravitational well. *American Journal of Physics*, 39:954, 1971.

[17] R.L. Gibbs. The quantum bouncer. *American Journal of Physics*, 43:25, 1975.

[18] J Gea-Banacloche. A quantum bouncing ball. *American Journal of Physics*, 67:776–782, 1999.

[19] V.V. Nesvizhevsky et al. Quantum states of neutrons in the Earth's gravitational field. *Nature*, 415:297–299, 2002.

[20] V.V. Nesvizhevsky et al. Measurement of quantum states of neutrons in the earth's gravitational field. *Physical Review D*, 67:102002, 2003.

[21] V.V. Nesvizhevsky et al. Study of the neutron quantum states in the gravity field. *European Physical Journal C*, 40:479–491, 2005.

[22] V.V. Nesvizhevsky and A.Yu. Voronin. *Surprising quantum bounces.* Imperial College Press, 2015.

[23] A.Yu Voronin and P. Froelich. Quantum reflection of ultracold antihydrogen from a solid surface. *Journal of Physics B*, 38:L301, 2005.

[24] P.-P. Crépin, G. Dufour, R. Guérout, A. Lambrecht, and S. Reynaud. Casimir-Polder shifts on quantum levitation states. *Physical Review A*, 95:032501, 2017.

[25] L. Viola and R. Onofrio. Testing the equivalence principle through freely falling quantum objects. *Physical Review D*, 55:455, 1997.

[26] A. Herdegen and J. Wawrzycki. Is Einstein's equivalence principle valid for a quantum particle? *Physical Review D*, 66:044007, 2002.

[27] M.M. Ali, A.S. Majumdar, D. Home, and A.K. Pan. On the quantum analogue of Galileo's leaning tower experiment. *Classical and Quantum Gravity*, 23:6493–6502, 2006.

[28] E. Kajari, N.L. Harshman, E.M. Rasel, S. Stenholm, G. Süßmann, and W.P. Schleich. Inertial and gravitational mass in quantum mechanics. *Applied Physics B*, 100:43–60, 2010.

[29] R. Colella, A.W. Overhauser, and S.A. Werner. Observation of gravitationally induced quantum interference. *Physical Review Letters*, 34:1472.

[30] M. Kasevich and S. Chu. Atomic interferometry using stimulated Raman transitions. *Physical Review Letters*, 67:181, 1991.

[31] M. Jammer. *Concepts of Mass in Contemporary Physics and Philosophy*. Princeton University Press, 2000.

[32] S. Fray, C.A. Diez, T.W. Hänsch, and M. Weitz. Atomic interferometer with amplitude gratings of light and its applications to atom based tests of the equivalence principle. *Physical Review Letters*, 93:240404, 2004.

[33] T.A. Wagner, S. Schlamminger, J.H. Gundlach, and E.G. Adelberger. Torsion-balance tests of the weak equivalence principle. *Classical and Quantum Gravity*, 29(18):184002, 2012.

[34] C.C. Speake and C.M. Will. Tests of the weak equivalence principle. *Classical and Quantum Gravity*, 29:180301, 2012.

[35] D. Schlippert, J. Hartwig, H. Albers, L.L. Richardson, C. Schubert, A. Roura, W.P. Schleich, W. Ertmer, and E.M. Rasel. Quantum test of the universality of free fall. *Physical Review Letters*, 112:203002, 2014.

[36] C.M. Will. *Theory and Experiment in Gravitational Physics (new edition)*. Cambridge University Press, 2018.

[37] V. Viswanathan, A. Fienga, O. Minazzoli, L. Bernus, J. Laskar, and M. Gastineau. The new lunar ephemeris INPOP17a and its application to fundamental physics. *Monthly Notices of the Royal Astronomical Society*, 476(2):1877–1888, 2018.

[38] P. Asenbaum, C. Overstreet, M. Kim, J. Curti, and M.A. Kasevich. Atom-interferometric test of the equivalence principle at the 10^{-12} level. *Physical Review Letters*, 125:191101, 2020.

[39] P. Touboul et al. MICROSCOPE mission: First results of a space test of the equivalence principle. *Physical Review Letters*, 119:231101, 2017.

[40] P.A.M. Dirac. The quantum theory of the electron. *Procedings of the Royal Society of London A: Mathematical, Physical and Engineering Sciences*, 1928.

[41] C.D. Anderson. The apparent existence of easily deflectable positives. *Science*, 76:238–239, 1932.

[42] G. Gabrielse, A. Khabbaz, D.S. Hall, C. Heimann, H. Kalinowsky, and W. Jhe. Precision mass spectroscopy of the antiproton and proton using simultaneously trapped particles. *Physical Review Letters*, 82:3198–3201, 1999.

[43] Y. Yamazaki and S. Ulmer. CPT symmetry tests with cold and antihydrogen. *Annalen der Physik*, 525(7):493–504, 2013.

[44] M.S. Safronova, D. Budker, D. DeMille, D.F.J. Kimball, A. Derevianko, and C.W. Clark. Search for new physics with atoms and molecules. *Review of Modern Physics*, 90:025008, 2018.

[45] D.J. Griffiths. *Introduction to elementary particles; 2nd rev. version.* Physics textbook. Wiley, New York, NY, 2008.

[46] J. Scherk. Antigravity: A crazy idea? *Physics Letters B*, 88:265–267, 1979.

[47] G. Chardin. Motivations for antigravity in general relativity. *Hyperfine Interactions*, 109:83–94, 1997.

[48] S. Hossenfelder. A bi-metric theory with exchange symmetry. *Physical Review D*, 78:044015, 2008.

[49] S.G. Karshenboim. A constraint on antigravity of antimatter from precision spectroscopy of simple atoms. *Astronomy Letters*, 35:663–669, 2009.

[50] M. Villata. CPT symmetry and antimatter gravity in general relativity. *EPL (Europhysics Letters)*, 94, 2011.

[51] J.M. Souriau. *Structure des Systèmes Dynamiques.* 1970.

[52] M. Morris, K. Thorne, and U. Yurtsever. Wormholes, time machines and the weak energy condition. *Physical Review*, 61:1446, 1988.

[53] S. Mbarek and M.B. Paranjape. Negative mass bubbles in de sitter spacetime. *Phys. Rev. D*, 90, 2014.

[54] G. Chardin and G. Manfredi. Gravity, antimatter and the Dirac-Milne universe. *Hyperfine Interactions*, 239:45, 2018.

[55] B. Guay. Dirac field of negative energy and primordial antimatter incursion. *International Journal of Modern Theoretical Physics*, 9:1–15, 2020.

[56] P. Morrison. Approximate nature of physical symmetries. *American Journal of Physics*, 26:358, 1958.

[57] M.M. Nieto and T. Goldman. The arguments against antigravity and the gravitational acceleration of antimatter. *Physics Reports*, 205(5):221–281, 1991.

[58] E.G. Adelberger, B.R. Heckel, C.W. Stubbs, and Y. Su. Does antimatter fall with the same acceleration as ordinary matter? *Physical Review Letters*, 66:850–853, 1991.

[59] F.C. Witteborn and W.M. Fairbank. Experimental comparison of the gravitational force on freely falling electrons and metallic electrons. *Physical Review Letters*, 19:1049, 1967.

[60] T.W. Darling, F. Rossi, G.I. Opat, and G.F. Moorhead. The fall of charged particles under gravity: A study of experimental problems. *Review of Modern Physics*, 64:237, 1992.

[61] M.H. Holzscheiter et al. Trapping of antiprotons in a large Penning trap - progress towards a measurement of the gravitational acceleration of the antiproton. *Nuclear Physics A*, 558:709–718, 1993.

[62] G. Baur et al. Production of antihydrogen. *Physics Letters B*, 368:251–258, 1996.

[63] M.H. Holzscheiter and M.M. Nieto. The route to ultra-low energy antihydrogen. *Physics Reports*, 402:1–101, 2004.

[64] G. Drobychev et al. Proposal for the AEGIS experiment at the CERN antiproton decelerator (Antimatter Experiment: Gravity, Interferometry, Spectroscopy). Technical Report CERN-SPSC-2007-017. SPSC-P-334, CERN, Geneva, 2007.

[65] AEGIS Collaboration and M.G. Giammarchi. AEGIS at CERN: Measuring antihydrogen fall. *Few-Body Systems*, 54, 2012.

[66] J.S. Hangst and P. Bowe. ALPHA Proposal. Technical Report CERN-SPSC-2005-006. SPSC-P-325, CERN, Geneva, 2005.

[67] Alpha Collaboration and A. E. Charman. Description and first application of a new technique to measure the gravitational mass of antihydrogen. *Nature Communications*, 4:1785, 2013.

[68] M.J. Borchert et al. A 16-parts-per-trillion measurement of the antiproton-to-proton charge-mass ratio. *Nature*, 601:53–57, 2022.

[69] J. Walz and T.W. Hänsch. A proposal to measure antimatter gravity using ultracold antihydrogen atoms. *General Relativity and Gravitation*, 36(3):561–570, 2004.

[70] P. Perez and GBAR Collaboration. The GBAR antimatter gravity experiment. *Hyperfine Interactions*, 233:21–27, 2015.

[71] B. Mansoulié and GBAR collaboration. Status of the GBAR experiment at CERN. *Hyperfine Interactions*, 240, 2019.

[72] G. Dufour, P. Debu, A. Lambrecht, V. V. Nesvizhevsky, S. Reynaud, and A. Yu. Voronin. Shaping the distribution of vertical velocities of antihydrogen in gbar. *The European Physical Journal C*, 74(1):2731–, 2014.

[73] P.P. Crépin. Quantum reflection of a cold antihydrogen wave packet. *thèse Sorbonne Université*, 2019.

[74] M. Hori and J. Walz. Physics at CERN's antiproton decelerator. *Progress in Particle and Nuclear Physics*, 72:206–253, 2013.

[75] W.A. Bertsche, E. Butler, M. Charlton, and N. Madsen. Physics with antihydrogen. *Journal of Physics B: Atomic, Molecular and Optical Physics*, 48(23):232001, 2015.

[76] M. Charlton, A.P. Mills, and Y. Yamazaki. Special issue on antihydrogen and positronium. *Journal of Physics B: Atomic, Molecular and Optical Physics*, 50(14):140201, 2017.

[77] Y. Yamazaki. Cold and stable antimatter for fundamental physics. *Proceedings of the Japan Academy, Series B*, 96(10):471–501, 2020.

[78] H. Bondi. Negative mass in general relativity. *Reviews of Modern Physics*, 29:423, 1957.

[79] F.M. Huber, R.A. Lewis, E.W. Messerschmid, and G.A. Smith. Precision tests of Einstein's weak equivalence principle for antimatter. *Advances in Space Research*, 25:1245–1249, 2000.

[80] S. Maury, W. Oelert, W. Bartmann, P. Belochitskii, H. Breuker, F. Butin, C. Carli, T. Eriksson, S. Pasinelli, and G. Tranquille. ELENA: the extra low energy antiproton facility at CERN. *Hyperfine Interactions*, 229(1):105–115, 2014.

[81] A. Kellerbauer et al. Proposed antimatter gravity measurement with an antihydrogen beam. *Nuclear Instruments and Methods in Physics Research B*, 266:351–356, 2008.

[82] W.A. Bertsche. Prospects for comparison of matter and antimatter gravitation with ALPHA-g. *Philosophical Transactions of the Royal Society A: Mathematical, Physical and Engineering Sciences*, 376(2116):20170265, 2018.

[83] D. Pagano et al. Gravity and antimatter: the AEGIS experiment at CERN. *Journal of Physics: Conference Series*, 1342:012016, 2020.

[84] P. Indelicato and GBAR Collaboration. The GBAR project, or how does antimatter fall? *Hyperfine Interactions*, 228:141–150, 2014.

[85] G. Tranquille, P. Belochitskii, T. Eriksson, S. Maury, and W. Oelert. ELENA: From the first ideas to the project. *Conference Proceedings C1205201*, 2012.

[86] W. Oelert. The ELENA project at CERN. *Acta Physica Polonica B*, 48, 2015.

[87] D. Lunney, C. Bachelet, C. Guénaut, S. Henry, and M. Sewtz. COLETTE: A linear paul-trap beam cooler for the on-line mass spectrometer MISTRAL. *Nuclear Instruments and Methods A*, 379, 2009.

[88] A. Husson and GBAR Collaboration. A pulsed high-voltage decelerator system to deliver low-energy antiprotons. *Nuclear Instruments and Methods in Physics Research A*, 1002:165245, 2021.

[89] M. Charlton and GBAR Collaboration. Positron production using a 9 mev electron linac for the GBAR experiment. *Nuclear Instruments and Methods in Physics Research A*, 985:164657, 2021.

[90] S. Niang and GBAR Collaboration. Accumulation of positrons from a linac based source. *Acta Physica Polonica A*, 137:164–166, 2020.

[91] L. Liszkay et al. Positronium reemission yield from mesostructured silica films. *Applied Physics Letters*, 92:063114, 2008.

[92] D.B. Cassidy, P. Crivelli, T.H. Hisakado, L. Liszkay, V.E. Meligne, P. Perez, H.W.K. Tom, and A.P. Mills. Positronium cooling in porous silica measured via doppler spectroscopy. *Physical Review A*, 81:012715, 2010.

[93] P. Crivelli, U. Gendotti, R. Rubbia, L. Liszkay, P. Pérez, and C. Corbel. Measurement of the orthopositronium confinement energy in mesoporous thin films. *Physical Review A*, 81:052703, 2010.

[94] Comini P. and P.-A. Hervieux. $\bar{H}^-$ ion production from collisions between antiprotons and excited positronium: cross sections calculations in the framework of the gbar experiment. *New Journal of Physics*, 15:095022, 2013.

[95] P. Comini, P.-A. Hervieux, and F. Biraben. $\bar{H}^+$ production from collisions between positronium and kev antiprotons for gbar. *Hyperfine Interactions*, 228:159, 2014.

[96] P. Crivelli, D.A. Cooke, and S. Friedreich. Experimental considerations for testing antimatter antigravity using positronium 1s-2s spectroscopy. *International Journal of Modern Physics: Conference Series*, 30, 2014.

[97] D.J. Larson, J.C. Bergquist, J.J. Bollinger, W.M. Itano, and D.J. Wineland. Sympathetic cooling of trapped ions: A laser-cooled two-species nonneutral ion plasma. *Physical Review Letters*, 57:70, 1986.

[98] H. Wallis, J. Dalibard, and C. Cohen-Tannoudji. Trapping atoms in a gravitational cavity. *Applied Physics B*, 54:407–419, 1992.

[99] L. Hilico, J.-P. Karr, A. Douillet, P. Indelicato, S. Wolf, and F. Schmidt-Kaler. Preparing single ultra-cold antihydrogen atoms for free-fall in GBAR. *International Journal of Modern Physics: Conference Series*, 30:1460269, 2014.

[100] N. Sillitoe, J.-P. Karr, J. Heinrich, T. Louvradoux, A. Douillet, and L. Hilico. $\overline{\mathrm{H}}^{+}$ *Sympathetic Cooling Simulations with a Variable Time Step*, volume 18 of *JPS Conference Proceedings*. 2017.

[101] GBAR collaboration page: https://gbar.web.cern.ch/.

[102] K.R. Lykke, K.K. Murray, and W.C. Lineberger. Threshold photodetachment of H^{-}. *Physical Review A*, 43:6104–6107, 1991.

[103] M. Vandevraye, P. Babilotte, C. Drag, and C. Blondel. Laser measurement of the photodetachment cross section of H^{-} at the wavelength 1064 nm. *Physical Review A*, 90:013411, 2014.

[104] D. Bresteau, C. Blondel, and C. Drag. Saturation of the photoneutralization of a H^{-} beam in continuous operation. *Review of Scientific Instruments*, 88(11):113103, 2017.

[105] D. Banerjee. Resistive multiplexed micromegas detectors to search for dark sector physics and test the weak equivalence principle for anti-matter at CERN. *PhD Sussex University*, 2017.

[106] Y. Giomataris, P. Rebourgeard, J.P. Robert, and G. Charpak. MICROMEGAS: a high-granularity position-sensitive gaseous detector for high particle-flux environments. *Nuclear Instruments and Methods in Physics Research Section A: Accelerators, Spectrometers, Detectors and Associated Equipment*, 376:29–35, 1996.

[107] B. Radics, G. Janka, D. A. Cooke, S. Procureur, and P. Crivelli. Double hit reconstruction in large area multiplexed detectors. *Review of Scientific Instruments*, 90(9):093305, 2019.

[108] O. Rousselle, P. Cladé, S. Guellati-Khelifa, R. Guérout, and S. Reynaud. Analysis of the timing of freely falling antihydrogen. *New Journal of Physics*, 24:033045, 2022.

[109] E. Wigner. On the quantum correction for thermodynamic equilibrium. *Physical Review*, 40:749–759, 1932.

[110] M.V. Berry. Semi-classical mechanics in phase space: A study of wigner's function. *Philosophical Transactions of the Royal Society of London. Series A, Mathematical and Physical Sciences*, 287, 1977.

[111] F.W.J. Olver et al. *NIST Handbool of Mathematical Functions*. 2010.

[112] F.W.J. Olver and L.C. Maximon. Digital library of mathematical functions. https://dlmf.nist.gov/10.

[113] The GBAR Collaboration. Proposal to measure the Gravitational Behaviour of Antihydrogen at Rest. *CERN report, CERN-SPSC-2011-029, SPSC-P-342*, 2011.

[114] M. Fréchet. Sur l'extension de certaines évaluations statistiques au cas de petits échantillons. *Review of the International Statistical Institute*, 11:182–205, 1943.

[115] H. Cramér. *Mathematical Methods of Statistics (new edition)*. Princeton University Press, 1999.

[116] P. Réfrégier. *Noise Theory and Application to Physics: From Fluctuations to Information*. Advanced Texts in Physics. Springer, New York, 2004.

[117] O. Rousselle, P. Cladé, S. Guellati-Khelifa, R. Guérout, and S. Reynaud. Improving the statistical analysis of anti-hydrogen free fall by using near edge events. *Physical Review A*, 105:022821, 2022.

[118] G. Dufour, R. Guérout, A. Lambrecht, V. Nesvizhevsky, and S. Reynaud. Quantum reflection of antihydrogen in the GBAR experiment. *International Journal of Modern Physics: Conference Series*, 30, 2014.

[119] N. Paul and P. Indelicato. GBAR Freefall Chamber. *Talk GBAR Meeting, december 2021*, 2021.

[120] P.-P. Crépin, C. Christen, R. Guérout, V.V. Nesvizhevsky, A.Yu. Voronin, and S. Reynaud. Quantum interference test of the equivalence principle on antihydrogen. *Physical Review A*, 99:042119, 2019.

[121] A.Y. Voronin, H Abele, S Baessler, V.V. Nesvizhevsky, A.K. Petukhov, K.V. Protasov, and A Westphal. Quantum motion of a neutron in a waveguide in the gravitational field. *Physical Review D*, 73:044029, 2006.

[122] A. E. Meyerovich and V. V. Nesvizhevsky. Gravitational quantum states of neutrons in a rough waveguide. *Physical Review A*, 73:063616, 2006.

[123] R. Adhikari, Y. Cheng, A.E. Meyerovich, and V. V. Nesvizhevsky. Quantum size effect and biased diffusion of gravitationally bound neutrons in a rough waveguide. *Physical Review A*, 75:063613, 2007.

[124] M. Escobar, F. Lamy, A. E. Meyerovich, and V. V. Nesvizhevsky. Rough mirror as a quantum state selector: Analysis and design. *Advances in High Energy Physics*, 2014:764182, 2014.

[125] J.J. Berkhout and J.T.M. Walraven. Scattering of hydrogen atoms from liquid-helium surfaces. *Physical Review B*, 47:8886–8904, 1993.

[126] C. Carraro and M.W. Cole. Sticking coefficient at ultralow energy : Quantum reflection. *Progress in Surface Science*, 57:61–93, 1998.

[127] V. Druzhinina and M. DeKieviet. Experimental observation of quantum reflection far from threshold. *Physical Review Letters*, 91:193202, 2003.

[128] H. Friedrich and J. Trost. Working with WKB waves far from the semiclassical limit. *Physics Reports*, 397:359–449, 2004.

[129] H. Oberst, Y. Tashiro, K. Shimizu, and F. Shimizu. Quantum reflection of He* on silicon. *Physical Review A*, 71:052901, 2005.

[130] B.S. Zhao, S.A. Schulz, S.A. Meek, G. Meijer, and W. Schoellkopf. Quantum reflection of helium atom beams from a microstructured grating. *Physical Review A*, 78:010902, 2008.

[131] P. Froelich and A.Y. Voronin. Interaction of antihydrogen with ordinary atoms and solid surfaces. *Hyperfine Interactions*, 213:115–127, 2012.

[132] Ch.J. Bordé. Atomic clocks and inertial sensors. *Metrologia*, 39:435–463, 2002.

[133] S. Merlet, Q. Bodart, N. Malossi, A. Landragin, F. Pereira Dos Santos, O. Gitlein, and L. Timmen. Comparison between two mobile absolute gravimeters: optical versus atomic interferometers. *Metrologia*, 47:L9–L11, 2010.

[134] A.Yu. Voronin and al. A spectroscopy approach to measure the gravitational mass of antihydrogen. *International Journal of Modern Physics: Conference Series*, 30, 2014.

[135] V.V. Nesvizhevsky, A.Yu. Vironin, P.P. Crepin, and S. Reynaud. Interference of several gravitational quantum states of antihydrogen in gbar experiment. *Hyperfine Interactions*, 240:32, 2019.

[136] A. Jurisch and H. Friedrich. Realistic model for a quantum reflection trap. *Physics Letters A*, 349:230–235, 2006.

[137] J. Madronero and H. Friedrich. Influence of realistic atom wall potentials in quantum reflection traps. *Physical Review A*, 75:022902, 2007.

[138] M. Abramowitz. *Handbook of mathematical functions with formulas, graphs, and mathematical tables*, volume 55. 1972.

[139] O. Vallée and M. Soares. *Airy functions and applications to physics*. Imperial College Press, 2004.

[140] G.B. Airy. On the intensity of light in the neighbourhood of a caustic. *Transactions of the Cambridge Philosophical Society*, 6:379, 1838.

[141] G.B. Airy. Supplement to a paper "on the intensity of light in the neighbourhood of a caustic". *Transactions of the Cambridge Philosophical Society*, 8, 1849.

[142] GRASIAN collaboration page: https://grasian.eu/.

[143] G. Pignol. Préparation de l'expérience GRANIT et recherche de nouvelles interactions avec les neutrons. *thèse Université Grenoble Alpes*, 2009.

[144] R.P. Feynman. Space-time approach to non-relativistic quantum mechanics. *Review of Modern Physics*, 20:367, 1948.

[145] P. Storey and C. Cohen-Tannoudji. The Feynman path-integral approach to atomic interferometry - a tutorial. *Journal de Physique II*, 4(11):1999–2027, 1994.

[146] O. Rousselle, P. Cladé, S. Guellati-Khelifa, R. Guérout, and S. Reynaud. Quantum interference measurement of the free fall of anti-hydrogen. *To be submitted in The European Physical Journal D, arXiv:2204.10778*, 2022.

[147] S. Agostinelli et al. Geant4 - a simulation toolkit. *Nuclear Instruments and Methods in Physics Research Section A*, 506:250–303, 2015.

[148] P. Sadowski, B. Radics, Ananya, Y. Yamazaki, and P. Baldi. Efficient antihydrogen detection in antimatter physics by deep learning. *Journal of Physics Communications*, 1:025001, 2017.

[149] P. Baldi, P. Sadowski, and D. Whiteson. Searching for exotic particles in high-energy physics with deep learning. *Nature Communications*, 5:4308, 2014.

[150] C. Killian, Z. Burkley, P. Yzombard, W. Chen, O. Hanski, E. Widmann, P. Crivelli, and S. Vasiliev. Towards the first demonstration of gravitational quantum states of atoms with a cryogenic hydrogen beam. *Stefan Meyer Institute for Subatomic Physics*, 2021.

[151] L. Rayleigh. Further applications of Bessel's functions of high order to the whispering gallery and allied problems. *The Philosophical Magazine: A Journal of Theoretical Experimental and Applied Physics*, 27:100–109, 1914.

[152] H. Mabuchi and H.J. Kimble. Atom galleries for whispering atoms—binding atoms in stable orbits around an optical resonator. *Opt. Lett.*, 19:749–751, 1994.

[153] A.Yu. Voronin, Nesvizhevsky V.V., and S. Reynaud. Interference of the whispering gallery states of antihydrogen. *Journal of Physics B Atomic Molecular and Optical Physics*, 45:165007, 2012.

[154] V.V. Nesvizhevsky, A.Yu. Voronin, R. Cubitt, and K.V. Protasov. Neutron whispering gallery. *Nature Physics*, 6:114, 2010.

[155] V.V. Nesvizhevsky, G. Pignol, and K.V. Protasov. Neutron scattering and extra-short-range interactions. *Physical Review D*, 77:034020, 2008.

[156] I. Antoniadis et al. Short-range fundamental forces. *Comptes Rendus Physique*, 12:755–778, 2011.

[157] S. Sponar, R.I.P. Sedmik, M. Pitschmann, H. Abele, and Y. Hasegawa. Tests of fundamental quantum mechanics and dark interactions with low-energy neutrons. *Nature Reviews Physics*, 3:309–327, 2021.

[158] S. Reynaud and A. Lambrecht. Casimir forces. *lectures given at Les Houches 101th summer school*, 2013.

[159] H.B.G. Casimir. On the attraction between two perfectly conducting plates. *Kon.Ned.Akad.Wetensch.Proc.*, 51:793–795, 1948.

[160] G. Plunien, B. Müller, and W. Greiner. The Casimir effect. *Physics Reports*, 134:87–193, 1986.

[161] H.B.G Casimir and D. Polder. Influence of redardation on the London - Van der Waals forces. *Nature*, 158:360, 1946.

[162] P.-P. Crépin, E.A. Kupriyanova, R. Guérout, A. Lambrecht, V.V. Nesvizhevsky, S. Reynaud, S. Vasilyev, and A.Yu. Voronin. Quantum reflection of antihydrogen from a liquid helium film. *EPL (Europhysics Letters)*, 119:33001, 2017.

[163] Python 3.10 documentation: https://docs.python.org/release/3.10.0/.

[164] T.E. Oliphant. Python for scientific computing. *Computing in Science and Engineering*, 9:10–20, 2007.

[165] K.J. Millman and M. Aivazis. Python for scientists and engineers. *Computing in Science and Engineering*, 13:9–12, 2011.

[166] Wolfram language and system documentation center: https://reference.wolfram.com/language/.

[167] S. Van der Walt, S. Chris Colbert, and G. Varoquaux. The NumPy array: a structure for efficient numerical computation. *Computing in Science and Engineering*, 13:22–30, 2011.

[168] S. Kwan Lam, A. Pitrou, and S. Seibert. Numba: a LLVM-based python JIT compiler. *Proceedings of the Second Workshop on the LLVM Compiler Infrastructure in HPC*, 7, 2015.

[169] A. Marowka. Python accelerators for high-performance computing, the journal of supercomputing. *The Journal of Supercomputing*, 74:1449–1460, 2018.

[170] Numba documentation: https://numba.readthedocs.io/en/stable/index.html.

Sujet : Analyse statistique des mesures classiques et quantiques de l'accélération de chute libre de l'antihydrogène pour l'expérience GBAR

Résumé : Le contexte de cette thèse est la collaboration GBAR au CERN qui vise à mesurer l'accélération de chute libre $\overline{g}$ des atomes d'antihydrogène ultrafroids dans le champ gravitationnel terrestre. Améliorer la précision de cette mesure est un objectif crucial pour les tests avancés du principe d'équivalence impliquant l'antimatière, qui pourrait améliorer notre compréhension de l'asymétrie observée entre matière et antimatière dans notre univers. Dans cette thèse, nous modélisons l'évolution de ces atomes d'antihydrogène depuis le piège où ils sont produits jusqu'à leur détection, en prenant en compte leur comportement quantique. Nos simulations visent à trouver les paramètres optimaux pour la chambre de chute libre afin d'obtenir la meilleure précision possible. Le recul lors du photodétachement du positron en excès de l'ion antihydrogène est pris en compte dans l'évaluation de la distribution de vitesse des atomes d'antihydrogène, et le phénomène de réflexion quantique des antiatomes sur les surfaces matérielles est aussi étudié. Combinée à la réflexion quantique sur un miroir horizontal, la gravité peut piéger les particules dans des états quantiques gravitationnels qui produisent des figures d'interférence qui peuvent être utilisées pour une mesure quantique de la valeur de $\overline{g}$. Une analyse statistique des mesures classiques et quantiques est réalisée en utilisant des simulations numériques de Monte-Carlo comparées à des méthodes analytiques. La méthode classique conduit à une précision meilleure que 10^{-2}, alors que la méthode quantique avec les états gravitationnels quantiques conduit à une précision d'environ 10^{-5}. Ce travail propose des méthodes statistiques nouvelles qui peuvent être utilisées dans d'autres applications que l'expérience GBAR.

Mots clés : antimatière - gravité - analyses statistiques - états quantiques gravitationnels.

Subject : Statistical analysis of classical and quantum measurements of free fall acceleration of antihydrogen for the GBAR experiment

Abstract : The framework of this thesis is the GBAR collaboration at CERN which aims at measuring the free fall acceleration $\bar{g}$ of ultracold antihydrogen atoms in the Earth's gravitational field. Improving the accuracy of this measurement is a crucial objective for advanced tests of the Equivalence Principle involving antimatter, which could improve our understanding of the asymmetry observed between matter and antimatter in our universe. In this thesis, we model the evolution of antihydrogen atoms from the trap where they are produced to their detection, by taking into account their quantum behaviour. Our simulations aim at finding the optimal parameters for the free fall chamber to get the best accuracy possible. The recoil in the photodetachment of the excess positron of antihydrogen ion is taken into account in the evaluation of the velocity distribution of antihydrogen atoms, and the phenomenon of quantum reflection of antiatoms on material surfaces is also studied. When combined with quantum reflection on a horizontal mirror, gravity can trap particles in gravitational quantum states, which produce interference patterns that can be used for a quantum measurement of $\bar{g}$. A statistical analysis is carried out for the classical and quantum measurements by using Monte-Carlo numerical simulations compared with analytical methods. The classical method leads to an accuracy better than 10^{-2}, while the quantum method with gravitational quantum states leads to a precision of about 10^{-5}. This work proposes new statistical methods which can be used in other applications than the GBAR experiment.

Keywords : antimatter - gravity - statistical analysis - gravitational quantum states.